THESIS FOR THE DEGREE OF DOCTOR OF PHILOSOPHY

Simulation and characterization of thermal and optical effects in surface-emitting lasers

Lars Persson

CHALMERS

Photonics Laboratory
Department of Microtechnology and Nanoscience (MC2)
Chalmers University of Technology
Göteborg, Sweden, 2025

Simulation and characterization of thermal and optical effects in surface-emitting lasers
Lars Persson

ISBN 978-91-8103-285-7
Doktorsavhandlingar vid Chalmers tekniska högskola
Ny serie nr 5743
ISSN 0346-718X

Photonics Laboratory
Department of Microtechnology and Nanoscience (MC2)
Chalmers University of Technology
SE–412 96 Göteborg
Sweden
Telephone: +46 (0)31–772 10 00

Front cover illustration: Ultraviolet surface-emitting lasers. Left: schematic of a vertical-cavity surface-emitting laser (VCSEL), where light confined by distributed Bragg reflectors (DBRs) is emitted vertically through the surface. Right: schematic of a photonic-crystal surface-emitting laser (PCSEL), where a two-dimensional photonic crystal both provides in-plane feedback and couples the light out in the vertical direction.

Printed in Sweden by
Reproservice
Chalmers Tekniska Högskola
Göteborg, Sweden, 2025

Simulation and characterization of thermal and optical effects in surface-emitting lasers
Lars Persson
Photonics Laboratory
Department of Microtechnology and Nanoscience (MC2)
Chalmers University of Technology

Abstract

III-nitride surface-emitting lasers are highly attractive as compact and efficient light sources across the visible and ultraviolet (UV) spectrum, with applications in high-brightness displays, photolithography, UV curing, and disinfection. Despite these prospects, their development has been slowed by challenges related to current injection, optical confinement, cavity length control, material defect density, and thermal management.

Blue electrically injected vertical-cavity surface-emitting lasers (VCSELs) have come the farthest, with state-of-the-art devices now achieving wall-plug efficiencies of 27.6% and output powers in the tens of milliwatts, placing them on the cusp of commercialization. One remaining hurdle is in demonstrating a robust way of realizing single mode operation and polarization control. In this thesis, we develop fabrication-friendly design concepts using localized shallow grating structures as viable strategies to achieve both.

In the ultraviolet, only optically pumped VCSELs have been realized so far, representing an important first step toward electrically injected devices. The poor thermal conductivity of AlGaN, however, means that resistive Joule heating will cause severe internal heating under electrical injection. Our simulations show that directly transferring GaN-based VCSEL designs to the UVC regime results in prohibitively high thermal resistance, but that introducing intracavity heat spreaders can lower device temperatures to lasing-viable levels. We also develop design concepts for built-in wavelength stabilization, culminating in the experimental demonstration of optically pumped UVB VCSELs with the most inherently temperature-stable emission wavelength reported to date for any VCSEL no matter material system.

The thesis also addresses UV photonic-crystal surface-emitting lasers (PCSELs). A three-dimensional coupled-wave theory framework was implemented to analyze finite-size loss mechanisms, and was complemented by the development of a new k-space weighted loss estimation method, which enables rapid analytical evaluation of vertical and lateral losses from infinite-structure band diagrams. These approaches provide powerful tools for understanding loss mechanisms in finite UV PCSELs, where a trade-off between low losses and efficient current spreading must be carefully managed.

Together, these contributions advance the understanding of thermal and optical effects in III-nitride surface emitting lasers and provide strategies and modeling frameworks to support the development of high-performance blue VCSELs, and electrically injected UV VCSELs and PCSELs.

Keywords: GaN, AlGaN, III-nitrides, blue, UV, VCSEL, PCSEL, thermal resistance, single-mode, wavelength stabilization, CWT, kSWLE

Publications

This thesis is based on the work contained in the following papers:

[A] **L. Persson**, F. Hjort, G. Cardinali, J. Enslin, T. Kolbe, T. Wernicke, M. Kneissl, J. Ciers, and Å. Haglund, "Athermalization of the lasing wavelength in vertical-cavity surface-emitting lasers", *Laser & Photonics Reviews*, 17, 8, 2300009, 2023.

[B] **L. Persson**, G. Cardinali, J. Ciers, and Å. Haglund, "Improving thermal resistance in III-nitride blue and UV vertical-cavity surface-emitting lasers", *Optics Express*, 33, p. 34242-34254, 2025.

[C] **L. Persson**, M. Riedel, Å. Haglund, and U. T. Schwarz, "Finite-size effects in photonic-crystal surface-emitting lasers - critical discussion of different approximations", *Submitted to Optics Express*, 2025.

Related conference contributions, not included in the thesis:

[D] **L. Persson**, J. Ciers, F. Hjort, and Å. Haglund "Thermal wavelength stability of ultraviolet-B vertical-cavity surface-emitting lasers enabled by short cavity length and dielectric mirrors", *Compound Semiconductor Week, Stockholm, Sweden*, 2021.

[E] **L. Persson**, F. Hjort, G. Cardinali, J. Enslin, T. Kolbe, T. Wernicke, M. Kneissl, J. Ciers, and Å. Haglund "Athermalization of the emission wavelength in UVB VCSELs" *International Workshop on Nitrides (IWN), Berlin, Germany, OD-AT034*, 2022.

[F] **L. Persson**, G. Cardinali, and Åsa. Haglund "Will AlGaN VCSELs with all-dielectric DBRs die from heat?" *International Workshop on Nitrides (IWN), Honolulu, USA, OD-422*, 2024.

[G] L. Sharma, **L. Persson**, J. Ciers, and Å. Haglund " Design of Single-Mode and Polarization stable 450 nm Vertical Cavity Surface Emitting Laser (VCSEL) with Surface Relief and Sub-Wavelength Grating", *International Conference on Nitride Semiconductors (ICNS), Malmö, Sweden, OD-Mon-3*, 2025.

[H] D. Apaydın, **L. Persson**, M. Riedel, S. Graupeter, L. Uhlig, J. Ciers, T. Wernicke, M. Kneissl, U. T. Schwarz, and Å. Haglund "Understanding losses and mode selection in finite-sized ultraviolet-C photonic-crystal surface-emitting lasers" *International Conference on Nitride Semiconductors (ICNS), Malmö, Sweden, OD-Mon-6*, 2025.

[I] M. Riedel, L. Uhlig, **L. Persson**, Å. Haglund, and U. T. Schwarz "Losses in deep-UV Photonic Crystal Surface Emitting Lasers: finite-size coupled wave theory simulations versus semi-analytical approximation" *International Conference on Nitride Semiconductors (ICNS), Malmö, Sweden, OD-Mon-7*, 2025.

Contents

Acknowledgement

First and foremost, I am deeply grateful to my main supervisor, Prof. Åsa Haglund for the opportunity to work in the exciting field of III-nitride VCSELs. Her guidance, encouragement, and constant willingness to discuss ideas have been invaluable throughout my PhD journey, and I could not have wished for a better supervisor. Åsa is a master of language, something I've experienced first-hand over the years through countless red markings; but I believe I'm better off for it, and my writing has improved a lot. Åsa is also a master of many other things, including explaining things in a way that is understandable to everyone.

I also wish to express my sincere gratitude to my assistant supervisor, Dr. Joachim Ciers, for all the help I've received in the lab and for the many discussions over the years. Joachim knows "everything" and is the person to turn to whenever help or advice is needed, something I, and many others, have greatly appreciated over the years.

My gratitude also goes to former Assoc. Prof. Jörgen Bengtsson, who showed me that there is always a "dark" and a "light" side, even in optics conventions, and that one should never stray too far from the light: always choose $+jk_0z$. He is perhaps the biggest reason why I became fascinated by optics, photonics, and simulations, thanks to an optics course I took with him during my second bachelor year in engineering physics. I still remember many of his teachings, including that even the smallest bug in Matlab code can lead to unexpectedly high levels of laser radiation: a reminder that laser safety is important not only in the lab.

I also want to thank Estrella, my comrade-in-office for about four years, for all the interesting discussions we have had during that time. More recently, I have had the pleasure of sharing an office with Cleophace and Sharma, and together we are trying to solve the problem that is the blue VCSEL: in other words, plenty of fun! I am also grateful to the rest of the group for their positive attitudes and good vibes. A special thanks goes to Erik for many discussions and for the fun we have shared in the optics lab, as well as for our swashbuckling chess battles during lunch breaks, where every pawn was fearlessly sacrificed. It has truly been a real hoot! I would also like to thank all the colleagues in the Photonics lab for the positive atmosphere, the interesting lunchroom discussions, and the occasional game of chess over the years.

There is also a place beyond work, and I would like to extend my thanks to Simon, Erik, and William for always being up for battling it out for control over the Woodland, racing to terraform Mars, wrestling dominion over the kingdom, and countless other adventures, or simply just hanging out. Always a joy!

Finally, I would like to thank my family. My dad's steady support and belief in me have been invaluable, both during this PhD and long before it began. Even though mom has gone to a better place, I like to believe that she would have been proud. I am grateful to my siblings for all their support over the years, even if we do not see each other as often as I would wish. I suspect that Mathias introducing me to Star Wars at a very young age may have had something to do with me ending up in photonics, in the hope of one day finding a real lightsaber. The search continues.

And to Frida: I cannot thank you enough for your unconditional support, for the joy you bring, and for always inspecting my figures. Now, as I sit here finishing this acknowledgment at 4 AM on the night before (or morning of) the printing of this thesis, I can't help but recall one of our informal house mottos: "om något är jobbigt så kanske man behöver det", which is always said with a twinkle in the eye, and usually invoked when it is time to go shopping, or simply when the couch is too comfortable to get up from.

Lars Persson
Göteborg, Sweden
September 2025

Acronyms

CW	Continuous wave
CWT	Coupled-wave theory
DBR	Distributed Bragg reflector
EEL	Edge-emitting laser
FF	Fill factor
FDTD	Finite-difference time-domain
GME	Guided-mode expansion
ITO	Indium tin oxide
LED	Light-emitting diode
PC	Photonic crystal
PCSEL	Photonic-crystal surface-emitting laser
QW	Quantum well
RCWA	Rigorous coupled-wave analysis
kSWLE	k-space weighted loss estimation
UVA/UVB/UVC	Ultraviolet A/B/C
VCSEL	Vertical-cavity surface-emitting laser

Chapter 1

Introduction

When the first laser (light amplification by the stimulated emission of radiation) was demonstrated in 1960 [1, 2], it was hailed in newspapers as "the incredible laser". Science fiction writers quickly seized on the idea, turning the new device into futuristic laser guns and "death rays" (famously featured in the 1964 James Bond film Goldfinger) that could vaporize anything in their path. Later, lasers were immortalized in popular culture by the lightsabers carried by Jedi knights in Star Wars (1977), shaping the public imagination of what a "laser" could be, but never would be. In reality, the laser's beginnings were far less dramatic. One of its pioneers, Arthur Schawlow, jokingly noted at a conference that a more accurate acronym would actually have been "loser", short for "light oscillation by stimulated emission of radiation" [3]. The joke did not stick, but the name "laser" did, and so did the technology. What was once described as a "solution looking for a problem" soon became a cornerstone of modern science and technology.

In the decades that followed, lasers transitioned from laboratory curiosities to essential tools woven into everyday life. They now scan barcodes at supermarkets, carry vast amounts of information through optical fibers at the speed of light, and perform delicate eye surgeries with unrivaled precision. At the same time, lasers have enabled Nobel-prize-winning research in physics and chemistry, powered modern manufacturing processes, and opened entirely new frontiers in medicine and sensing. Today, it is difficult to imagine a world without them.

Among the many forms of lasers, semiconductor lasers have found widespread use thanks to their compact size, low cost, high power efficiency, and compatibility with mass production, which have made them indispensable in consumer electronics and communication systems. Within this family, the vertical-cavity surface-emitting laser (VCSEL) has played an important role, that today forms a fast-growing billion dollar industry [4]. The first infrared GaAs-VCSELs were conceived in 1979 [5] and commercialized in 1996 [6, 7]. VCSELs combine low threshold currents and circular, low-divergence beams

with a compact geometry (Fig. 1.1) that enables dense two-dimensional arrays and on-wafer testing that reduces cost. Furthermore, they can be modulated at high speed while operating at low currents, often have single longitudinal mode emission with only a small wavelength shift under varying temperature, and can be tuned continuously with current. VCSELs can also be designed for single transverse mode operation. Compared to light-emitting diodes (LEDs), they provide higher conversion efficiencies at high current densities, enabling higher output power per chip area. These advantages have led to applications ranging from short-reach optical communication to 3D sensing in smartphones [8, 9].

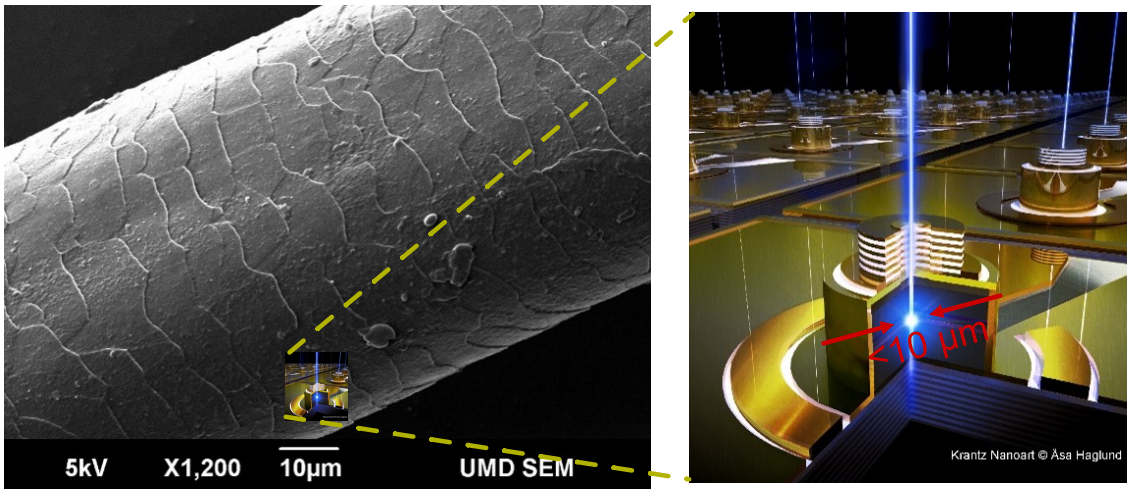

Figure 1.1: Illustration of the extremely small size of a VCSEL aperture ($\lesssim 10\,\mu m$), shown in comparison to a human hair of $\approx 50\,\mu m$ diameter.

Despite the widespread success of infrared GaAs-based VCSELs, extending their operation into the green-to-ultraviolet (UV) spectral range has proven far more difficult. For many years, one of the main challenges was the lack of suitable semiconductor materials with bandgaps large enough for laser emission in this spectral range. This situation began to change in the early 1970s with the pioneering work of Herbert Maruska at RCA Laboratories [10–12]. In 1972, Maruska and colleagues demonstrated the first blue emission from gallium nitride (GaN) by introducing magnesium acceptors [12]. However, the devices were extremely dim, and RCA eventually abandoned the project before the technology could mature [13, 14]. For nearly two decades, GaN remained a difficult material to work with due to the challenges of crystal quality and p-type doping, and most groups around the world shifted their focus to other material systems.

Renewed progress came in the 1980s and 1990s through the efforts of Isamu Akasaki, Hiroshi Amano, and Shuji Nakamura, who succeeded in overcoming the key barriers of GaN growth and p-type doping [15–19]. Their innovations enabled the demonstration of the first high-brightness blue LEDs in the mid-1990s [20–24]. This development completed the trio of red, green, and blue

emitters required for full-color displays, and also enabled efficient white light sources through the use of blue LEDs with suitable phosphors. These breakthroughs opened the door to energy-efficient solid-state lighting and numerous new applications. In recognition of this achievement, Akasaki, Amano, and Nakamura were awarded the Nobel Prize in Physics in 2014 "for the invention of efficient blue light-emitting diodes, which have enabled bright and energy-saving white light sources" [13].

Building on the success of the blue LED, efforts soon turned to extending GaN technology to lasers. The first blue edge-emitting laser was demonstrated in 1996 [22], only a few years after the blue LED. Development of GaN VCSELs proved more challenging, with the first demonstration of electrically injected devices not coming until 2008 [25, 26]. Continued progress was slowed by challenges in achieving highly reflective mirrors, precise cavity control, transverse current confinement, electrical injection efficiency, and thermal management. In recent years, however, steady advances have brought blue VCSELs closer to commercialization. Some of the most impressive demonstrations to date have been achieved by Sony Corporation in 2024, with VCSELs showing wall-plug efficiencies (WPE) of up to 22.2% and output powers exceeding 8 mW [27], and by Meijo University in 2025, with a blue VCSEL reaching a WPE of 27.6%, a maximum output power of 16.2 mW, and a threshold current density of 7.7 kW cm^{-2} [28, 29], showing that blue VCSELs are now on the cusp of commercialization.

Progress in the ultraviolet (UV) spectral range has been slower and more difficult. UV VCSELs face additional challenges due to the wide bandgap required, especially for emission below 360 nm. In this regime, AlGaN alloys replace GaN/InGaN, but their thermal and electrical conductivities are orders of magnitude lower, and the electrical injection efficiency has until recently been only a few percent. Higher defect densities and non-uniform surface morphologies further complicate device fabrication. In VCSELs, the current injection and light output occur along the same vertical axis, which makes transverse current spreading and confinement a challenge without introducing excessive optical loss, and achieving high-reflectivity mirrors in the deep-UV remains challenging. As a result, only optically pumped deep-UV devices have been demonstrated [30–32], though research continues to push toward electrically driven UV VCSELs. Recent progress from Meijo and Nagoya has solved part of this puzzle by demonstrating that high injection efficiencies can be achieved in optimized AlGaN structures emitting in the UVB and UVC [33–37].

In parallel with these developments, another important branch of surface-emitting lasers emerged with the photonic-crystal surface-emitting lasers (PCSELs). PCSELs combine the high beam quality of VCSELs with power levels comparable to edge-emitting lasers, making them highly attractive for applications requiring high-brightness single-mode emission. The first infrared InP-based PCSELs were demonstrated in 1999 [38]. In recent years, PCSELs have achieved remarkable performance, with Kyoto University reporting 50 W single-mode continuous-wave (CW) operation in 2023 [39]. Today, several companies,

such as Vector Photonics [40, 41], as well as the center of excellence (COE) at Kyoto University [42, 43], are actively trying to bring about the commercialization of PCSELs.

As with VCSELs, extending PCSELs into the blue spectral region proved more difficult. The first demonstrations under electrical pulsed operation came only in 2008 [44], and progress remained slow. In 2022, Kyoto University achieved a milestone with a blue PCSEL delivering 320 mW in CW operation. However, extending the emission wavelength further into the UVC for PCSELs remains an open challenge, with the only demonstrations to date, reported by our group, relying on optical pumping [45].

1.1 Applications

Ever since their first demonstrations, many different lasers have been developed, often driven by curiosity: what can we get to lase? But beyond curiosity, lasers have found countless areas of application and immense societal impact. Today, semiconductor lasers are commercially available from the infrared (> 750 nm) through much of the visible spectrum (400-700 nm), and even into the UVA (320-400 nm). However, they remain absent in the UVB (280-320 nm) and UVC (200-280 nm) ranges, where only solid-state lasers and excimer lasers are currently available. While these systems can fill certain needs, they mostly generate heat ($\approx 99.98\%$), typically produce poor beam quality, suffer from high cost, and are bulky compared to semiconductor lasers. This motivates the development of compact III-nitride devices such as VCSELs and PCSELs, as energy-efficient and low-cost UV light sources.

One reason UVC light is so useful is that it does not naturally reach the Earth's surface due to strong absorption by atmospheric gases like oxygen and ozone (Fig. 1.2). This has allowed life to evolve without developing resistance to its effects. As a result, UVC light is highly effective at inactivating bacteria and viruses by damaging their DNA and RNA, as its wavelength aligns with the peak absorption of nucleic acids [46]: in a sense a "death ray," and the science-fiction writers were right all along! This property makes UVC light useful for disinfection and sterilization applications, including water purification, air treatment in ventilation systems, and surface sterilization of medical equipment [47]. It also enables solar-blind optical communication, since the absence of solar background in this spectral range allows high signal-to-noise detection without sunlight interference [48]. UVC light has gained increasing attention in recent years due to the COVID-19 pandemic and its proven ability to inactivate the coronavirus (SARS-CoV-2) [49]. Many of these applications directly align with the United Nations Sustainable Development Goals [50] and the Minamata Convention on Mercury, since UVC VCSELs and PCSELs could provide compact, energy-efficient, and mercury-free alternatives to conventional UV lamps.

In the UVB range, lasers could be employed in medical phototherapy, for

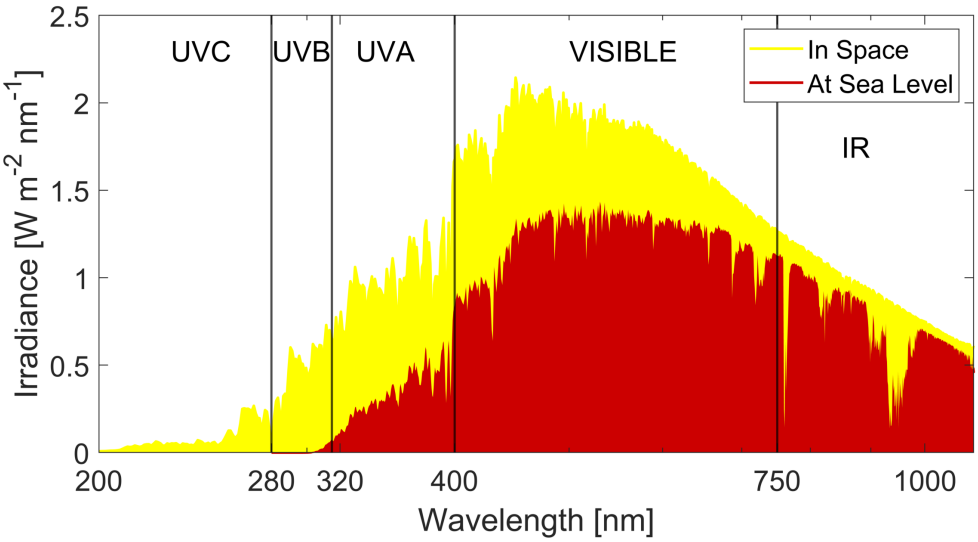

Figure 1.2: Solar spectral irradiance in space (AM0) and at sea level (AM1.5G) from the ASTM G173-03 reference spectra [51], showing the reduction of irradiance at Earth's surface due to atmospheric absorption.

example, in the treatment of skin conditions such as psoriasis or vitiligo, or for dermatological applications [46]. In the UVA range, light penetrates deeper into tissue, making them suitable for biomedical imaging and scanning applications, such as retinal diagnostics. Beyond healthcare, UV VCSELs also hold promise in UV curing [46], photolithography [46], and sensing applications such as ozone detection [52] and atomic clocks [53].

In the blue-violet ($\approx 400 - 500$ nm), semiconductor lasers enable a wide array of technologically important applications. Blue VCSELs are attractive for high-resolution displays and projectors [54], including AR/VR and automotive head-up displays [55, 56], where shorter wavelengths allow finer pixelation and vivid color reproduction. Their low power consumption also makes them well suited for portable applications such as smart glasses. In addition, because green and blue light penetrates seawater efficiently, compact VCSELs are promising candidates for underwater optical communication [57]. Other emerging applications include adaptive automotive headlights and high-precision 3D printing.

Photonic-crystal surface-emitting lasers (PCSELs) extend the scope of short-wavelength semiconductor lasers to also include high-power applications. By combining the surface-emitting geometry of VCSELs with large-area photonic-crystal feedback, PCSELs can achieve single-mode operation over millimeter-scale apertures with high-output powers while maintaining excellent beam quality. This makes them attractive for applications such as photolithography, disinfection, machining of difficult-to-process materials, high-brightness solid-state illumination, and underwater light detection and ranging

(LiDAR) [58].

1.2 Outline of thesis

This thesis contributes to the understanding and development of surface-emitting lasers in the UV and blue spectral regions, with a focus on their optical and thermal properties, and provides theoretical tools for future device optimization.

Chapter 2 reviews key material properties of the III-nitride system, including optical, electrical, and thermal aspects relevant to surface-emitting devices. Chapter 3 introduces the fundamental concepts of VCSEL operation and design, covering resonant cavity effects, mirror properties, and thermal behavior. Chapter 4 presents our work on III-nitride VCSELs, addressing design strategies, thermal management, and wavelength stabilization, along with experimental and simulation results. Chapter 5 focuses on photonic-crystal surface-emitting lasers, discussing their fundamental principles, finite-size effects, and introducing a new analytical method for estimating lateral and vertical losses. Chapter 6 concludes the thesis with a summary of the main findings and an outlook on future challenges in realizing high-performance blue and UVC VCSELs and PCSELs.

Chapter 2

Properties of the III-nitride material system

The group-III nitride semiconductor system, comprising GaN, AlN, InN, and their ternary alloys, forms the material foundation for ultraviolet (UV) and blue surface-emitting lasers. These materials offer wide, direct bandgaps, making them well suited for optoelectronic devices operating at short wavelengths. For instance, InGaN QWs have paved the way for energy efficient blue LEDs that have enabled the LED lighting revolution, and AlGaN QWs have the promise of enabling UV light sources for applications including disinfection and water purification as discussed in the introduction. At the same time, several fundamental material properties set III-nitrides apart from more established III–V systems such as GaAs or InP, introducing unique challenges and tradeoffs in the design and realization of laser devices.

When research on III-nitride optoelectronics began, it was widely believed, based on decades of experience with GaAs-based devices, that efficient laser action would Only by possible if the dislocation density could be reduced below $\lesssim 1 \times 10^4\,\mathrm{cm}^{-2}$ [59–61]. GaAs VCSELs, for instance, degrade rapidly when grown on defective substrates, and such low dislocation densities were considered a prerequisite for efficient operation [59–61]. In contrast, epitaxial III-nitride films grown on foreign substrates such as sapphire or silicon typically exhibit threading dislocation densities in the range of $10^{8-10}\mathrm{cm}^{-2}$. That III-nitride LEDs and lasers can operate efficiently under such conditions was initially viewed as a paradox. This unexpected success is now attributed to carrier localization in the InGaN quantum well active region, primarily due to compositional fluctuations in InGaN [62–65]. These fluctuations create localized potential minima that spatially confine carriers, reducing their overlap with non-radiative recombination centers such as dislocations. As a result, even though the material is highly defective by traditional metrics, radiative recombination remains efficient.

This dislocation tolerance is just one of several unexpected and unconventional properties that distinguish III-nitride semiconductors from more established III–V materials. In the following sections, other key characteristics are examined in more detail, including the high effective carrier masses and their consequences for optical gain, the challenges of p-type doping and low free carrier concentrations, the unique polarization fields arising from the wurtzite crystal structure, and the thermal properties. Together, these properties define both the opportunities and the design constraints faced in the development of III-nitride surface-emitting lasers.

2.1 Crystal structure and polarization effects

Group-III nitrides such as GaN, AlN, and InN crystallize predominantly in the wurtzite structure under typical growth conditions [66]. This hexagonal phase is energetically favored over the cubic zincblende polymorph and is characterized by two interpenetrating hexagonal close-packed sublattices: one composed of group-III atoms and the other of nitrogen as shown in Fig. 2.1. The resulting lack of inversion symmetry along the [0001] direction, combined with the large electronegativity difference between group-III elements (In, Ga, Al) and nitrogen, gives rise to strong internal polarization fields.

The wurtzite lattice features two lattice constants, a_0 and c_0, defining anisotropic material properties. Crystal planes of particular importance include the polar c-plane (0001), and the nonpolar a-plane $(11\bar{2}0)$ and m-plane $(10\bar{1}0)$, also indicated in Fig. 2.1. Most devices are grown along the c-plane due to established growth methods and substrate availability, though this orientation is associated with strong polarization effects.

The lack of centrosymmetry gives rise to a spontaneous polarization along the c-axis, even in unstrained layers. When heterostructures experience strain, due to lattice mismatch or thermal expansion mismatch, additional piezoelectric polarization is induced. The resulting polarization fields significantly influence the electronic band structure in QWs, particularly for c-plane devices. These fields tilt the conduction and valence band edges and spatially separate the electron and hole wavefunctions, as shown in Fig. 2.2(a). This effect, known as the quantum-confined Stark effect (QCSE), reduces the wavefunction overlap, decreases radiative efficiency, and redshifts the emission wavelength at low injection levels.

The magnitude of the polarization fields in III-nitride quantum wells depends on the degree of lattice mismatch between the well and barrier materials. Since the lattice mismatch between InN and GaN is significantly larger than that between AlN and GaN, the strain-induced piezoelectric polarization, and hence the overall polarization field, is typically stronger in InGaN/GaN wells than in AlGaN/GaN [67]. As a result, QCSE tends to be more pronounced in InGaN-based structures, leading to a larger redshift and reduced wavefunction overlap at low excitation levels.

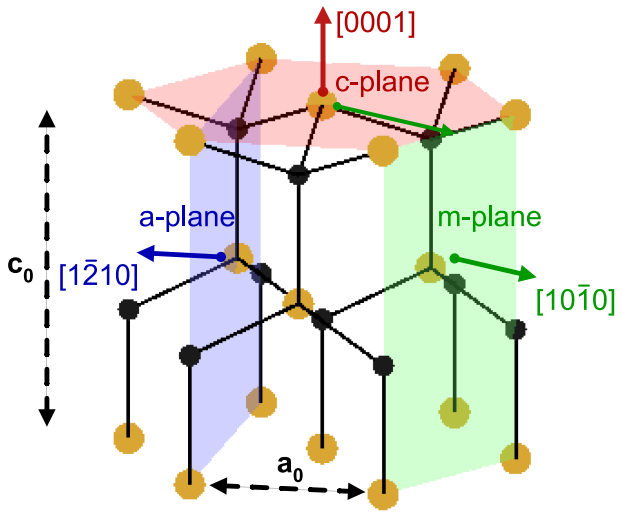

Figure 2.1: Wurtzite crystal structrue. The orange atoms represent the Al/Ga/In sublattice, and the black atoms the N sublattice. The three most important crystal planes are indicated: red c-plane (0001), blue a-plane $(1\bar{2}10)$, and green m-plane $(10\bar{1}0)$.

At higher carrier densities, the polarization fields are partially screened by free carriers, which flattens the bands and reduces the QCSE [68]. As a result, the emission wavelength blueshifts with increasing current density. This screening effect can be observed in electroluminescence measurements of InGaN-based LEDs, as shown in Fig. 2.2(b), where the emission wavelength shifts by up to 20 nm. However, it has been suggested that at low current densities, additional effects may contribute to this blueshift. In-rich composition fluctuations in the quantum wells can create localized states at lower energies, which dominate emission at low carrier injection. These states may have a low density of states and can be easily filled, causing a rapid shift of the emission to higher-energy states as the carrier density increases. In this interpretation, the strong initial blueshift at low current densities is driven by state filling, while at moderate to high current densities, the continued blueshift is primarily governed by carrier screening of the polarization fields. This dual contribution may explain the more pronounced blueshift at low current densities and the subsequent flattening of the curve at moderate and high injection levels observed in Fig. 2.2(b).

A detailed understanding of polarization-induced effects is essential for device design. In LEDs, which typically operate at low current densities where polarization fields remain largely unscreened, it is particularly important to use thin quantum wells. Thin wells reduce the spatial separation between the electron and hole wavefunctions, which increases their overlap and improves radiative recombination efficiency. In contrast to LEDs, lasers such as VCSELs and PCSELs operate at significantly higher current densities, on the order of a few kA/cm^2, where the internal fields are mostly screened. In this regime, the wavefunction overlap improves, and the emission wavelength shifts toward the

zero-field case. However, it becomes crucial to account for the blueshift due to carrier screening when designing the structure, so that the gain peak, cavity resonance, and mirror stopband remain aligned under operating conditions. This alignment is discussed in further detail in Section 3.4.

Another strategy that has recently gained attention is the use of thick quantum wells, where optical transitions involving higher excited states are less affected by polarization-induced separation of carriers, thereby reducing the QCSE shift [69]. Theoretical calculations have also shown that the achievable gain can be similar in devices employing multiple thin QWs or a single thick QW [70]. An alternative approach to mitigating the QCSE is to grow the active region on nonpolar or semipolar crystal planes, where the polarization fields are significantly reduced or eliminated altogether [71]. While this can improve performance by restoring symmetric band profiles, such orientations also introduce challenges in growth and processing.

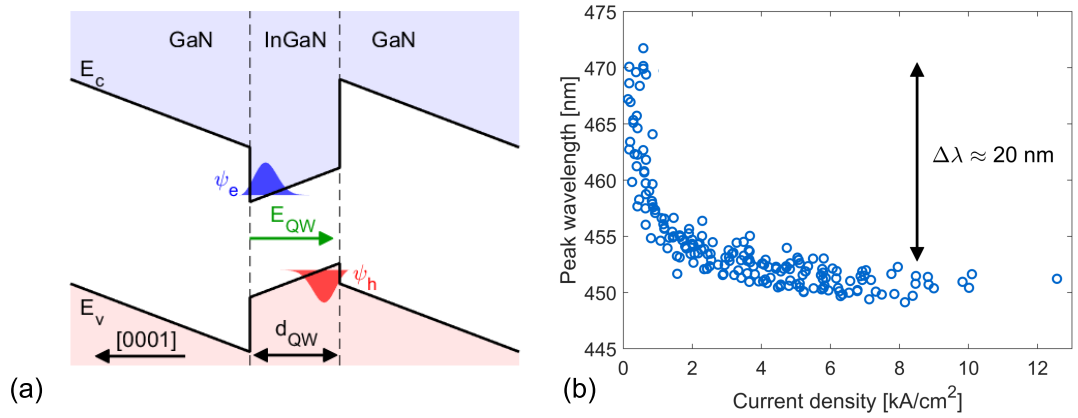

Figure 2.2: (a) Illustration of the bandstructure and the tilt caused by the polarization fields. The electron and hole wavefunctions are also shown to reside in opposite spatial parts of the QW. (b) Measured electroluminescence peak shift of blue LEDs with InGaN QWs. The blueshift caused by carrier screening is here 20 nm.

2.2 Optical properties

The III-nitride material system offers direct bandgap with wide tunability, extending from the infrared (InN, $\sim$ 0.7 eV) to the deep ultraviolet (AlN, $\sim$ 6.1 eV). This forms the basis for a variety of light-emitting devices. An overview of the bandgap and corresponding wavelength versus in-plane lattice constant, a_0, for the binary and ternary compounds is shown in Fig. 2.3.

The refractive index of III-nitride materials depends on both composition and wavelength. For wavelengths longer than the absorption edge, i.e., in the transparent regime, the refractive index generally decreases with increasing wavelength. Near the absorption edge, strong dispersion occurs due to inter-

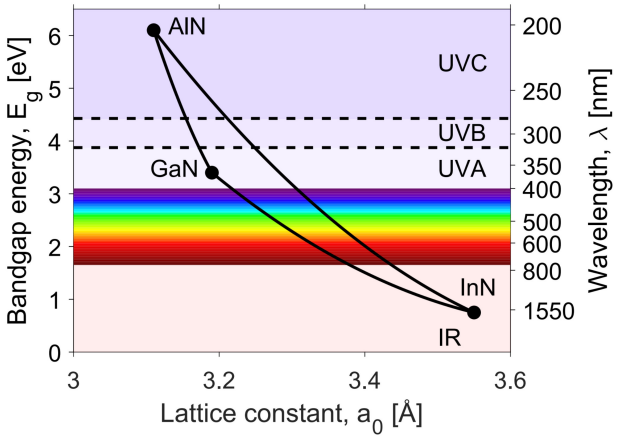

Figure 2.3: Bandgap energy E_g, corresponding emission wavelength, and in-plane lattice constant a_0 for III-nitride binary compounds (AlN, GaN, InN) and their ternary alloys (AlGaN, InGaN, AlInN) at room temperature. Spectral regions from infrared (IR) to ultraviolet (UVA, UVB, UVC) are indicated for reference. Material parameters are taken from [72].

band transitions, as seen in Fig. 2.4. These trends are important in the design of optical components that rely on refractive index contrast, such as mirrors, resonant cavities, and photonic crystals. In addition, the refractive index varies with temperature [73, 74] and carrier concentration [75], both of which are important to consider in device design.

The wurtzite crystal structure of III-nitrides gives rise to optical anisotropy, with the material acting as a positively uniaxial birefringent medium. The ordinary refractive index, relevant for transverse electric (TE) polarization light propagating along the c-axis, is shown in Fig. 2.4. For layers grown along non-c-axis directions, the optical axis is tilted with respect to the surface normal, and the polarization of the optical mode can align either parallel (extraordinary) or perpendicular (ordinary) to this axis. Because these two polarizations experience different refractive indices, the cavity can be engineered to support only one of them. In VCSELs, this birefringence has been used to achieve polarization locking in otherwise rotationally symmetric cavities. This effect has been demonstrated in devices grown on m-plane substrates, where the optical axis lies in the wafer plane and breaks the in-plane symmetry [76].

2.3 Bandstructure

In semiconductors, the periodic crystal potential causes the electronic states to form bands. The energy separation between the conduction and valence bands defines the bandgap, which determines the material's optical and electronic properties.

The wurtzite crystal structure of GaN and AlN leads to an anisotropic

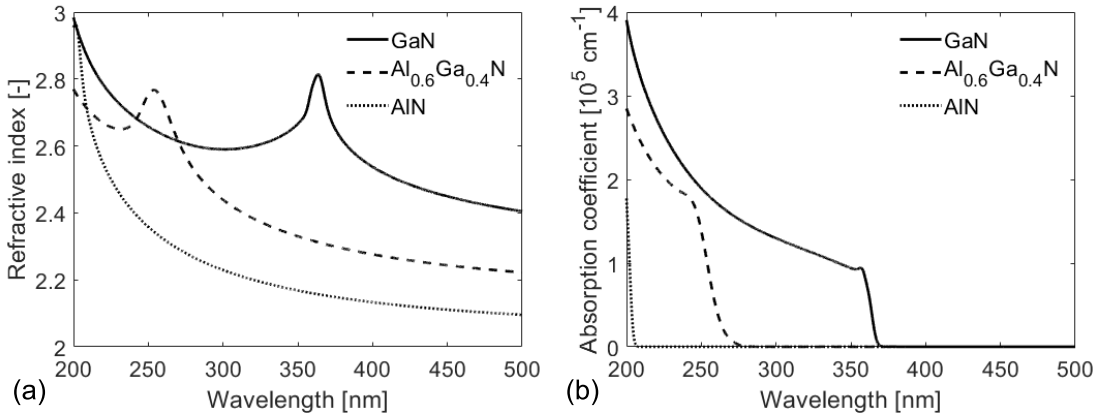

Figure 2.4: The real part of the refractive index, n, (a) and its imaginary part, κ, scaled to be an absorption coefficient $\alpha = 4\pi\kappa/\lambda$ (b) of the ordinary refractive index for GaN (solid), $Al_{0.6}Ga_{0.4}N$ (dashed), and AlN (dotted).

bandstructure, meaning the energy-momentum relation differs along the c-axis (k_z) and in-plane directions ($k_{||}$). At the Brillouin zone center (Γ-point), the valence band splits into heavy hole (HH), light hole (LH), and crystal-field split-off (CH) bands due to spin–orbit and crystal-field interactions. Their relative ordering depends strongly on alloy composition, strain, and quantum confinement [77].

Figure 2.5 shows calculated valence band dispersions for unstrained GaN and AlN using $k \cdot p$ theory [78] with parameters from [67]. In GaN, the HH band lies highest, while in AlN the CH band is dominant. Transitions from the conduction band to HH or LH bands produce TE-polarized light (electric field perpendicular to the c-axis), whereas transitions to the CH band generate transverse magnetic (TM) polarized light (electric field parallel to the c-axis). As Al content increases, the shift toward CH-band dominance leads to more TM-polarized emission, which is poorly confined in vertical-cavity devices like VCSELs.

The crossover point from HH to CH dominance occurs around $\sim 4\%$ Al for unstrained bulk layers, but can shift to $\sim 60\%$ under compressive strain [79]. Quantum confinement in thin QWs also affects the band ordering: for wells thinner than 3 nm, the transition to TM polarization may not occur until $\gtrsim 80\%$ Al [79]. This interplay between strain, composition, and confinement is critical in designing efficient deep-UV lasers. Even in UV LEDs, TM polarization is undesirable, since TM-polarized light propagates in-plane with the quantum wells, making it difficult to extract.

2.3.1 Effective mass influence on laser thresholds

GaN has a wider bandgap and flatter band curvature near the band edges, which results in significantly higher effective masses for both electrons and

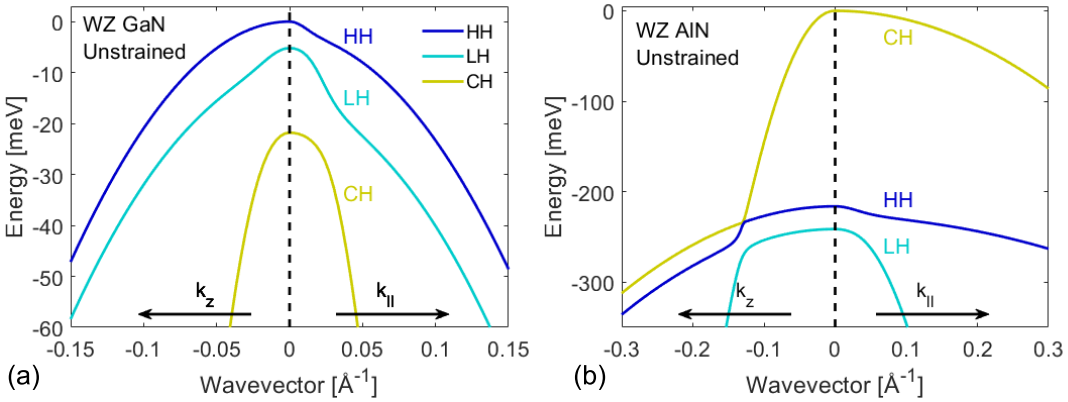

Figure 2.5: Valence band dispersions for unstrained wurtzite (WZ) GaN (a) and AlN (b), showing the heavy hole (HH), light hole (LH), and crystal-field split-off (CH) bands. The energy is plotted as a function of wavevector along the c-axis direction k_z and the in-plane direction $k_{||}$. The band ordering and curvature differ significantly between GaN and AlN due to variations in crystal-field splitting and spin–orbit interaction. Parameters used for the kp calculations were taken from [67].

holes. These larger effective masses increase the density of states (DoS) near the band edges, meaning that more carriers must be injected to achieve population inversion and optical gain over a given energy interval. A simple quantitative comparison between intrinsic GaAs and GaN using the Bernard–Duraffourg condition at 0 K shows that the required excess carrier density n scales with the reduced effective mass m_r of the electron–hole system [80]

$$\frac{n_{GaN}}{n_{GaAs}} = \frac{m_{r,GaN}}{m_{r,GaAs}}, \tag{2.1}$$

were $m_r = m_e^* m_{dh}/(m_e^* + m_{dh})$, m_e^* is the effective electron mass, $m_{dh} = ({m_{hh}^*}^{3/2} + {m_{lh}^*}^{3/2})^{2/3}$ is the combined density-of-states hole mass, m_{hh}^* is the heavy hole effective mass, and m_{lh}^* is the light hole effective mass. The effective mass is inversely proportional to the curvature of the energy band, and thus heavier masses correspond to flatter bands and higher DoS near the band edge. This results in GaN requiring approximately six times higher excess carrier density than GaAs to achieve optical gain over the same energy bandwidth. The estimate is approximate and does not take into account differences in the peak gain amplitude, which is more directly relevant to the lasing threshold.

This inherent requirement for high carrier injection directly impacts the design of III-nitride vertical-cavity and photonic-crystal surface-emitting lasers. Devices must support higher current densities while maintaining efficient carrier confinement and minimizing heating. Moreover, the higher effective masses also correlate with lower carrier mobility, particularly for holes, which further complicates efficient injection in GaN-based laser structures.

2.4 Electrical properties

A key challenge in III-nitride materials is achieving high free carrier concentrations through impurity doping. Intentional n-type doping is typically done with silicon (Si), which forms shallow donor levels ($\sim 20\,\mathrm{meV}$ for GaN) that are mostly ionized at room temperature. This enables electron concentrations up to $1 \times 10^{19}\,\mathrm{cm}^{-3}$ without significant degradation of crystal quality. However, increasing the Al content in AlGaN raises the donor ionization energy, reducing the activation efficiency, especially for Al mole fractions approaching 80% and beyond [81, 82].

P-type doping is considerably more difficult. Magnesium (Mg) is the most commonly used acceptor in GaN, but its ionization energy is high (170 meV), resulting in only a few percent of Mg atoms being ionized at room temperature. As a result, typical hole concentrations are limited to $\sim 1 \times 10^{18}\,\mathrm{cm}^{-3}$, even for high Mg levels. Unintentional background doping often has n-type character [83], which further lowers the effective hole concentration. The difficulty of achieving p-type conductivity becomes even more pronounced in AlGaN due to the increasing bandgap, which causes the ionization energy of Mg to increase further with Al content [81, 84]. For high-Al content ($x > 0.7$), hole concentrations can drop below $1 \times 10^{17}\,\mathrm{cm}^{-3}$.

Figure 2.6 shows the calculated fraction of ionized donors and acceptors in $\mathrm{Al}_x\mathrm{Ga}_{1-x}\mathrm{N}$ as a function of Al content at 20 °C and 80 °C, using Fermi–Dirac statistics and material parameters from [85]. The model assumes donor concentration of $2 \times 10^{18}\,\mathrm{cm}^{-3}$ and an acceptor concentrations of $5 \times 10^{19}\,\mathrm{cm}^{-3}$, chosen to yield comparable free carrier densities at room temperature. The results highlight the steep decline in ionization efficiency with increasing Al content due to higher dopant ionization energies. At 20 °C and an aluminium composition of 70%, less than 10% of donors and only $\sim 0.1\%$ of acceptors are ionized. While higher temperatures improve activation slightly, p-type doping remains severely limited.

Because of the low hole concentrations (and low hole mobility) the conductivity of p-doped layers are low. Therefore, ITO is commonly used on the p-side to aid lateral current spreading. However, ITO becomes highly absorbing in the UV and is unsuitable for AlGaN-based emitters. At the same time, p-type conductivity in AlGaN is even lower than GaN, making injection and current spreading more difficult. Alternative strategies such as distributed polarization doping (DPD) and tunnel junctions (TJs) have been developed to address these challenges. In DPD structures, a spatially graded AlGaN layer generates polarization charges that create an internal electric field, which effectively assists hole transport into the active region. This approach, often combined with Mg doping, enabled the first electrically pulsed UVB laser diodes [33, 34, 86] and the first continuous-wave (CW) UVC laser diodes [37]. Tunnel junctions (TJs) provide another route to bypass p-type limitations by enabling lateral current spreading in n-type layers. While this approach is particularly attractive for AlGaN-based UV devices, its feasibility has already been demonstrated in blue

VCSELs by Meijo [87] and UCSB [88]. TJs have also recently been demonstrated in resonant-cavity UVB LEDs (RCLEDs) [32], which are structurally similar to VCSELs and show promise for future electrically injected UV VCSELs.

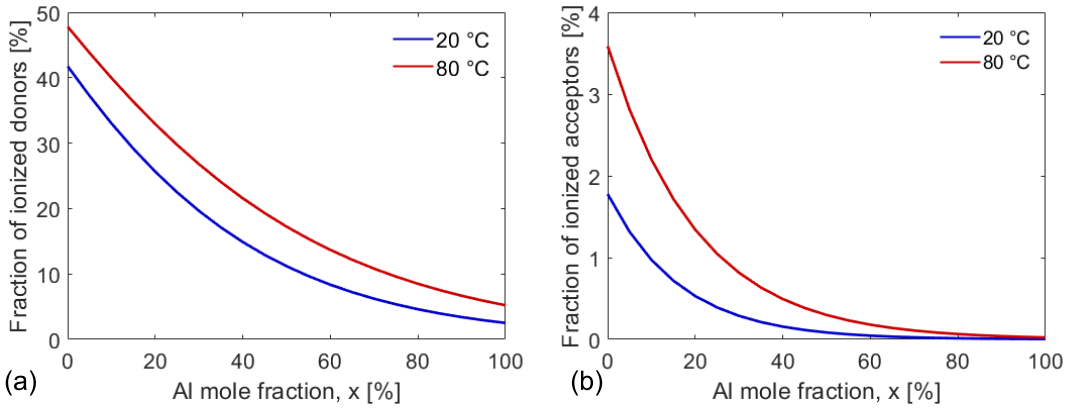

Figure 2.6: Calculated fraction of ionized donors (a) and acceptors (b) in $Al_xGa_{1-x}N$ as a function of Al mole fraction for 20 °C (blue) and 80 °C (red). The calculations assume a fixed donor concentration of $2 \times 10^{18}\,cm^{-3}$ and acceptor concentration of $5 \times 10^{19}\,cm^{-3}$, which yield comparable free carrier densities near room temperature. The decreasing ionization efficiency with increasing Al content highlights the growing difficulty of impurity doping in wide-bandgap AlGaN.

2.5 Thermal conductivity

Heat is conducted in semiconductor materials primarily through vibrations of the crystal lattice, known as phonons. The thermal conductivity of a material is therefore governed by how efficiently these phonons can propagate. This propagation is limited by scattering processes, including phonon-phonon interactions, alloy disorder, defects, and interfaces. As the temperature decreases, phonon scattering rates are reduced, and thermal conductivity typically increases, a trend observed in many crystalline semiconductors.

In the III-nitride system, the binary compounds AlN, GaN, and InN exhibit high thermal conductivities due to relatively low phonon scattering in their pure crystalline form. For instance, single-crystalline GaN can reach bulk thermal conductivities up to $\sim 160\,K\,W^{-1}$ at room temperature, while AlN can exceed $\sim 200\,K\,W^{-1}$ [89]. However, when forming ternary alloys such as AlGaN, InGaN, or AlInN, the introduction of alloy disorder significantly increases phonon scattering and leads to a dramatic reduction in thermal conductivity. For example, AlGaN with 50% Al content can have a thermal conductivity more than ten times lower than either binary endpoint. This reduction is well captured by Adachi's model [90], which interpolates the alloy thermal conductivity based

on the binary values and includes a term for alloy scattering

$$\frac{1}{\kappa_{A_xB_{1-x}C}} = \frac{x}{\kappa_{AC}} + \frac{(1-x)}{\kappa_{BC}} + x(1-x)\Gamma_{AB}. \tag{2.2}$$

where κ_{AC} and κ_{BC} are the binary thermal conductivities and the coefficient Γ_{AB} accounts for lattice disorder. As shown in Figure 2.7, the thermal conductivity exhibits a characteristic bathtub-shaped dependence on composition, with a broad minimum at intermediate alloy fractions due to disorder-induced phonon scattering, as captured by Adachi's model.

In layered structures such as distributed Bragg reflectors (DBRs), which consist of alternating materials with differing thermal conductivities and thicknesses, the effective thermal conductivity becomes highly anisotropic. Heat flows laterally (in-plane) through layers in parallel, and vertically through layers in series. This results in an effective lateral thermal conductivity, κ_r, and vertical conductivity, κ_z, given by the weighted arithmetic and harmonic means, respectively:

$$\kappa_r = \frac{d_1\kappa_1 + d_2\kappa_2}{d_1 + d_2} \tag{2.3}$$

$$\kappa_z = \frac{d_1 + d_2}{d_1/\kappa_1 + d_2/\kappa_2} \tag{2.4}$$

where κ_1 and κ_2 are the thermal conductivities, and d_1 and d_2 the thicknesses of the alternating layers. An implication of this anisotropic averaging is that the lateral thermal conductivity is always greater than or equal to the vertical thermal conductivity, as shown in Paper B

$$\max(\kappa_1, \kappa_2) \geq \kappa_r \geq \kappa_z \geq \min(\kappa_1, \kappa_2). \tag{2.5}$$

This anisotropy is especially relevant in III-nitride VCSELs, where low-κ DBRs suppress vertical heat flow and force most of the heat to spread laterally through the cavity.

Phonon transport across interfaces between different materials in layered structures may be further impeded by thermal boundary resistance, which arises due to mismatch in phonon spectra and acoustic impedance. To account for this, the effective vertical thermal conductivity can be modified as

$$\kappa_z = \frac{d_1 + d_2}{d_1/\kappa_1 + d_2/\kappa_2 + 2R_{int}}, \tag{2.6}$$

where R_{int} is the thermal boundary resistance across a single interface. The factor of two accounts for the two interfaces present in each DBR period, and it is assumed that both interfaces have the same resistance.

In addition, the thermal conductivity in thin layers may be further reduced if the layer thickness becomes comparable to or smaller than the phonon mean free path [91]. In this regime, increased phonon-interface scattering reduces the effective conductivity below the bulk value, a finite-size effect not captured by the expressions above. This suppression is most significant for very thin layers such as quantum wells and potentially DBRs.

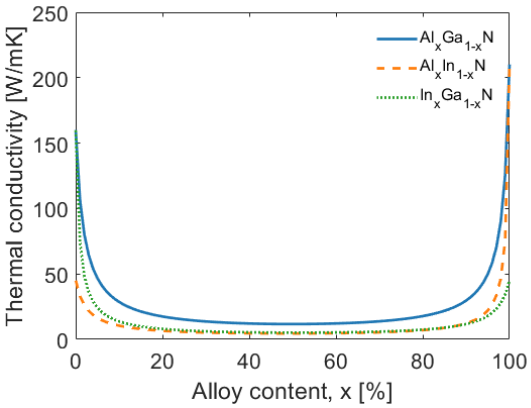

Figure 2.7: Calculated bulk thermal conductivity of ternary III-nitride alloys $Al_xGa_{1-x}N$, $Al_xIn_{1-x}N$, and $In_xGa_{1-x}N$ as a function of alloy composition x, based on Adachi's model [90] with paramters from [89]. The thermal conductivity is significantly reduced at intermediate compositions due to alloy scattering, reaching values more than an order of magnitude lower than in the binary compounds.

Chapter 3

Vertical-cavity surface-emitting lasers

3.1 Operating principle

Vertical-cavity surface-emitting lasers (VCSELs) are a class of semiconductor lasers that emit light perpendicular to the wafer surface, in contrast to edge-emitting lasers (EELs), where light propagates laterally. The defining features of VCSELs arise from their small active volume, which enables low threshold currents, and from their circularly symmetric aperture with low index contrast, which provides circular beam profiles with low divergence. Their surface-normal emission also allows wafer-scale testing and high-density two-dimensional arrays.

The vertical cavity is formed between two highly reflective mirrors, typically distributed Bragg reflectors (DBRs), and act as a Fabry–Pérot resonator. In III-nitride VCSELs, two common mirror configurations are employed: (i) a double dielectric design with dielectric DBRs on both sides of the cavity, and (ii) a hybrid design that combines a dielectric top DBR with a bottom epitaxial DBR. These structures are shown in Fig. 3.1.

In both designs, current is injected in the periphery of the device via intracavity contacts and spread laterally to the QWs in the center part of the device. Once the carrier density in the QW increases to the threshold level where the material gain balances the total optical losses, stimulated emission begins to build up and gradually surpasses spontaneous emission as the dominant process with increasing current injection. The photons are confined vertically between the top and bottom DBRs and the photon density build up coherently within the cavity. Above threshold, lasing takes place, and light is emitted vertically through the partially transmitting outcoupling mirror. Because the active region is extremely short, typically only a few tens of nanometers, VCSELs require very high mirror reflectivities, typically exceeding 99%, to ensure

sufficient photon confinement and optical feedback for lasing.

A representative standing wave pattern is shown alongside the hybrid VCSEL in Fig. 3.1(b) to illustrate the importance of optical field alignment. Discrete longitudinal cavity modes are supported by the vertical cavity, and the QWs are typically aligned with antinodes of the standing wave to maximize the confinement factor, Γ_{QW}, and modal gain. Transverse optical and current confinement are often in III-N VCSELs achieved by an effective index step created by a shallow etched structure using etched mesas or oxide apertures [92].

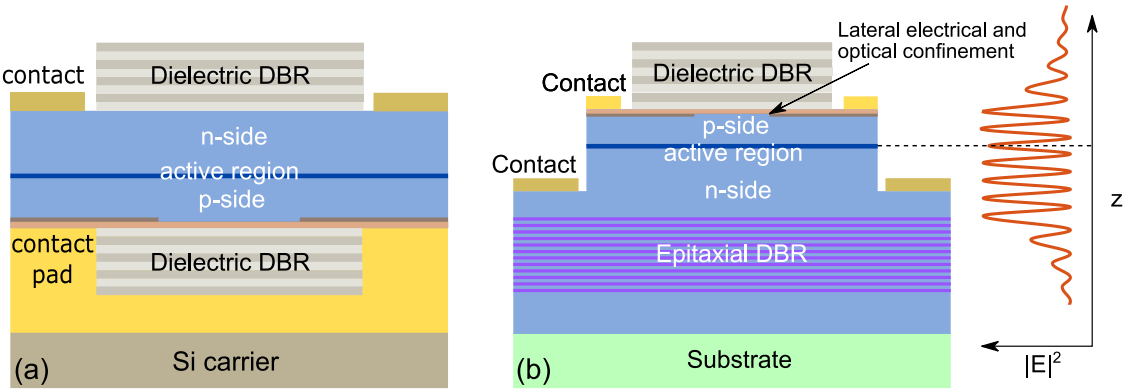

Figure 3.1: Common III-nitride VCSEL structures. (a) All-dielectric configuration, consisting of two dielectric DBRs. (b) Hybrid configuration, with a top dielectric DBR and a bottom epitaxial DBR. In both cases, the vertical optical cavity is formed between the two DBRs, and current is injected through intracavity contacts. A representative standing wave pattern is shown next to the hybrid structure to highlight the importance of aligning the quantum well (QW) gain region with the antinodes of the optical field, thereby maximizing the confinement factor and modal gain.

At threshold, the intracavity optical field must reproduce itself after one round trip in both amplitude and phase, ensuring constructive interference and high photon density. This requirement leads to the threshold gain condition:

$$g_{th} = \frac{1}{\Gamma_{QW}}\left(\alpha_i + \frac{1}{2L_c}\ln\frac{1}{R_1R_2}\right), \tag{3.1}$$

where g_{th} is the material threshold gain, α_i is the absorption loss, L_c is the cavity length, and R_1 and R_2 are the mirror reflectivities. The phase condition ensures that the accumulated round-trip phase shift adds up to an integer multiple of 2π to ensure constructive interference, which in turn sets the allowed longitudinal resonance wavelengths

$$k_0 n_c 2L_c + \varphi_t + \varphi_b = 2\pi m \rightarrow \lambda_m = \frac{2n_cL_c}{m - (\varphi_t + \varphi_b)/(2\pi)}, \tag{3.2}$$

where λ_m is the wavelength of the m-th longitudinal resonance, n_c is the average refractive index of the cavity, and $\varphi_{t/b}$ accounts for the wavelength-dependent

phase shift at the top/bottom DBR. When the mirror center wavelength is designed to coincide with the longitudinal resonance wavelength, the phase shifts $\varphi_t = \varphi_b = 0$ vanish, and the resonance condition simplifies to $nL_c = (m/2)\lambda$. For example, $m = 5$ corresponds to an optical cavity length of $nL = 2.5\lambda$, often referred to as a 2.5λ cavity, while $m = 20$ corresponds to a 10λ cavity.

For III-nitride VCSELs, additional challenges arise due to the relatively low refractive index contrast available in epitaxial DBRs and the poor p-type conductivity of (Al)GaN-based materials. These constraints necessitate the use of dielectric DBRs or hybrid mirror configurations. Thermal management is also critical, given the lower thermal conductivity of certain dielectric materials and the relatively high threshold current densities required in these wide-bandgap devices.

3.2 Distributed Bragg reflectors

Distributed Bragg reflectors, consist of alternating layers of materials with high and low refractive indices. These layers are each designed to have an optical thickness of a quarter-wavelength, resulting in constructive interference and high reflectivity over a range of wavelengths referred to as the stopband, $\Delta\lambda_{stop}$ [93]. High mirror reflectivity is critical in VCSELs because the optical gain per round trip is small, typically around, ~ 1 %. This low gain places stringent demands on the mirror reflectivity, which must often exceed 99 % to satisfy the amplitude condition for lasing [94]. As illustrated in Fig. 3.2, even a small decrease in mirror reflectivity significantly increases the threshold gain required from the quantum wells.

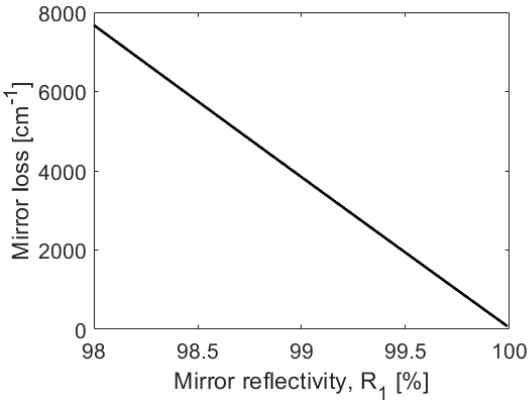

Figure 3.2: Calculated mirror loss using Eq. (3.1), $-\ln(R_1R_2)/(2\Gamma_{QW}L_c)$, for a 10λ blue VCSEL cavity with $R_2 = 99.99\,\%$, $\Gamma_{QW} = 0.74\,\%$, and $L_c = 1790\,\text{nm}$.

3.2.1 Transfer-matrix method

To analyze optical properties of DBRs and VCSEL cavities, the transfer matrix method (TMM) is commonly used. In this formalism, each interface and propagation region is represented by a matrix, and the total response of the structure is determined by multiplying these matrices. Example of a TMM configuration is illustrated in Fig. 3.3(a), where a plane wave is incident on a multilayer stack with partial reflection and transmission at each interface. The total matrix M_{tot} is formed by multiplying the propagation and interface matrices for all layers

$$M_{tot} = M_N M_{N-1} ... M_3 M_2 M_1 = \begin{bmatrix} M_{11} & M_{12} \\ M_{21} & M_{22} \end{bmatrix} \tag{3.3}$$

where M_i are the interface and propagation matrices. For propagation through a layer of refractive index n, thickness d, and incident angle θ, the propagation matrix is

$$M_{prop} = \begin{bmatrix} e^{jk_0 n \cos\theta} & 0 \\ 0 & e^{-jk_0 n \cos\theta} \end{bmatrix}. \tag{3.4}$$

For s (TE) and p (TM) polarized light, the interfaces M_{inter} differ based on the Fresnel reflection and transmission coefficients [95]

$$M^s_{inter} = \frac{1}{2n_r \cos\theta_r} \begin{bmatrix} n_r \cos\theta_r + n_l \cos\theta_l & n_r \cos\theta_r - n_l \cos\theta_l \\ n_r \cos\theta_r - n_l \cos\theta_l & n_r \cos\theta_r + n_l \cos\theta_l \end{bmatrix}, \tag{3.5}$$

and

$$M^p_{inter} = \frac{1}{2n_r \cos\theta_r} \begin{bmatrix} n_r \cos\theta_l + n_l \cos\theta_r & n_r \cos\theta_l - n_l \cos\theta_r \\ n_r \cos\theta_l - n_l \cos\theta_r & n_r \cos\theta_l + n_l \cos\theta_r \end{bmatrix}, \tag{3.6}$$

here n_l and θ_l are the refractive index and angle of incidence on the left side of the interface (incident medium), and n_r and θ_r are the refractive index and angle of transmission on the right side. The reflectivity of a multilayer DBR can then be found from the ratio of matrix components in M_{tot}

$$R = \left| \frac{M_{21}}{M_{22}} \right|^2. \tag{3.7}$$

Fig. 3.3(b) shows both the reflectivity and the reflection phase for a 10-pair SiO_2/HfO_2 DBR calculated using the TMM formalism at normal incidence.

TMM can also be used to determine the threshold gain and resonance wavelength of the VCSEL cavity. Under the condition of no external input, self-sustained oscillation occurs when

$$|M_{22}(\lambda_0, g_{th})| = 0. \tag{3.8}$$

This nonlinear equation can be solved iteratively to determine the resonance wavelength λ_0 and material threshold gain g_{th}.

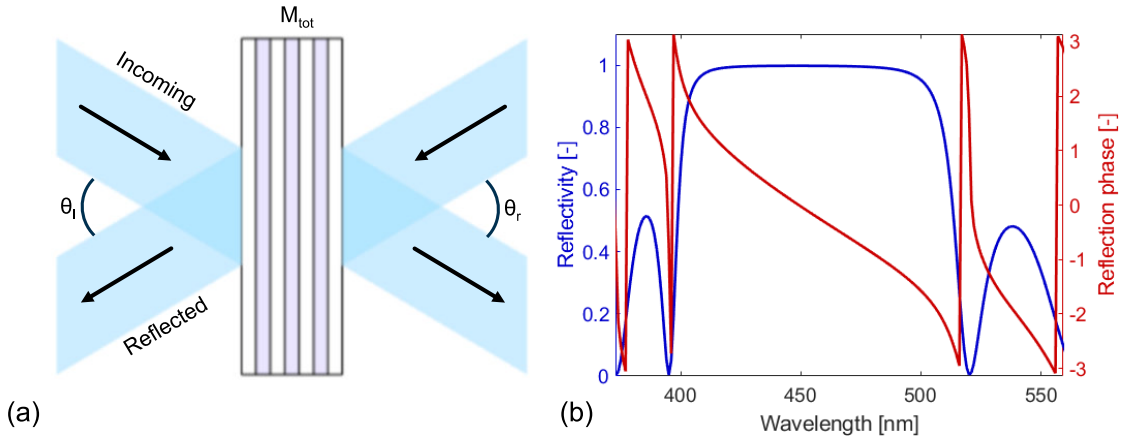

Figure 3.3: (a) Illustration of transfer-matrix method simulation for a multilayer dielectric stack, showing an incident plane wave and its reflected, and transmitted plane waves. (b) Simulated reflectivity (blue) and reflection phase (red) spectrum at normal incidence for a 10-pair SiO_2/HfO_2 DBR centered at 450 nm. The broad stopband with high reflectivity is characteristic of a distributed Bragg reflector, while the phase response provides additional insight into resonance conditions and cavity dispersion.

An alternative way to estimate the total optical losses in the VCSEL cavity is to use the spectral linewidth, defined as the full width at half maximum (FWHM), $\Delta\lambda_{FWHM}$, of the reflectivity dips corresponding to the longitudinal cavity modes. These dips arise from resonant coupling into longitudinal cavity modes, where incident light constructively interferes and is temporarily stored in standing wave patterns inside the cavity. As a result, less light is reflected at those wavelengths, producing sharp dips in the reflectivity spectrum, as illustrated in Fig. 3.4(a). The linewidth of these resonances is inversely related to the photon lifetime, τ_p, via an uncertainty relation

$$\Delta\lambda_{FWHM} = \frac{\lambda_0^2}{2\pi c_0}\frac{1}{\tau_p}. \tag{3.9}$$

Since the photon lifetime is inversely proportional to all optical losses in the cavity and the group velocity, v_g, we can express this as

$$\Delta\lambda_{FWHM} = \frac{\lambda_0^2}{2\pi c_0} v_g \alpha_{tot} = \frac{\lambda_0^2}{2\pi n_g}\big(\alpha_{cav} + \alpha_m + \Gamma_{QW}\alpha_{QW}\big), \tag{3.10}$$

where α_{cav} is the background absorption in the cavity, α_m the mirror loss, α_{QW} the absorption (or gain) in the quantum wells, Γ_{QW} the confinement factor, and n_g the group index, Since this relation is linear in α_{QW}, the material threshold gain can be extracted by simulating the linewidths at two different values of α_{QW}, one which is $\alpha_{QW} = 0$ (transparency)

$$g_{th} = \frac{\Delta\lambda_{FWHM}(\alpha_{QW}=0)}{\Delta(\Delta\lambda_{FWHM})/\Delta\alpha_{QW}} = \frac{1}{\Gamma_{QW}}\Big(\alpha_{cav} + \alpha_m\Big). \tag{3.11}$$

This approach provides an efficient alternative to iterative root-finding methods for $|M_{22}(\lambda_0, g_{th})| = 0$. As shown in Fig. 3.4, applying this method to a 450 nm VCSEL cavity yields a threshold material gain of approximately $1540\,\mathrm{cm}^{-1}$.

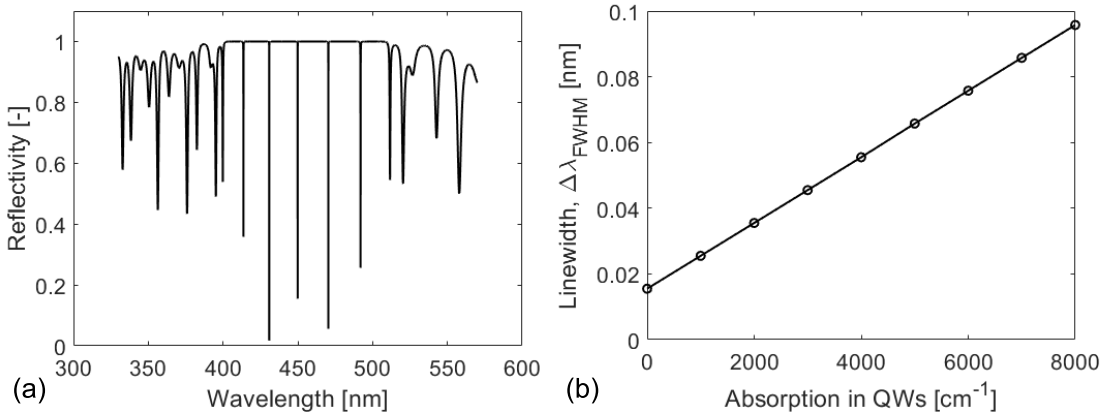

Figure 3.4: TMM-based estimation of threshold gain in a 10λ blue (450 nm) VCSEL with HfO_2/SiO_2 DBRs. (a) Simulated reflectivity spectrum showing sharp dips from longitudinal cavity resonances within the DBR stopband. The dip linewidths relate to the photon lifetime and thereby total optical losses. (b) Extracted linewidth ($\Delta\lambda_{FWHM}$) of the central 10λ mode as a function of absorption in the quantum wells. The linear slope enables extraction of the threshold material gain using Eq. (3.11), yielding $g_{th} \approx 1540\,\mathrm{cm}^{-1}$.

3.2.2 Impact of thickness variations

The exact layer thickness of the individual layers in the DBRs is very important to get the Bragg wavelength of the DBRs at the same wavelength as that of the cavity. If they are not aligned, then the DBR will impart a phase shift proportional to this mismatch. Just a small shift can result in some nm's of shift in the resonance wavelength. If the cavity is designed to support a resonance $\lambda_m = 2n_cL_c/m$, but the Bragg wavelength of the DBRs deviate from this value, or vice versa, then the actual resonance will be shifted. In terms of the design wavelength, λ_m, the new wavelength will be shifted according to

$$\lambda_{\text{shifted}} = \frac{m}{m - (\varphi_t + \varphi_b)/(2\pi)}\lambda_m. \tag{3.12}$$

The shorter the physical cavity (smaller m), the greater impact the phase from the DBRs will have. For longer cavities (larger m) a mismatch between the resonance wavelength and the Bragg wavelength has a smaller impact. Also, since the total phase change across the stopband is 2π, the change in phase with wavelength can be approximated based on the stopband alone $\mathrm{d}\varphi/\mathrm{d}\lambda \approx -2\pi/\Delta\lambda_{stop}$, and analytical expressions for the stopband are readily available [93].

Not only does a variation in the Bragg wavelength change the resonance wavelength of the VCSEL, but it also impacts the overlap losses, or material threshold gain required for lasing. The reflectivity decreases slightly, and the resonance changes the overlap between the standing wave in the cavity and important layers, such as the QWs and highly absorptive layers, such as ITO or tunnel junctions. Figure 3.5(a) shows the impact on a simulated blue 5λ VCSEL with 10/11-pair SiO_2(53.7 nm)/HfO_2(76.3 nm) DBRs as a function of the DBR thickness variation. In Fig. 3.5(a) we can see that the overall material threshold gain of the cavity increases a lot by just allowing all DBR layers to vary by $\pm 5\,\%$. This sharp increase occurs because the Bragg wavelength shifts so far from the cavity resonance at 450 nm that the mode approaches the edge of the DBR stopband, where the reflectivity drops significantly ($\lambda_{\text{Bragg}} \sim 405\,\text{nm}$ and $\lambda_{\text{Bragg}} \sim 495\,\text{nm}$ for a $\mp 12\%$ variation). A $\pm 5\%$ variation of the layer thickness corresponds to a thickness variation of 3.8 nm/2.7 nm for SiO_2/HfO_2, which puts very high requirements for the fabrication of such DBRs for a low-loss VCSEL. In Fig. 3.5(b) we can also see how the field overlap with the QWs and the ITO layer for this blue 10λ VCSEL as a function of the DBR thickness variation.

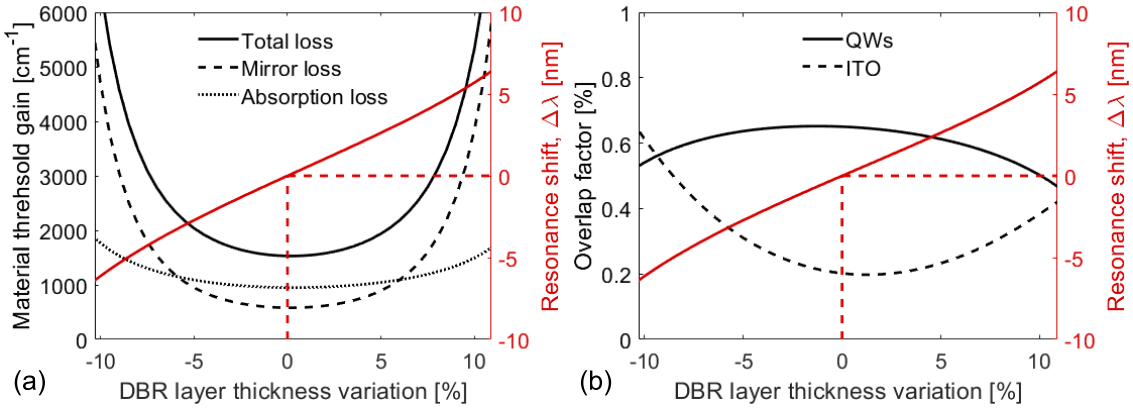

Figure 3.5: 10λ blue (450 nm) VCSEL with 10/11 pair SiO_2/HfO_2 DBRs. (a) Material threshold gain variation as a function of the DBR layer thickness variation. (b) Variation of the QW longitudinal overlap factor Γ_{QW} and the field overlap with the highly absorptive ITO layer.

3.2.3 Phase layer

Terminating a DBR with a metal can be useful: it can improve overall reflectivity by mitigating the effect of surface roughness, which limits the benefit of adding more DBR pairs; in optically pumped VCSELs it enables reflection and recycling of pump light that is not absorbed by the QWs on the first pass; and it is also required when the substrate is removed and the VCSEL is bonded to a carrier. However, placing a metal directly on the last DBR layer introduces

an additional reflection phase that can cause destructive interference within the stopband, visible as a dip in the reflectivity spectrum. To avoid this, a so-called phase layer can be inserted between the DBR and the metal as shown in Fig. 3.6(a). By choosing the phase layer thickness appropriately, the destructive interference is shifted outside the stopband, thereby restoring high reflectivity. The reflection from the metal induces a phase shift φ_2 (which is typically close to π), the propagation through the phase layer also provides a phase shift $2k_0 n_{PL} d_{PL}$, and the sum of the phases must equal an integer of 2π

$$d_{PL} = \frac{2\pi m - \varphi_1 - \varphi_2}{2k_0 n_{PL}}, \tag{3.13}$$

where m is an integer, n_{PL} is the refractive index of the phase layer, φ_1 is the reflection phase between the terminating DBR layer and the phase layer, and φ_2 is the reflection phase between the Al phase layer and the metal reflector. This equation provides an accurate prediction of the required d_{PL} when the metal thickness is thick enough so that there are no reflections from the backside of the metall that reaches the phase layer. If the metal thickness is not thick enough, TMM simulations are required for optimizations, but the above equation still gives a good estimate in these cases as well.

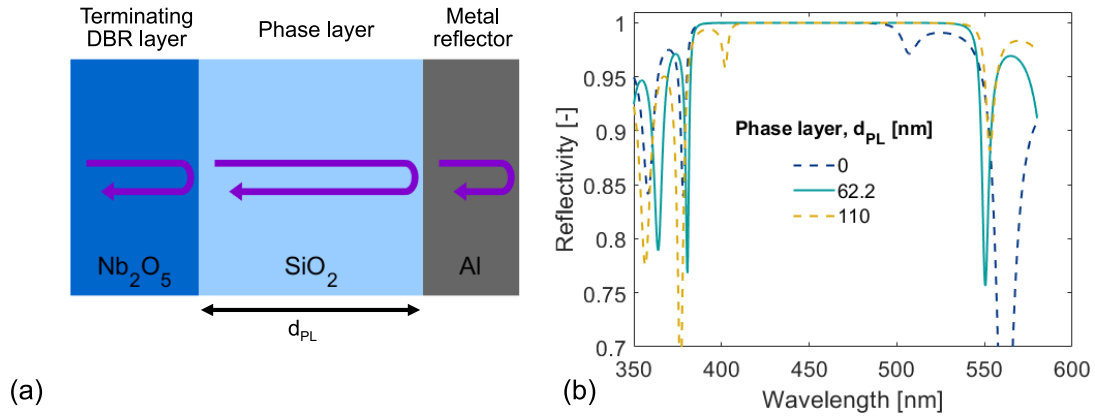

Figure 3.6: (a) Schematic of a phase layer inserted between the terminating DBR layer and a metal reflector to compensate for the reflection phase and avoid destructive interference. (b) Calculated reflectivity spectra for a 10 pair SiO_2/Nb_2O_5 DBR with different SiO_2 phase layer thicknesses, showing a reflectivity dip within the stopband for 0 nm and 110 nm thickness and its suppression with an optimized phase layer thickness of 62 nm.

3.3 Standing-wave effects

The use of double dielectric DBRs requires the removal of the substrate. This can, for instance, be realized by a substrate removal technique using electro-

chemical etching of (Al)GaN sacrificial layers [96, 97]. This enables a post-growth cavity adjustment by adding spacer layers to align specific layers, such as quantum wells at field antinodes and highly absorptive layers such as ITO and etched interfaces at field nodes. However, using spacer layers with a refractive index that differs significantly from the surrounding cavity material can result in pronounced field peaks in the spacer layers adjacent to the DBRs. These peaks arise due to multiple internal reflections and interference within the thin spacer.

For example, using HfO_2 spacers in a GaN VCSEL, results in a strong index mismatch between both the spacer and the cavity interface (HfO_2-GaN) and the spacer and the first low-index DBR layer interface (HfO_2-SiO_2). This leads to partial reflection at both boundaries and the formation of a resonant field enhancement, effectively a Fabry–Pérot-like standing wave within the spacer. This cavity-edge resonance enhances the electric field antinodes near the cavity edges, as shown in Fig. 3.7(a). As a result, the mode intensity shifts toward the interfaces, reducing the overlap with the quantum wells.

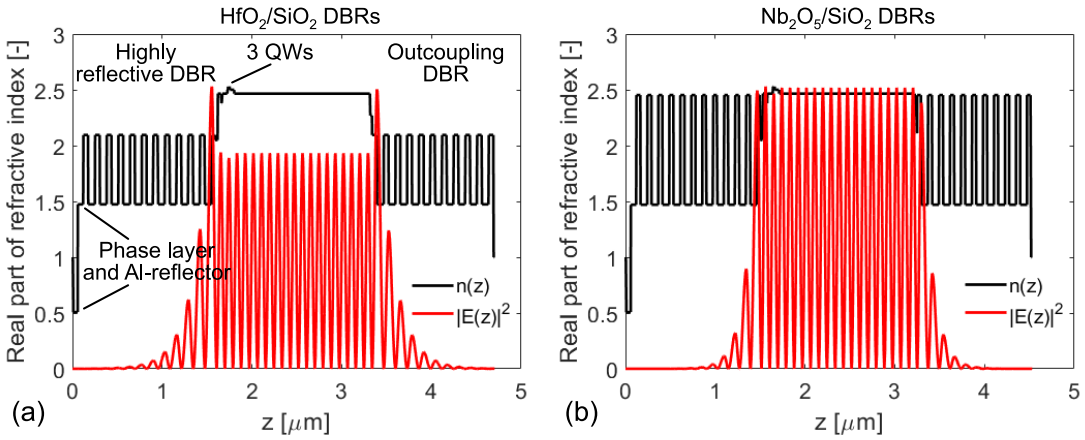

Figure 3.7: Simulated standing-wave profiles in a 10λ GaN-based VCSEL with dielectric DBRs and different spacer layers: (a) HfO_2/SiO_2 DBRs with HfO_2 spacers ($\Gamma_{QW} = 0.65\,\%$), and (b) Nb_2O_5/SiO_2 DBRs with Nb_2O_5 spacers ($\Gamma_{QW} = 0.75\,\%$). The HfO_2 design shows strong electric field antinodes at the cavity edges due to resonant enhancement in the spacer layers. In contrast, the better index match of Nb_2O_5 with GaN suppresses this effect, resulting in a cavity mode that is more centrally confined within the active region. Both designs use 11 bottom (high-reflectivity) and 10 top (outcoupling) DBR pairs.

In contrast, the Nb_2O_5/SiO_2 design with Nb_2O_5 spacers offers a better index match with GaN, suppressing this cavity-edge resonance and yielding a smoother and more centrally confined optical mode with a higher QW confinement factor, as seen in Fig. 3.7(b) Specifically, the QW confinement factor increases from 0.65 % in the HfO_2-based design to 0.75 % in the Nb_2O_5-based design. This corresponds to a $\sim$ 13% reduction in the required material gain for lasing in the Nb_2O_5 case, purely due to the Γ_{QW} enhancement.

3.4 Spectral alignment of mirror stopband, gain and cavity mode

In VCSELs, achieving lasing requires careful spectral alignment of three elements: the longitudinal cavity resonance, determined by the optical thickness of the cavity and the phase response of the mirrors; the DBR stopband, which must provide high reflectivity at the resonance wavelength; and the gain spectrum of the quantum wells, which must provide sufficient gain at the spectral position of the cavity mode.

Unlike edge-emitting lasers, which have long cavities supporting a dense mode spectrum, VCSELs typically support only a few longitudinal modes. As shown in Fig. 3.8(b), these resonances (black vertical lines) are discrete and widely spaced. Lasing occurs only if one of these modes falls within both the gain spectrum and the mirror's high-reflectivity region, and if the total round-trip gain exceeds the losses.

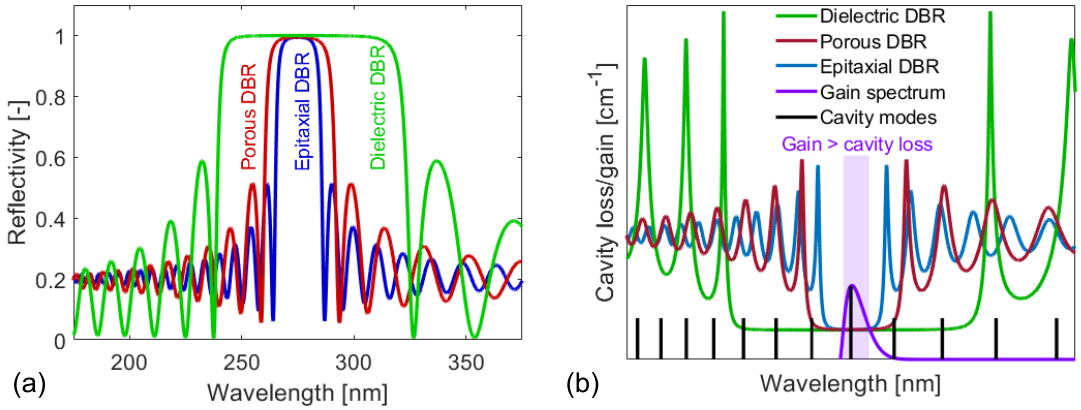

Figure 3.8: (a) Reflectivity spectra of three representative DBR types designed for UV-C VCSELs targeting 275 nm emission: a 10-pair dielectric (green), a 20-pair porous (red), and a 30-pair epitaxial (blue). Dielectric DBRs provide the widest stopband and highest peak reflectivity, offering more flexibility for spectral alignment. (b) Wavelength-dependent cavity loss (including mirror and internal losses) for the same DBR types, overlaid with the gain spectrum (purple) and longitudinal cavity modes (black vertical lines) of a 10λ cavity. Lasing occurs only when a cavity mode coincides with both the gain peak and a region of low cavity loss, as indicated by the shaded region where net gain exceeds total loss.

The spectral overlap between cavity mode, gain spectrum, and DBR stopband (low loss region) is illustrated in Fig. 3.8 for three types of DBRs used in III-nitride VCSELs: dielectric, epitaxial, and porous. The wide stopband of dielectric DBRs makes it easier to spectrally align a cavity mode within the high-reflectivity region. However, achieving lasing still requires that the gain peak also coincides with this mode. In contrast, epitaxial and porous DBRs exhibit narrower stopbands, which restrict the range of viable cavity modes

and increase the sensitivity to fabrication variations. During epitaxial growth, the cavity length commonly varies by $\Delta L/L_c \gtrsim 1\%$. The resulting shift in the cavity resonance wavelength can be estimated based on Eq. (3.2) (neglecting mirror phase) as

$$\Delta\lambda = \frac{\Delta L}{L_c}\lambda_m. \tag{3.14}$$

A 1% variation in cavity length ($\Delta L/L_c = 1\%$) shifts the resonance wavelength by approximately $\Delta\lambda \approx \pm 2.75$nm in the UVC (275 nm) and $\Delta\lambda \approx \pm 4.5$nm in the blue (450 nm). Figure 3.9 shows the simulated material threshold gain as a function of cavity length variation for a 275 nm UVC VCSEL with 10/11-pair SiO_2/HfO_2 DBRs. It is interesting to note that, if the thickness variation is uniform across the cavity, then the penalty in thickness variation of g_{th} can be largely removed by designing the active region to be in the center of the cavity at an optical antinode. The thickness variation during growth on either side of the active region then forces the active region to remain in an antinode and the threshold gain within the designed longitudinal mode number remains close to constant. However, once the resonance condition changes and the cavity supports a new longitudinal mode, the standing wave pattern shifts such that the QWs move from an antinode to a node (or vice versa), causing a sudden increase in threshold gain. This effect is clearly seen in Fig. 3.9(c), where the losses remain almost flat within a given mode order, but increase sharply after a mode jump due to the abrupt change in field overlap with the QWs and any highly absorptive layers. Positioning the QWs near the center of the cavity could be realized in designs utilizing tunnel junctions (TJs), where part of the highly resistive p-side is replaced by n-type (Al)GaN with much higher conductivity. This allows both sides of the cavity to be of similar thickness, enabling the QWs to be positioned near the cavity center.

Misalignment between the longitudinal mode and gain peak leads to increased threshold or suppressed lasing altogether. This sensitivity is further illustrated in Fig. 3.2, where even a ~ 0.5 % drop in reflectivity drastically increases the required material gain. Such constraints underscore the importance of precise cavity and mirror design in III-nitride VCSELs, particularly in the UV-C region where fabrication tolerances are tight [98].

A common complication in this alignment process is the difference between the gain peak and the spontaneous emission peak measured by electroluminescence (EL) or photoluminescence (PL). While the spontaneous emission spectrum is easy to measure experimentally and is often used to infer the gain characteristics in VCSELs, it does not directly indicate the spectral position of maximum gain. This discrepancy arises from the different physical mechanisms underlying spontaneous and stimulated emission. The spontaneous emission spectrum is governed by spontaneous recombination and is shaped by the joint density of states weighted by the carrier occupation probabilities. This tends to favor transitions at higher photon energies, causing the spontaneous emission peak to occur at a shorter wavelength. In contrast, the gain spectrum is shaped by stimulated emission and requires population inversion, formally described

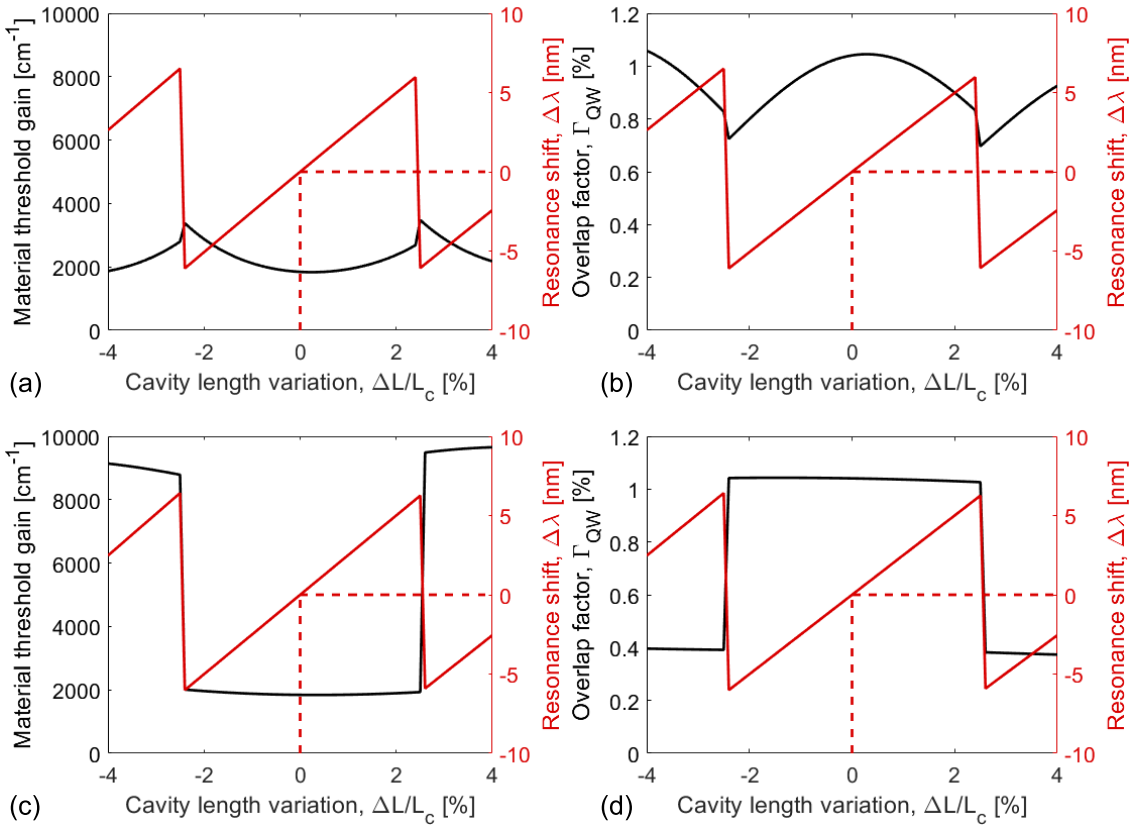

Figure 3.9: Simulated impact of cavity length variation on the optical performance of a 10λ UV-C (275 nm) VCSEL withSiO_2/HfO_2 DBRs. (a) Material threshold gain (black) and cavity resonance wavelength shift ($\Delta\lambda$, red) as a function of relative cavity length variation $\Delta L/L_c$, assuming all variation occurs on the n-side. This corresponds to an asymmetric case where the n-side is much thicker than the p-side, so growth-induced thickness variation accumulates primarily on the n-side. (b) Corresponding quantum well (QW) overlap factor (black) and $\Delta\lambda$ (red) for the same asymmetric case. (c) Threshold gain (black) and $\Delta\lambda$ (red) for a symmetric case where the cavity length variation is distributed equally between the n- and p-sides (of similar thickness). (d) Corresponding QW overlap factor (black) and $\Delta\lambda$ (red) for the symmetric case. Sharp jumps in threshold gain result from a shift in longitudinal mode order, which causes the QWs to transition between node and antinode positions in the standing wave.

by the Bernard–Duraffourg condition, which states that gain occurs when the difference between the electron and hole quasi-Fermi levels exceeds the photon energy. This condition is more easily satisfied at lower photon energies, causing the gain peak to shift to longer wavelengths. As a result, the gain peak is often red-shifted relative to the spontaneous emission peak, even under identical injection conditions.

This distinction is very important in VCSEL fabrication. Since the spontaneous emission spectra is easily measured while the gain spectra is not

directly measurable in most VCSELs, which can lead to unintentional misalignment. Traditional methods for extracting the gain spectrum, such as the Hakki–Paoli technique [99], rely on analyzing amplified spontaneous emission between closely spaced longitudinal modes. While this method is widely used in edge-emitting lasers, it is generally not applicable to VCSELs due to their short cavity lengths and sparse longitudinal mode spacing.

In rare cases, gain measurements using Hakki–Paoli have been tested for specially designed long-cavity VCSELs, where multiple resonances exist within the gain bandwidth. The only example of Hakki-Paoli method in III-nitride VCSELs is the study of a 20λ-long GaN VCSEL [25, 100]. However, this approach is not practical for most VCSELs, which typically use much shorter cavities with large longitudinal mode spacing, making it difficult to resolve multiple resonances within the gain spectrum. An alternative is the segmented contact method [101], an electrically pumped analogue of the variable stripe length technique. Here, the emission length is varied by activating laterally separated contact segments, allowing gain to be extracted from the resulting power–length dependence. However, this requires lateral propagation of light between segments, which can introduce artificial losses unless the structure includes a built-in waveguide. Since standard VCSEL epi lack such vertical confinement, applying this method to III-nitride VCSELs would require waveguide-like modifications to the cavity.

3.5 Cavity dispersion

A VCSEL is designed to support longitudinal resonances determined by the optical thickness of the cavity, forming a Fabry–Pérot-like structure with standing waves along the vertical (z) direction. Due to the DBRs, the structure confines light vertically, allowing only discrete values of the out-of-plane wavevector k_z that fulfill the resonance condition. However, the field is not purely one-dimensional: the transverse mode profile has a finite spatial width, often Gaussian, which implies a corresponding spread in the in-plane wavevector components (k_x, k_y).

This situation is analogous to carrier behavior in quantum wells (QWs), where confinement in one dimension quantizes the allowed energy states in that direction, but leaves the carriers free to occupy a continuum of in-plane momentum states. In the optical case, the DBRs act as mirrors that confine the electromagnetic field along the z-direction, while permitting transverse propagation. As a result, the total wavevector magnitude increases with in-plane wavevector, and the resonance wavelength shifts to lower values with increasing angle θ to the surface normal.

This angular dependence of the resonance is referred to as cavity dispersion. It is often observed in angle-resolved electroluminescence or photoluminescence (k-space) measurements, where the emitted light is recorded as a function of angle and wavelength [30]. Below threshold, the spontaneous emission couples

into a continuum of angular modes that match the resonant condition. A typical k-space measurement reveals parabolic arcs corresponding to these resonances, as illustrated in Fig. 3.10. Above threshold, the emission narrows in both angle and wavelength, forming a sharp, non-dispersive vertical line, indicating lasing.

Importantly, this means that angle-integrated spectra (below threshold), such as those collected by conventional spectrometers without angular resolution, will average over all emission angles within the numeric aperture. Consequently, the spectral maximum in such measurements may differ by as much as $\Delta\lambda \approx -1\,\mathrm{nm}$ from the on-axis resonance ($\theta = 0°$). For accurate identification of the target longitudinal resonance, angle-resolved spectra are required.

The extent of visible cavity dispersion also depends on the width of the spontaneous emission spectrum, mirror bandwidth, and cavity length. Longer cavities support more longitudinal modes, making multiple arcs visible. In addition, dielectric DBRs with broad stopbands allow several of these modes to fall within the low-loss region, whereas epitaxial or porous DBRs typically have narrower stopbands, limiting the number of observable resonances. Nevertheless, k-space measurements are valuable for all VCSELs, as they help identify the lasing mode and allow a reliable threshold determination.

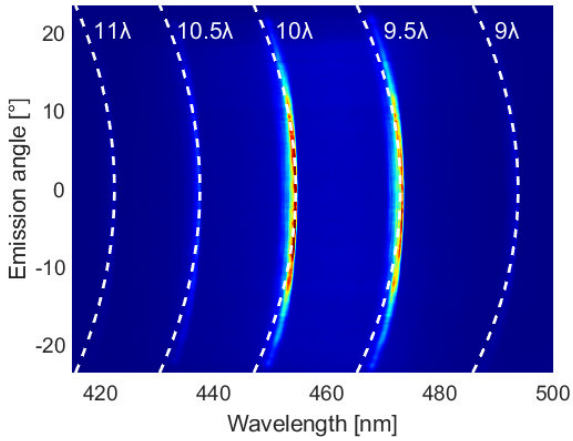

Figure 3.10: Angle-resolved electroluminescence measurement of a blue 10λ VCSEL emitting at ≈ 450 nm, with 10/11-pair SiO_2/HfO_2 DBRs. The spectrum reveals characteristic parabolic arcs corresponding to different longitudinal cavity modes. The overlaid white dashed lines represent the calculated angular dispersion based on Eq. (3.18), showing excellent agreement with the measured data.

The observed dispersion shape arises from the dependence of the cavity mode energy on the in-plane wavevector. Starting from the relation for the wavevector inside the planar cavity $\vec{k} = n_c\vec{k_0} = n_c(k_{x0}, k_{y0}, k_{z0})$, the photon energy becomes

$$E_{ph} = c_0\hbar n_c|\vec{k_0}| = c_0\hbar n_c k_{z0}\sqrt{1 + \frac{k_{x0}^2 + k_{y0}^2}{k_{z0}^2}}, \tag{3.15}$$

where k_{z0} is fixed by the longitudinal cavity resonance and k_{x0}, k_{y0} depend on the transverse propagation angle. For small angles $\tan(\theta_{int}) = \sqrt{k_{x0}^2 + k_{y0}^2}/k_{z0} \approx \theta_{int}$ with θ_{int} the internal propagation angle to the cavity normal/optical axis, and the photon energy becomes

$$E_{ph} \approx c_0 \hbar n_c k_{z0} \Big(1 + \frac{1}{2}\theta_{int}^2\Big). \tag{3.16}$$

Expressed in terms of wavelength using $E_{ph} = hc/(n_c \lambda_{ph})$, this gives

$$\lambda_{ph} \approx \lambda_{z0} \Big(1 - \frac{1}{2}\theta_{int}^2\Big) \tag{3.17}$$

where $\lambda_{z0} = 2\bar{n}_c L_c/[m - (\varphi_t + \varphi_b)/(2\pi)]$ is the longitudinal resonance of the cavity. To connect the internal angle θ_{int} to the measurable external emission angle θ_{air}, we apply Snell's law $n_c \sin\theta_{int} = \sin\theta_{air}$, and for small angles $\theta_{int} \approx \theta/n_c$, we obtain

$$\lambda_{ph} \approx \lambda_{z0} \Big(1 - \frac{1}{2}\frac{\theta_{air}^2}{n_c^2}\Big) \tag{3.18}$$

This parabolic relation explains the characteristic arc shapes observed in angle-resolved k-space measurements, as illustrated in Fig. 3.10. For completeness, a more accurate expression without any small-angle approximation is

$$\lambda_{ph} = \lambda_{z0} \frac{1}{\sqrt{1 + \tan(\arcsin(\sin\theta_{air}/n_c))^2}}, \tag{3.19}$$

though for most practical emission angles ($\pm 20°$), the approximate form is sufficient.

3.6 Proof of lasing

Demonstrating lasing in novel devices, such as III-nitride VCSELs and PCSELs, especially in the UV, requires more than observing a threshold-like behavior or a spectral peak. In high-Q cavities, spontaneous emission can efficiently couple into the cavity modes, potentially giving rise to misleading features in power-dependent spectra. A peak that appears to grow rapidly may resemble lasing, but without a corresponding increase in the coherence of the emitted light or a significant linewidth narrowing, this interpretation can be incorrect.

Figure 3.11 shows an example where a narrow cavity resonance is superimposed on a broad spontaneous emission spectrum. As excitation increases, more spontaneous emission is coupled into the cavity mode, causing the peak to grow. In linear scale, this resembles a threshold-like behavior. However, a logarithmic plot reveals no exponential growth. Depending on how the spectrum is integrated, such effects can produce an artificial kink in the light–output curve.

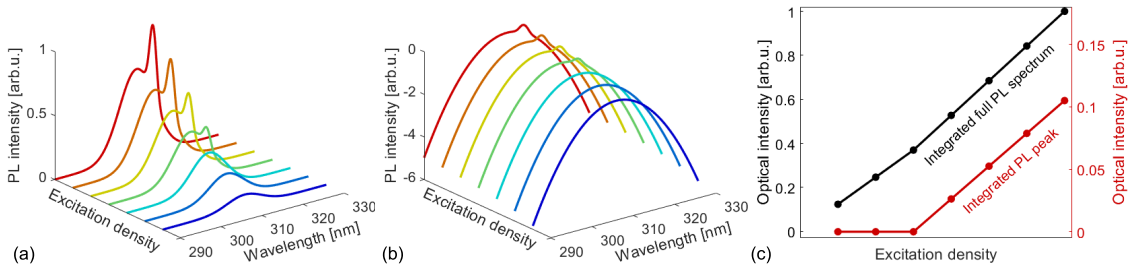

Figure 3.11: Simulated spontaneous emission spectrum superimposed on a cavity resonance with 2 nm FWHM. (a) In linear scale, the growing peak appears to suggest exponential behavior. (b) In logarithmic scale, the peak grows linearly, indicating non-exponential growth. (c) Integrated intensity of the peak and full spectrum versus excitation. A kink-like feature appears when only the peak is integrated, despite the absence of lasing. This illustrates how spontaneous emission coupled into a high-Q cavity can mimic threshold-like behavior.

To avoid such misinterpretations, it is important to evaluate several indicators. Nature Photonics provides a well-recognized checklist for evaluating lasing demonstrations, including evidence of threshold behavior, spectral narrowing, beam profile characterization, polarization, and coherence measurements [102]. While not all criteria may be practical in every case, combining several provides more robust support.

Angle-resolved photoluminescence (or electroluminescence) is especially useful, as it reveals the angular dispersion of the cavity mode and highlights the transition from spontaneous to lasing emission. Below threshold, the emission follows the angularly dispersive cavity mode. Above threshold, one observes a sharp increase in intensity, spectral narrowing, reduced beam divergence, and the appearance of a non-dispersive lasing peak. The transition from a parabolic dispersion to a non-dispersive lasing line is a striking feature that provides a clear and compelling indication of lasing, as illustrated in Fig. 3.12.

3.7 Effective index model and lateral optical confinement

In VCSELs, the concept of an "effective index" is often used to describe the lateral behavior of vertically resonant structures [103]. However, this term can be defined in different ways, and its precise meaning depends on context. One commonly used definition is the field-weighted average index

$$n_{avg} = \frac{\int n(z)|E(z)|^2 dz}{\int |E(z)|^2 dz}, \tag{3.20}$$

which is often used in waveguide theory. While useful, this definition does not account for the optical phase shifts introduced by distributed Bragg reflectors

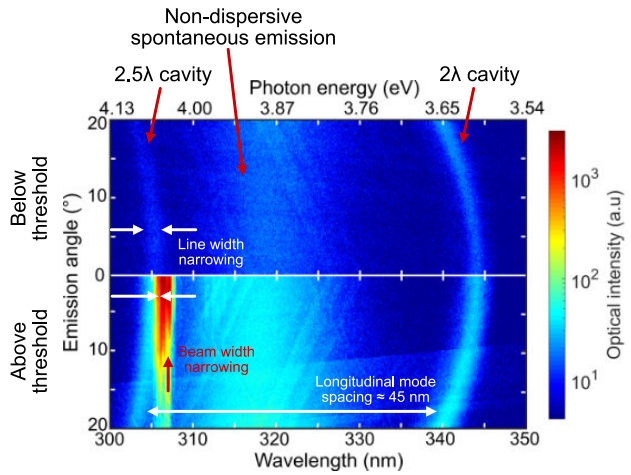

Figure 3.12: Angle-resolved emission of a UVB VCSEL with 2.5λ cavity and double dielectric 310 nm DBRs. Below threshold, two longitudinal cavity modes are visible as curved arcs, reflecting the parabolic angular dispersion of the cavity. Above threshold, a sharp, non-dispersive lasing line emerges with significant intensity, linewidth narrowing, and beam narrowing. In the absence of a lateral aperture, small cavity thickness variations across the device lead to spatial filamentation, with multiple lasing spots emerging simultaneously at different positions on the surface [30]. This measurement is reproduced from [30].

(DBRs), which extend the effective optical path beyond the physical cavity thickness.

In contrast, the resonance-based effective index used in Hadley's effective index model (EIM) [103,104] is defined via the Fabry–Pérot resonance condition

$$n_{eff} = \frac{\lambda_m}{2L_c}\left(m - \frac{\varphi_t + \varphi_b}{2\pi}\right) \tag{3.21}$$

where λ_m is the longitudinal resonance wavelength, L_c is the physical cavity thickness, and $\varphi_{t/b}$ are the top/bottom DBR phase shifts. This resonance-based index captures the full optical structure, including DBR penetration and any local cavity modifications.

3.7.1 Tilt-angle condition for resonant coupling

Lateral variation in the vertical cavity, such as from etching and/or dielectric deposition, can locally alter the effective optical thickness and hence the resonance wavelength [74, 92, 105]. These spatial resonance shifts are modeled as lateral variations in n_{eff}, forming the basis of Hadley's effective index model (EIM) [103, 104].

If the central region supports a Fabry–Pérot resonance at λ_c, and the peripheral region supports $\lambda_c + \Delta\lambda$, with $\Delta\lambda > 0$. A vertically propagating wave in the center resonates at λ_c, but if its wavevector tilts to angle θ_c, the vertical component becomes $k_{z,c} = 2\pi\cos\theta_c/\lambda_c$. For this wave to couple into the

peripheral region, it must match the resonance condition there

$$\frac{2\pi}{\lambda_c}\cos\theta_c = \frac{2\pi}{\lambda_c + \Delta\lambda} \rightarrow \cos\theta_c = \frac{\lambda_c}{\lambda_c + \Delta\lambda}. \tag{3.22}$$

This expression determines the minimum tilt angle θ_c at which coupling (and therefore lateral leakage) can occur. Importantly, such leakage is only possible if $\Delta\lambda > 0$, i.e. if the peripheral region supports a longer-wavelength (lower-energy) resonance than the center. In such a case, a portion of the optical field in the central region can leak laterally, causing increased diffraction loss. This configuration is referred to as anti-guided, as light preferentially escapes the central aperture. Conversely, if the central region supports a longer resonance wavelength ($\Delta\lambda < 0$), the field remains confined, resulting in a guided configuration. These two cases are illustrated schematically in Fig. 3.13, where the relative cavity lengths determine whether the mode is laterally confined or leaks into the periphery.

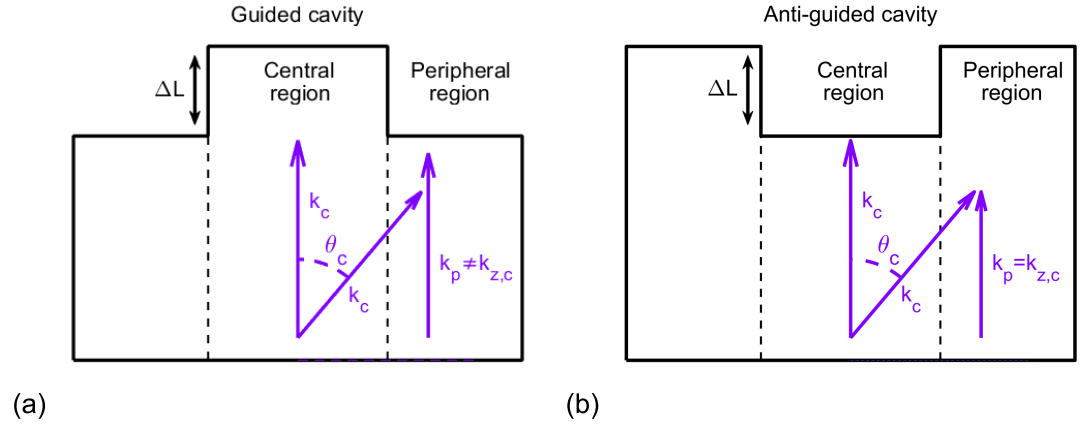

Figure 3.13: Schematic of a (a) guided and (b) anti-guided VCSEL cavity. The lateral depression ΔL alters the optical thickness, shifting the Fabry–Pérot resonance. In (a), the central region has a longer cavity length ($\lambda_c > \lambda_p$), producing a higher effective index than the peripheral region, leading to lateral confinement of the mode. In (b), the central region is thinner ($\lambda_c < \lambda_p$), resulting in light leakage into the peripheral region, corresponding to an anti-guided configuration. The wavevector components illustrate how phase matching governs lateral coupling.

3.7.2 Snell's law analogy and the origin of the effective index step

Interestingly, the form of the phase-matching expression in Eq. (3.22) resembles Snell's law [106]. Although there is no physical material interface between the central and peripheral regions, we can model the the central region as having refractive index n_c, and the peripheral region as $n_c + \Delta n$, where the index contrast is inferred from the red-shifted resonance. If the peripheral region

supports a longer resonance wavelength, as in the anti-guided case, then light in the peripheral region will experience total internal reflection (TIR) at angle θ_c when incident on the central region. Applying Snell's law

$$n_c \sin(90^\circ) = (n_c + \Delta n) \sin(90^\circ - \theta_c) \rightarrow \cos\theta_c = \frac{n_c}{n_c + \Delta n}. \tag{3.23}$$

Combining this with observation with Eq. (3.22) we can associate the resonance shift between the two regions to a an effective index difference

$$\frac{\Delta n}{n_c} = \frac{\Delta \lambda}{\lambda_c} \tag{3.24}$$

Physically, this angle θ_c corresponds to the critical angle for total internal reflection (TIR) at a lateral boundary between effective indices $n_c + \Delta n$ and n_c. In this analogy, rays in the peripheral (higher-index) region impinging on the lower-index central region at angles beyond θ_c are totally internally reflected. This Snell-like picture naturally introduces the concepts of anti-guiding and guiding: if the effective index is higher in the peripheral region than in the center, light tends to escape laterally, corresponding to an anti-guided configuration. Conversely, if the effective index is higher in the center, light is confined, and the structure behaves as a laterally guided cavity. For good lateral confinement, the central region should therefore have a higher effective index (i.e., a longer Fabry–Pérot resonance wavelength) than the peripheral region, ensuring guided operation and minimizing diffraction loss. Note that in this derivation, a positive index step $\Delta n > 0$ corresponds to an anti-guided cavity, where the effective index is higher in the peripheral region. This choice is made to match the condition for lateral leakage. However, in much of the VCSEL literature and simulation practice, the sign convention is reversed: $\Delta n > 0$ is typically used to denote a guided cavity with a higher effective index in the center. This conventional notation will be used throughout the remainder of this thesis.

3.7.3 Angular diffraction loss in anti-guided VCSELs

To illustrate the resonant diffraction loss mechanism, we approximate the angular emission of the intracavity field using an Airy-like distribution—motivated by the diffraction pattern of a circular aperture

$$E(\theta) \propto \frac{2J_1(ka \sin\theta)}{ka \sin\theta}, \tag{3.25}$$

where a is the aperture radius, θ is the propagation angle relative to the optical axis, and J_1 is the Bessel function of the first kind of order one. This provides a simple, yet instructive, model of how the angular content of the field relates to the possibility of lateral leakage. Specifically, leakage occurs when the angular components of the field overlap with the resonance condition in the periphery,

which corresponds to a certain launch angle θ_c derived from the effective index step.

Figure 3.14(a) illustrates the modeled angular content of the field, where shaded bands indicate the angular ranges that satisfy the resonance condition for two different values of Δn_{eff}. The corresponding round-trip loss, estimated by integrating the angular content over these bands, is shown in Fig. 3.14(b). This lateral loss increases sharply when the central and peripheral cavities become resonant at an oblique angle, corresponding to an anti-guided structure ($\Delta n_{eff} \lesssim 0$). In contrast, in the guided regime ($0 \lesssim \Delta n_{eff} \lesssim 0.053$), there is no angle for resonant coupling and lateral leakage is absent. Similar behavior has been reported in more rigorous numerical studies using three-dimensional beam-propagation methods (3D-BPM) [92].

The leakage loss exhibits an oscillatory dependence on Δn_{eff}, due to the oscillations of the Airy function. These modulations reflect how the angular components of the field align with the allowed leakage angles. As Δn_{eff} becomes more negative, the resonant angle shifts to larger values, where the Airy tail diminishes, reducing the efficiency of power coupling and, thus, the leakage fraction. Similar oscillatory behavior in simulated diffraction losses has been reported in the literature [107].

As the effective index step becomes more negative in an anti-guided cavity (i.e. increasing $|\Delta n_{eff}|$ with $\Delta n_{eff} < 0$), the peripheral resonance $\lambda_{p,m}$ shifts to longer wavelengths. When this index step becomes sufficiently large in magnitude, the next adjacent peripheral mode, with a shorter wavelength $\lambda_{p,m+1}$, may become closer to the central $\lambda_{c,m}$, causing the structure to switch from anti-guided to guided behavior [92]. This switching of the closest peripheral resonance occurs when the center mode lies midway between $\lambda_{p,m}$ and $\lambda_{p,m+1}$, i.e. $|\lambda_{p,m} - \lambda_{c,m}| = |\lambda_{c,m} - \lambda_{p,m+1}|$. The effective index step required to cause this transition can be approximated using Eq. (3.24) as $\Delta n_{eff} = -(n_c/\lambda_c)(\Delta\lambda/2)$ where $\Delta\lambda/2 = (\lambda_{p,m} - \lambda_{p,m+1})/2$ is the average separation between central cavity resonance λ_c, m and the two adjacent peripheral modes. Similarly, for a guided cavity transitioning to an anti-guided one, the switch occurs when $|\lambda_{c,m} - \lambda_{p,m}| = |\lambda_{p,m-1} - \lambda_{c,m}|$, and the required effective index step is again $\Delta n = (n_c/\lambda_c)(\Delta\lambda/2)$, where $\Delta\lambda/2 = (\lambda_{p,m-1} - \lambda_{p,m})/2$.

For example, in a 7.5λ VCSEL ($m/2 = 7.5$) with hybrid DBRs and $\lambda_{c,m} = 420\,\text{nm}$ and $n_c = 2.49$ (with the structure described in detail in [92]), the transition from guided to anti-guided behavior occurs near $\Delta n_{eff} \approx 0.053$ (in addition to the switch at $\Delta n_{eff} \approx 0$), as illustrated in Fig. 3.14(b). Similarly, the switch from anti-guided to guided occurs near $\Delta n_{eff} \approx -0.053$.

While this model does not account for all scattering and diffraction mechanisms, it captures the key trends and physical intuition behind resonant lateral leakage in anti-guided cavities. Importantly, it highlights how small variations in Δn_{eff} can dramatically impact optical losses. The conditions $\Delta n_{eff} \approx 0$ and $\Delta n_{eff} \approx (n_c/\lambda_c)(\Delta\lambda/2)$ mark critical transitions between guided and anti-gudied regimes, and should be avoided in VCSEL designs to minimize the risk of large diffraction loss. This effect is well documented in litera-

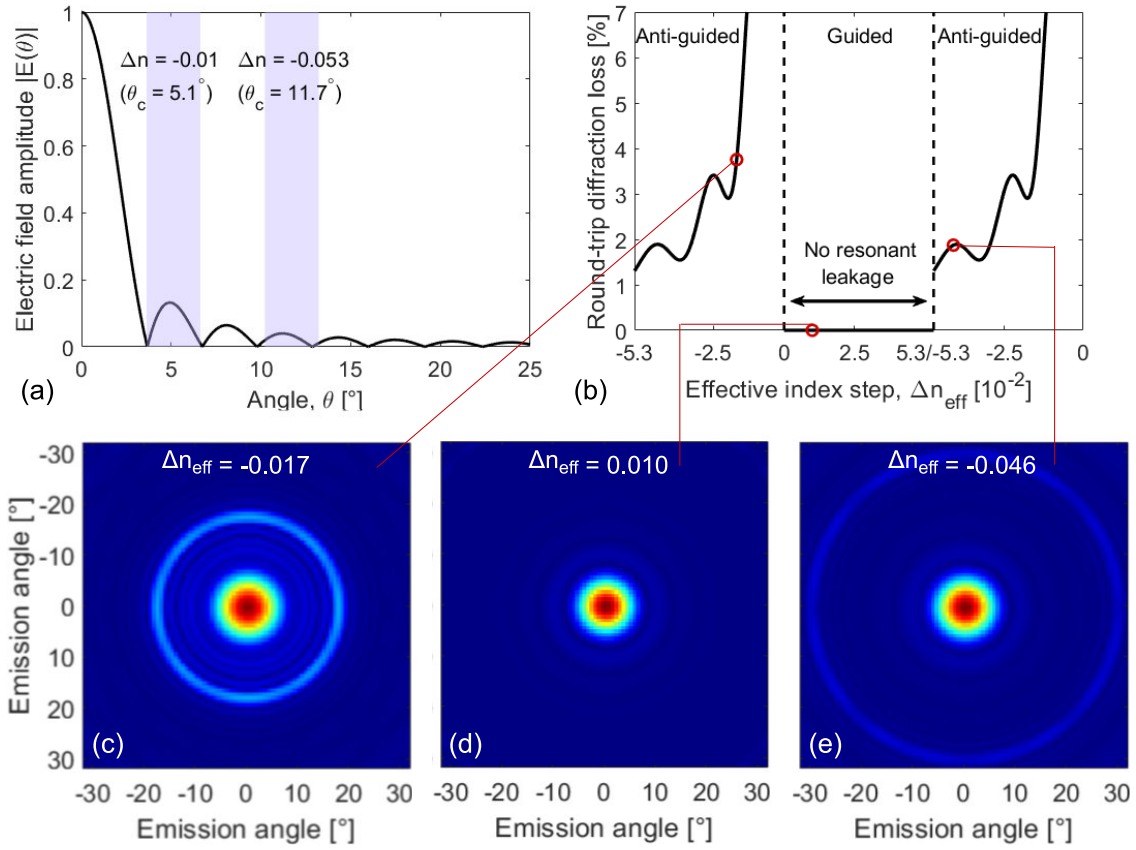

Figure 3.14: (a) Modeled angular content of the intracavity field, based on the far-field pattern of a circular aperture (Airy function). The shaded regions correspond to angular bands around the resonant coupling angle θ_c for two different effective index steps $\Delta n_{eff} = -0.01$ and -0.053. (b) Estimated round-trip diffraction loss as a function of effective index step. The loss is computed as the fraction of the angular power spectrum that satisfies the resonance condition, integrated over a $\pm 1.5°$ window around the resonant angle. The central region ($0 \lesssim \Delta n_{eff} \lesssim 0.053$), where no resonant leakage occurs, corresponds to a guided cavity, whereas lateral leakage increases rapidly in the anti-guided regions ($\Delta n_{eff} \lesssim 0$ and $\Delta n_{eff} \gtrsim 0.053$). (c-e) Simulated far-field intensity distributions using 3D-BPM for a 7.5λ blue VCSEL with hybrid DBRs and a 4 µm aperture, at different effective index steps: (c) $\Delta n_{eff} = -0.017$ (anti-guided), (d) $\Delta n_{eff} = 0.010$ (guided), and (e) $\Delta n_{eff} = -0.046$ (anti-guided). Circular rings in (c) and (e) arise from resonant leakage, which is absent in the guided case (d).

ture [74, 92, 105], with fabricated devices that use anti-guided cavities showing substantially higher threshold currents ($\sim 3x$) compared to their guided counterparts [108].

The effect of the resonant leakage can be observed in the far-field emission of the VCSEL. The trapped light at the resonant angle θ_c in the peripheral cavity exits the VCSEL at an angle that can be approximately determined

using Snell's law [92]

$$n_c \sin\theta_c = \sin\theta_{air}. \tag{3.26}$$

For example, Fig. 3.14(c-e) shows the calculated far-field using 3D-BPM for three different index steps ($\Delta n = -0.017$, $\Delta n = 0.010$, and $\Delta n = -0.046$). These effective index steps are realized using a standard SiO_2 aperture [109], where varying the etch depth of the p-GaN and the thickness of the deposited dielectric allows tuning Δn_{eff}. The circular ring that appears around the main lobe at angle θ_{air} in the anti-guided structures is a clear signature of resonant leakage. By combining Eq. (3.22) and Eq. (3.26), we find that the light originating from the leakage angle θ_c exits at angles $\theta_{air} = 17°$ for $\Delta n = -0.017$ and $\theta_{air} = 28°$ for $\Delta n = -0.046$, in very good agreement with the far-field patterns obtained from 3D-BPM in Fig. 3.14(c-e). For the guided structure with $\Delta n = 0.019$, no such leakage angle can be observed in the far-field pattern.

These far-field features correspond to significant differences in simulated material threshold gain. For the anti-guided case with $\Delta n = -0.017$, the threshold gain is $\sim 5000\,\text{cm}^{-1}$, while for the guided case with $\Delta n = 0.0190$, it drops to $\sim 2400\,\text{cm}^{-1}$. In the strongly anti-guided case with $\Delta n = -0.046$, the threshold gain is $\sim 3200\,\text{cm}^{-1}$. These values can be compared to a 1D EIM simulation of the same structure, which neglects diffraction loss and yields a material threshold gain of $\sim 1900\,\text{cm}^{-1}$. The $\sim 500\,\text{cm}^{-1}$ higher loss in the guided case compared to the 1D model is caused by the small aperture diameter of 4 µm used in the simulations, which increases diffraction losses. This highlights the threshold penalty associated with resonant lateral leakage in anti-guided cavities, and the importance of carefully selecting Δn_{eff} to avoid such regimes.

3.8 Thermal effects

The thermal behavior of VCSELs plays a crucial role in their performance, influencing threshold current, wavelength stability, and device lifetime. During operation, heat is generated through nonradiative recombination and resistive losses. This heat must be effectively dissipated to avoid elevated cavity temperatures that can degrade performance or inhibit lasing altogether. Heat management is a bit more challenging in III-nitride VCSELs compared to EELs due to the non-electrically conductive and thermally insulating DBR. However, a VCSEL's lasing wavelength shifts less with temperature.

This reduced wavelength shift arises because the lasing wavelength in VCSELs is primarily set by the optical cavity resonance, which changes only slowly with temperature. In contrast, the lasing wavelength in EELs closely follows the gain peak and therefore shifts much more rapidly as temperature increases. The reduced wavelength shift of VCSELs is highly desirable for applications such as gas sensing [110], atomic clocks [111], spectroscopy [112], and fiber-optic communication systems [113, 114], where precise wavelength control is important.

As illustrated in Fig. 3.15, both the gain peak and the cavity resonance shift toward longer wavelengths with increasing temperature. The gain peak redshifts primarily due to bandgap shrinkage (described by Varshni's relation) and the broadening of carrier distributions at elevated temperatures. In contrast, the cavity resonance shifts due to an increase in the optical thickness of the cavity, caused by the positive thermo-optic coefficient ($dn/dT > 0$) of most semiconductor materials. This leads to a redshift in the cavity resonance. However, the rate of this redshift is typically slower than that of the gain peak.

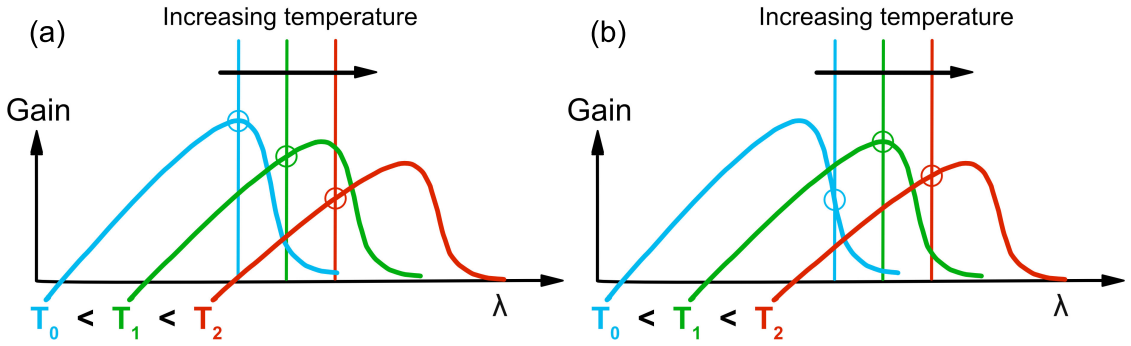

Figure 3.15: Illustration of thermal wavelength shifts in VCSELs. (a) If the cavity mode and gain peak are aligned at room temperature, increasing temperature causes the gain peak to redshift faster than the cavity mode, leading to detuning and reduced modal gain. (b) By designing the cavity mode to be slightly detuned from the gain peak at room temperature, the two can align at the target operating temperature, maintaining higher modal gain and reducing the threshold current. Colored vertical lines indicate the cavity resonance wavelength at different temperatures.

The mismatch in thermal shift rates between the cavity and the gain peak can lead to detuning, where the lasing wavelength no longer coincides with the maximum gain. This reduces the modal gain and increases the threshold current, as shown in Fig. 3.15(a). This effect becomes increasingly important at elevated temperatures, especially in III-nitride VCSELs where longitudinal mode spacing is large and there may only be one viable resonance within the gain bandwidth. As a result, even modest thermal shifts can significantly impact performance. To mitigate this, one strategy involves deliberately designing the VCSEL so that the cavity mode is initially detuned from the gain peak at room temperature, allowing the two to align at the desired elevated operating temperature as shown in Fig. 3.15(b). This approach can mitigate thermal misalignment and stabilize the threshold current over a range of temperatures.

3.8.1 Thermal resistance

A key metric for characterizing the thermal performance of VCSELs is the thermal resistance, R_{th}, defined as the temperature rise per unit of dissipated

power [115]

$$R_{th} = \frac{\Delta T}{P_{diss}}. \tag{3.27}$$

This value reflects how effectively heat can be extracted from the active region and depends on both material properties, device geometry, and where heat is generated. In practice, accessing the internal cavity temperature directly is difficult, so thermal resistance is typically extracted from the shift in lasing wavelength with increasing power and heat-sink temperature. Using the wavelength as a thermometer, the thermal resistance is often determined via [9]

$$R_{th} = \frac{\Delta\lambda/\Delta P_{diss}}{\Delta\lambda/\Delta T_{hs}}. \tag{3.28}$$

Here, $\Delta\lambda/\Delta P_{diss}$ is the shift in lasing wavelength with dissipated power, and $\Delta\lambda/\Delta T_{hs}$ is the shift of the lasing wavelength with heat sink temperature (typically extracted in pulsed operation to avoid Joule heating). This method assumes that the shift in lasing wavelength is dominated by heating of the active region, and that the resonance wavelength increases linearly with both dissipated power and heat-sink temperature. However, this assumption is not valid for VCSEL designs in which the lasing wavelength has been athermalized, such as the UVB VCSEL described in Paper A. In such structures, the negative thermo-optic coefficient of materials like HfO_2 are used to counteract the redshift from the cavity, resulting in a stabilized or even blue-shifting lasing wavelength with temperature, $\Delta\lambda < 0$. In these cases, the lasing wavelength is no longer a reliable tool for probing the internal cavity temperature, and thermal resistance must be evaluated by alternative means.

Thermal resistance in VCSELs is typically higher than in edge-emitting lasers due to their compact vertical architecture, which limits pathways for heat extraction. A major contributor is the use of multilayer DBRs with low effective thermal conductivity, especially in III-nitride VCSELs, which impedes vertical heat transport. Efficient heat management often involves placing heat sinks closer to the active region without disturbing optical properties, optimizing layer thicknesses, and improving thermal conductivity near the active region.

3.8.2 Pulsed operation

In some VCSEL applications and for first demonstrations, pulsed operation is used to reduce the effects of self-heating, and avoid processing complexities such as current spreading, contact formation, and thermal management. To minimize device heating during pulsed operation, one can use the lumped thermal model [116] to determine pulse durations that ensure both a low peak temperature and negligible residual heating. Instead of solving the partial differential heat equation, we reduce it to a first-order ordinary differential equation for the average temperature $T(t)$ in the region of interest, typically the active region or mesa region. The model is described in Appendix A, and is governed by the

balance between the input power and the rate at which heat leaves the system, which is proportional to the temperature difference between the device and its surroundings, T_{amb}.

During the on-pulse heat accumulates, and during the off-pulse the device cools down with a time-constant

$$\tau = R_{th}\rho c_p V = R_{th}C_{th}, \tag{3.29}$$

where $C_{th} = \rho c_p V$ is the thermal capacitance, which quantifies the amount of heat required to change the temperature by a certain amount, and R_{th} represents the difficulty of heat flowing out of the system.

The peak temperature rise during the heating pulse is given by $\Delta T_{on,max} = P_0 R_{th}[1 - \exp(-t_{on}/\tau)]$ which yields an upper bound on the allowed time

$$t_{on} \leq -\tau \ln\Big(1 - \frac{\Delta T_{on,max}}{P_0 R_{th}}\Big), \tag{3.30}$$

During the off-time, the device cools exponentially. To ensure the temperature returns to within a fraction $\epsilon \ll 1$ of ambient, we require $\Delta T_{off,min} = \Delta T_{on}\exp(-t_{off}/\tau) \leq \epsilon \Delta T_{on}$ which yields a lower bound on the allowed time

$$t_{off} \geq -\tau \ln(\epsilon) \tag{3.31}$$

Suppose the target is to keep the maximum temperature rise below $\Delta T_{on,max} = 10\,^{\circ}\mathrm{C}$, and ensure that the temperature returns to within $\epsilon = 0.1\%$ of ambient by the end of the off-period. For a blue (450 nm) 10λ VCSEL with $R_{th} = 710\,\mathrm{K\,W^{-1}}$, and time constant $\tau = 200\,\mathrm{ns}$ (using values from Table 3.1), this results in $t_{on} < 190\,\mathrm{ns}$, $t_{off} > 1.4\,\mu\mathrm{s}$, and a duty cycle of $D = t_{on}/(t_{on}+t_{off}) \approx 10\,\%$. It is known that these lumped thermal models generally overestimates how quickly the system cools-down during the off pulse [116], and the duty cycle is typically kept below 1 % to avoid heating.

Table 3.1: Parameters used for estimating the time-constant in III-nitride VCSELs. The specific heat, c, and density, ρ, for AlN and GaN are taken from [117]. For InN the specific heat is taken from [118] and the density from [119].

Material	AlN	GaN	InN
c [$\mathrm{J\,kg^{-1}\,K^{-1}}$]	600	490	320
ρ [$\mathrm{kg\,m^{-3}}$]	3230	6150	6810

Chapter 4

Frontiers in III-N VCSELs

VCSELs are a class of semiconductor lasers in which light emission occurs perpendicular to the substrate surface. They offer several compelling advantages over EELs, including low threshold currents, circular and low-divergence output beams, wafer-scale testing capability, and potential for high-density 2D array integration. These attributes make VCSELs attractive for applications ranging from high-resolution displays and optical interconnects to biomedical sensing and atomic clocks.

In the visible and ultraviolet spectral regions, VCSELs based on group-III nitrides are of particular interest. GaN-based blue VCSELs have reached a level of maturity sufficient for introduction to the commercial market, with perhaps the only remaining hurdles being robust single-mode operation and reliable polarization control that is required for some applications. In contrast, UVB and UVC VCSELs remain in earlier stages of research, with devices still relying on optical pumping. Achieving high-performance, electrically injected UV VCSELs remains challenging due to several material and structural limitations, including poor mirror reflectivity, inefficient current injection, high thermal resistance.

This chapter reviews recent progress in III-nitride VCSELs and the design strategies developed to overcome these challenges. Section 4.1 provides an overview of the state of the art, highlighting approaches for mirror design, electrical injection, and the best-performing blue and UV devices reported to date. Section 4.2 focuses on the specific challenges of heat management in UVC VCSELs, presenting strategies to reduce thermal resistance and improve device reliability (Paper B). Section 4.3 discusses the implementation of athermal cavity designs based on negative thermo-optic coefficient materials, demonstrating stable lasing over a wide temperature range (Paper A). Finally, Section 4.4 presents unpublished simulation results addressing polarization control and single-mode operation strategies.

4.1 Progress in III-nitride VCSELs

Developing VCSELs in the III-nitride material system is particularly challenging compared with the well-established AlGaAs system, due to large lattice mismatches between available nitride compounds, poor p-type conductivity, strong polarization fields, and the absence of native oxides for aperture definition. As a result, III-nitride VCSELs require fundamentally different design approaches for DBRs, electrical injection, and aperture formation.

4.1.1 Mirror designs

The first optically pumped III-nitride VCSELs used two epitaxial $Al_{0.40}Ga_{0.60}N/Al_{0.12}Ga_{0.88}N$ DBRs [120], but this approach was quickly abandoned due to the poor p-type conductivity of (Al)GaN, which limits vertical current injection and makes it difficult to spread current laterally in the p-side. Most designs today use either a hybrid DBR structure which combines a bottom epitaxial DBR with a top dielectric mirror, or an all-dielectric DBR design, in which both top and bottom mirrors are dielectric. In both cases, current is injected through intracavity contacts on both the p- and n-sides. An exception is a demonstration by Meijo, where an n-doped epitaxial DBR was used, removing the need for an intracavity contact on the n-side [121].

Hybrid blue-emitting VCSELs typically use a bottom AlInN/GaN DBR, which can be grown nearly lattice-matched to GaN by adjusting the indium content to around 18%. This allows high-quality growth of up to 30–40 pairs using metal–organic vapor phase epitaxy [122–126]. However, the refractive index contrast is relatively low, which leads to a narrow stopband and many pairs are required to achieve a reflectivity above 99%.

In contrast, VCSELs with all-dielectric DBRs, can achieve similar or higher reflectivity with far fewer pairs and a wider stopband, owing to their much larger refractive index contrast. Common material combinations include SiO_2 as low-index material with high-index materials such as TiO_2 [127], Nb_2O_5 [109], Ta_2O_5 [128], ZrO_2 [129], and HfO_2, deposited by sputtering or evaporation. Since these materials are non-crystalline, there are no lattice-matching requirements.

One drawback shared by both epitaxial and dielectric DBRs is their poor thermal conductivity, as discussed in paper B, which makes heat extraction difficult. Increasing the cavity length can help improve lateral heat dissipation through the high thermally conductive GaN cavity material. However, in devices with planar DBRs, whether epitaxial or dielectric, the cavity length can not be increased too much because diffraction losses, which increase with cavity thickness [130]. To overcome this trade-off, Sony has demonstrated a VCSEL design using a top dielectric mirror with a curved surface to form a stable optical resonator [54, 131–136]. This allows for much longer cavities of up to 20 µm ($\sim 100\lambda$) while avoiding large diffraction losses [130]. By enabling longer cavities with improved thermal spreading, the curved mirror design of-

fers a promising path forward for high-power and high-temperature operation in III-nitride VCSELs, but care has to be taken to not end up with multiple longitudinal modes or mode hopping [137].

4.1.2 Approaches for electrical injection

The first electrically injected III-nitride VCSELs, using either a hybrid design [25] or an all-dielectric design [26], were demonstrated more than a decade after the first optically pumped devices [58]. This slow progress was not only due to the challenge of achieving sufficient reflectivity in the mirrors but also resulted from difficulties in implementing efficient electrical injection. The low conductivity of p-GaN limits lateral current spreading from the intracavity p-contacts to the active region, reducing hole injection efficiency. To overcome this, most device designs incorporate a semi-transparent conductive layer within the cavity to spread current uniformly into the active region.

The most common solution in blue VCSELs is a thin indium tin oxide (ITO) layer, which serves as both the p-contact and a lateral current-spreading layer. ITO is referred to as a transparent conductive oxide indicating a trade-off between transparency and conductivity, but it has a significant absorption tail extending into the blue, with absorption coefficients typically above $1000\,\mathrm{cm}^{-1}$. To limit the absorption in one round-trip, the ITO is kept thin (20–30 nm) and positioned at an antinode of the standing wave, although such thin layers reduce conductivity. It is also important to keep the ITO surface smooth to minimize scattering losses [138]. Electrical isolation outside of the aperture between the ITO and p-GaN is achieved either by etching/ion-implantation [26, 139–141] or by adding an insulating layer such as SiO_2 between the p-GaN and the ITO [142].

In the UV the absorption is even higher and ITO is therefore not suitable for shorter-wavelength UV VCSELs. For UV lasers, TJs have emerged as a promising alternative, offering the potential for both good conductivity and high transparency in III-nitride devices. While TJs are more difficult to implement at shorter wavelengths, where the wider bandgap of AlGaN and the difficulty of achieving efficient p-type doping increase the series resistance, recent advances have demonstrated low-resistance TJs using (In)GaN interlayers and Al contents up to 58% in homojunctions [143–147]. Recently, TJs have also been demonstrated in UVB microcavities [32], highlighting their potential for future electrically injected UVC VCSELs.

4.1.3 State-of-the-art: blue VCSELs

Figure 4.1(a) shows what has been reported in terms of maximum output power of electrically injected continuous-wave VCSELs emitting at blue wavelengths at room temperature over the years. Blue VCSELs started out being tiny, very efficient heat sources (low wall-plug efficiencies, WPE), and remained so for a long time. But recently tremendous progress has been made. Meijo

University has recently demonstrated blue hybrid VCSELs with a whooping 27.6% WPE, maximum output power of 16.2 mW, and a threshold current density of 7.7 kA cm^{-2} [28, 29]. These improvements have been enabled by three key technologies: high quality AlInN/GaN DBRs [148], nano-height apertures for transverse optical and current confinement [140], and in-situ cavity length control [122]. Furthermore, single-mode lasing up to 7 mW was achieved using 3.3 µm apertures and those lasers had threshold currents of 1.4 mA (16 kA cm^{-2}) [140, 149].

Significant progress has also been made for VCSELs employing all-dielectric DBRs. Sony Corporation has demonstrated a 20 µm-thick cavity device with a curved mirror, achieving a WPE of 22.2% and output powers above 8 mW [27]. By optimizing the aperture size and mirror curvature, they also realized single-mode operation, reaching a threshold of 1.2 mA (9.5 kA cm^{-2}) and an output power of 7.1 mW [132]. More recently, they demonstrated devices with a low threshold of 0.64 mA (5.1 kA cm^{-2}) while maintaining a high maximum output power of 7.6 mW [150].

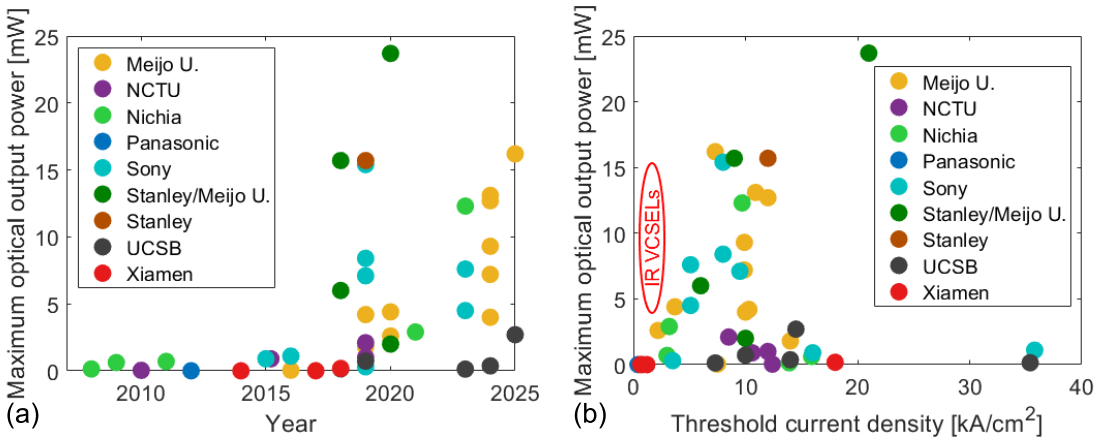

Figure 4.1: (a) Reported maximum optical output power versus publication year and (b) maximum optical output power versus threshold current density for electrically injected continuous-wave blue-emitting VCSELs at room temperature. Data are compiled from [26, 28, 29, 87, 88, 109, 121, 122, 128, 129, 132, 133, 136, 140, 142, 149–167], and the red circle with the text "IR VCSELs" indicate typical values for infrared VCSELs of similar aperture size of 8 µm in diameter.

Figure 4.1(b) shows what has been achieved in terms of maximum output power versus threshold current density. Threshold current density is good to use if one wants to compare lasers with different aperture size, but not always a precise performance metric, as filamentation due to a lack of optical guiding and inhomogeneous current injection is common in III-nitride VCSELs [168], especially in early-stage devices. The data highlight a fundamental design trade-off between output power and lasing threshold: achieving high output power requires a less reflective outcoupling mirror (fewer DBR pairs), which increases optical losses inside the cavity and raises the threshold. Conversely,

minimizing threshold typically involves highly reflective DBRs (more pairs) on both sides, reducing mirror losses but also lowering outcoupling efficiency and output power.

As discussed in Section 2.3.1, well-performing GaN VCSELs are expected to have intrinsically higher threshold current densities due to the larger effective mass and higher density of states. From Fig. 4.1(b), it is clear that recent GaN VCSEL developments are indeed moving toward this regime, with a bit higher thresholds but output powers comparable to GaAs VCSELs. However, given the shorter wavelength of blue emission, each photon from a GaN VCSEL carries more energy; thus, for the same external quantum efficiency, a higher optical output power should be expected (by a factor of $E_{ph}(GaN)/E_{ph}(GaAs) \propto \lambda_{GaAs}/\lambda_{GaN} \sim 2$). The fact that current devices still exhibit output powers similar to GaAs VCSELs highlights the potential for further performance improvements.

4.1.4 State-of-the-art: UV VCSELs

Pushing the emission wavelength from the blue into the UV has proven highly challenging for many of the same reasons that limit blue VCSEL performance: inefficient p-type doping of AlGaN [169], poor lateral current spreading, difficulty achieving high-reflectivity mirrors in the deep-UV [94], and managing optical losses and series resistance. These challenges become even more severe at shorter wavelengths, and to date no CW electrically injected UVC VCSELs have been reported.

The first optically pumped UV VCSELs were demonstrated in 1996 [120]. Despite this early progress, electrically injected VCSELs in the UV have so far not been realized. Notably, since 2019 there have been demonstrations of electrically injected UVB (pulsed) and UVC (CW) EELs [33–37], which have addressed several of the fundamental challenges of electrical injection and poor material quality in AlGaN. However, electrical injection is inherently more difficult in VCSELs than in EELs because the injection and optical propagation occur along the same axis. In EELs, vertical current injection and horizontal light propagation allow contacts to be placed out of the optical path. In VCSELs, by contrast, transverse current spreading must be achieved without obstructing the vertical optical mode, which becomes increasingly difficult at shorter wavelengths.

Figure 4.2 summarizes all reported UV VCSEL demonstrations to date, showing cavity Al-content as a function of lasing wavelength. Although the first optically pumped UVA VCSEL was demonstraterd in 1996, relatively little progress was made in pushing to shorter emission wavelengths until 2020 when the first optically pumped UVB VCSEL was reported by our group [30, 170] and later the first UVC VCSELs by and Xiamen University [31, 171] and our group [98].

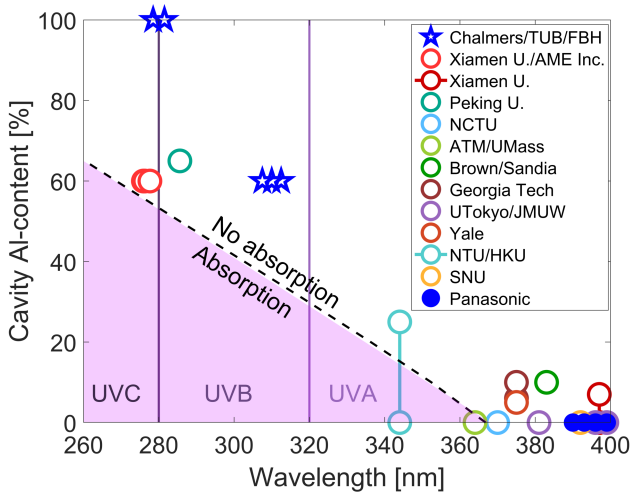

Figure 4.2: Cavity Al-content versus lasing wavelength for all reported UV VCSEL demonstrations. Open circles: optically pumped devices. Filled circles: electrically injected devices. Data are compiled from [30, 31, 98, 129, 170–185]. The dashed line marks the approximate absorption edge of the AlGaN cavity and the vertical lines separates the UVB and UVC regions. The only electrically injected devices reported to date operate in the UVA region.

4.2 Towards electrically injected UVC VCSELs

Electrically driven VCSELs operating in the UVC remain an elusive goal. Despite significant progress in optically pumped UVC VCSELs [31, 98, 171], no device has yet achieved continuous-wave (CW) lasing under electrical injection.

One critical but often overlooked challenge is thermal management. Heat is generated through resistive losses (due to the low electrical conductivity of AlGaN [169]) and non-radiative recombination, while heat dissipation is hindered by the poor thermal conductivity of materials like AlGaN and dielectric DBRs. Elevated temperatures can lead to detuning, increased leakage, and enhanced non-radiative recombination. Together, these effects can trigger thermal roll-over, where further increases in current lead to a decrease in output power. If thermal roll-over occurs before the threshold current is reached, the device will not achieve lasing under CW operation.

4.2.1 The challenge of heat in UVC VCSELs

We show that simply applying the same cavity design principles used in blue VCSELs to UVC devices results in prohibitive temperatures. For instance, a 10λ cavity of $Al_{0.75}Ga_{0.25}N$ with dielectric DBRs is predicted to reach internal temperatures as high as 370 °C, with a thermal resistance of $\sim 4400\,\mathrm{K\,W^{-1}}$ at 80 mW dissipated power, well above the thermal roll-over limit of GaN VCSELs

(∼ 150 °C) [109], see Fig. 4.3(a–b). For more details see Paper B.

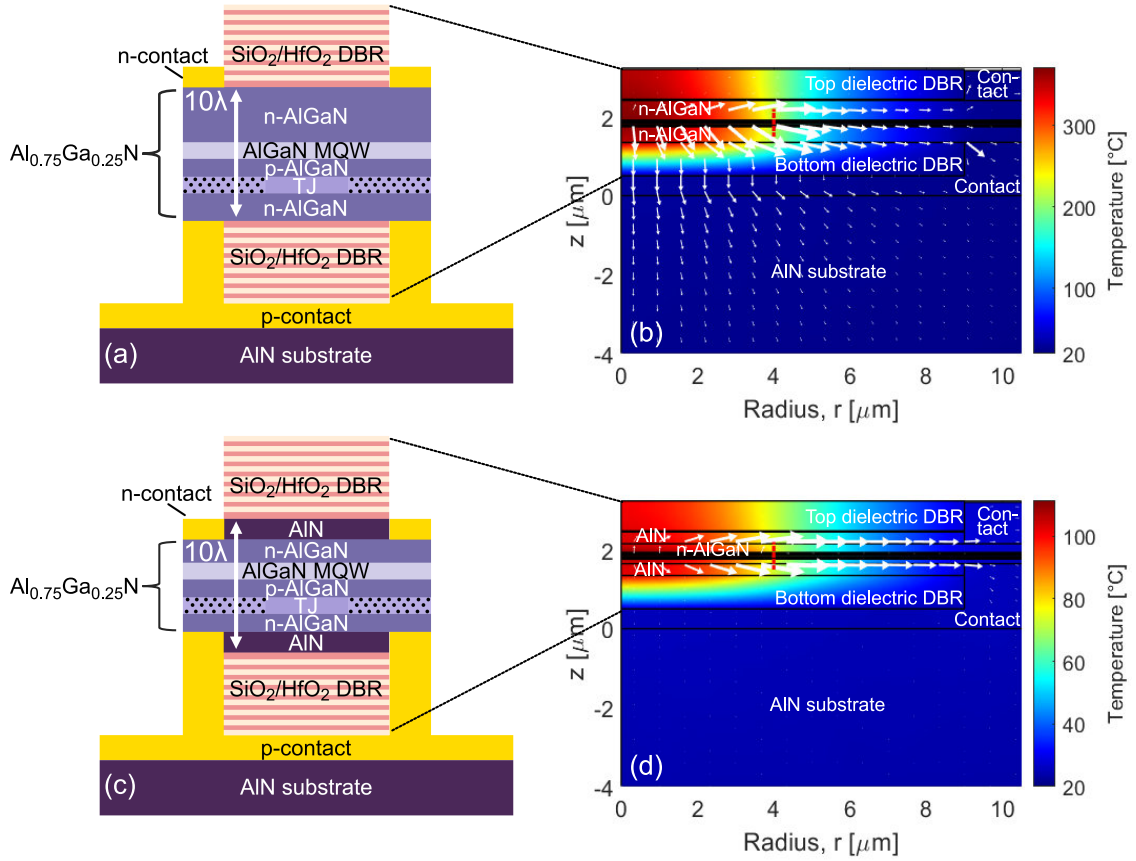

Figure 4.3: Simulated steady-state temperature distribution in a 10λ UVC VCSEL near threshold with a total dissipated power of 80 mW. The white arrows indicate the heat flux. A red dotted line has been inserted at r = 4 µm to indicate the extent of the current aperture. (a-b) Cavity consisting of $Al_{0.75}Ga_{0.25}N$. The poor thermal conductivity of AlGaN leads to an inefficient heat transfer from the active region resulting in a high temperature of 370 °C (R_{th} = 4400 K/W) in the active region. (c-d) Part of the n-AlGaN layer has been replaced by a 300-nm thick AlN-layer on both the n-side (top) and p-side (bottom) of the cavity. The excellent thermal conductivity of the AlN layers facilitates the lateral transport of heat as indicated by the white arrows. In this design a maximum internal temperature of only 110 °C (R_{th} = 1140 K/W) is reached in the active region.

4.2.2 Strategies for reducing thermal resistance

In blue GaN VCSELs, both simulations [186, 187] and experiments [109] have shown that increasing the cavity length significantly reduces the thermal resistance. However, this trend has not been physically explained in the literature. In Paper B, we present the first analytical model that captures the underlying mechanism: when vertical heat conduction is limited, as is the case for devices with low-thermal-conductivity dielectric DBRs, lateral heat spreading becomes

the dominant dissipation pathway. This lateral conduction results in an inverse scaling of thermal resistance with cavity length.

We develop a simple cylindrical heat flow model showing how R_{th} scales inversely with cavity length when lateral conduction dominates, which is the case when using low-conductivity DBRs.

$$R_{th} \approx \frac{1}{2\pi L_c \kappa} \ln\left(\frac{r_0}{r_{ap}}\right) + R_{th,sat}, \tag{4.1}$$

where L_c is the cavity length, κ is the effective thermal conductivity, r_{ap} is the aperture radius, and r_0 the radial distance to the heat sink. The additive term $R_{th,sat}$ accounts for saturation effects in long cavities.

Our simulations confirm that increasing the cavity length significantly lowers R_{th}, up to a point. For GaN VCSELs, thermal resistance decreases as $1/L_c$ up to $\sim 30\lambda$, beyond which it saturates. This saturation arises because the heat source becomes effectively decoupled from the opposite side of the cavity. Once the cavity is sufficiently long, heat no longer spreads far enough vertically to benefit from additional lateral redistribution. The thermal transport then increasingly resembles that of a disk-shaped heat source placed on the surface of a semi-infinite medium. In this limit, the saturated thermal resistance can be approximated analytically by [188]

$$R_{th,sat} = \frac{1}{2\kappa d_{ap}}, \tag{4.2}$$

where d_{ap} is the aperture diameter. This expression provides an excellent match to the simulated thermal resistance in long GaN-based VCSELs, where $R_{th,sat} \approx 390\,\mathrm{K\,W^{-1}}$ at 30λ, as shown in Fig. 4.4. However, in UVC VCSELs with an AlGaN cavity ($\kappa = 15\,\mathrm{W\,m^{-1}\,K}$), the same expression overestimates the saturated thermal resistance by approximately a factor of two. For example, simulations give $R_{th,sat} \approx 2100\,\mathrm{K\,W^{-1}}$, as shown in Fig. 4.4, compared to the analytical prediction of $R_{th,sat} \approx 4200\,\mathrm{K\,W^{-1}}$ using Eq. (4.2). This discrepancy arises because additional heat dissipation paths, such as vertical conduction through the bottom dielectric DBR and lateral conduction toward the heat sink at radius r_0, become non-negligible in comparison with Eq. (4.2). Since these paths are not affected by further extension of the cavity above the active region, they remain constant and act in parallel with the lateral path, effectively reducing the total saturated thermal resistance below the value predicted by Eq. (4.2).

However, even with extended cavity lengths of 30λ, the low thermal conductivity of AlGaN limits the reduction in thermal resistance to $\sim 2600\,\mathrm{K\,W^{-1}}$, which remains too high for practical continuous-wave operation. For an 80 mW dissipated power, this corresponds to an internal temperature of $\sim 230\,^{\circ}\mathrm{C}$, above the roll-over point for typical blue VCSELs of 150 °C [142]. Additionally, growing a thick (30λ) $Al_{0.75}Ga_{0.25}N$ cavity on an AlN template can introduce strain relaxation and lead to defect formation. For such long cavities, the use of curved DBRs may also be required to minimize diffraction losses.

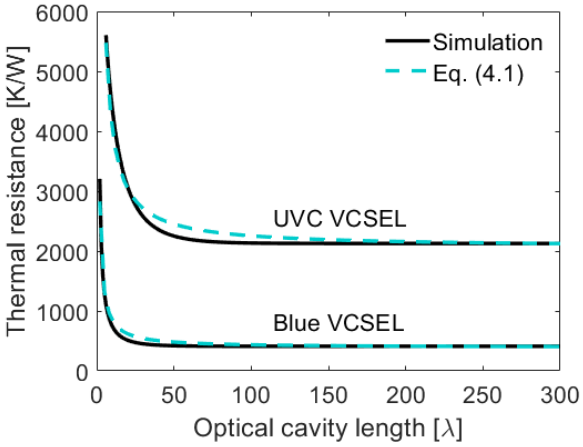

Figure 4.4: Simulated thermal resistance as a function of optical cavity length for blue and UVC VCSELs. For both devices, thermal resistance decreases significantly with cavity length before saturating beyond $\sim 30\lambda$. The dashed curves show analytical fits based on the cylindrical heat flow model of Eq. (4.1), which assumes dominant lateral conduction.

An alternative strategy for reducing thermal resistance is suggested by Eq. (4.1): decreasing the effective heat spreading distance r_0, which is closely related to the p-contact diameter (which act as a heat sink). Reducing the p-contact diameter brings it closer to the heat source, improving thermal extraction. In Paper B, we show that a 15% reduction in R_{th}, can be achieved this way, significant, though still insufficient to reach lasing-viable temperatures.

4.2.3 Will AlGaN VCSELs die of heat - or can we save them?

As discussed in the previous section, conventional design strategies struggle to reduce the thermal resistance of AlGaN-based UVC VCSELs sufficiently for CW lasing. Even with extended cavities and a p-contact located closer to the active region, the internal temperature remains well above typical rollover temperatures under realistic operating conditions. This is due to the low thermal conductivity of AlGaN, which fundamentally limits heat dissipation through the cavity. To overcome this thermal bottleneck, we propose embedding high-thermal-conductivity AlN spacer layers on both sides of the cavity to enhance lateral heat spreading.

We believe that this structure possible to realize since AlN can be grown lattice-matched to $Al_{0.75}Ga_{0.25}N$ on AlN substrates [189]. Although AlN is electrically insulating, the structure can remain compatible with current injection by selectively etching the AlN to access the n- and p-contact regions. This allows electrical access to the underlying AlGaN while retaining the AlN's role in lateral heat spreading.

Using this approach, we simulate a structure with 300 nm thick AlN layers above and below a 10λ cavity, with the AlGaN thickness adjusted to preserve the total optical length (10λ). The resulting thermal resistance is reduced from $4400\,\mathrm{K\,W^{-1}}$ to $1140\,\mathrm{K\,W^{-1}}$, resulting in an internal temperature of only 110 °C under 80 mW CW operation, as illustrated in Fig. 4.3(c-d), well below the rollover point of 150 °C. These results demonstrate that, with appropriate thermal design, CW lasing in AlGaN VCSELs is feasible from a thermal point of view.

4.3 Athermalization of the lasing wavelength

Precise wavelength control is essential in many VCSEL applications such as gas sensing [110], atomic clocks [111], spectroscopy [112], and fiber-optic communication systems [113, 114], where the operating wavelength must remain stable despite temperature fluctuations. In III-nitride VCSELs, the lasing wavelength typically redshifts with increasing temperature at a rate of $12\,\mathrm{pm\,K^{-1}}$ to $18.5\,\mathrm{pm\,K^{-1}}$ [76, 109, 187, 190, 191], due to the positive thermo-optic coefficient $\partial n/\partial T > 0$ of the (Al)GaN-based cavity.

We have experimentally demonstrated that the redshift caused by the semiconductor cavity can be counteracted by properly designed DBRs, enabling a VCSEL with a temperature-stable lasing wavelength. In Paper A, we developed an analytical framework for understanding this compensation mechanism by formulating the cavity resonance condition in terms of the phase penetration depth into the DBRs. This approach captures how temperature-induced changes in the mirror phase, arising from the thermo-optic properties of the dielectric materials, can counteract the thermal redshift of the cavity mode. We also experimentally demonstrated a 2.5λ UVB VCSEL exhibiting significantly reduced thermal wavelength shift based on this design.

Here, we extend the discussion by showing that the same compensation can be understood more directly in terms of the mirror phase shifts themselves. This equivalent but arguably more intuitive perspective offers additional physical insight into how cavity and mirror dispersion interact to achieve athermal behavior.

4.3.1 DBR phase shift compensation

The resonance condition in a VCSEL is obtained by adding all phase accumulation over one round-trip in the cavity. For constructive interference to occur, and for the formation of standing waves, the phase must repeat itself every round-trip. This required that the accumulated phase be an integer number of 2π.

$$2k_0 n_c L_c + \varphi_t + \varphi_b = 2\pi m, \tag{4.3}$$

where $\varphi_{b/t}$ is the phase obtained from reflection in the top/bottom DBR. Solving for the resonance wavelength one obtains

$$\lambda_m(RT) = \frac{2n_cL_c}{m-(\varphi_t+\varphi_b)/(2\pi)} \approx \frac{2n_cL_c}{m}, \tag{4.4}$$

where we have assumed that at room temperature (RT), the Bragg wavelength of the DBRs are designed to coincide with the cavity resonance yielding $\varphi_{t/b} = 0$. At elevated temperatures, the refractive index of both the cavity and the DBR layers change, affecting the resonance wavelength. At an elevated temperature, the resonance wavelength can be expressed as

$$\lambda_m(RT+\Delta T) = \frac{2(n_c+\partial n_c/\partial T\ \Delta T)L_c}{m-(\varphi_t+\varphi_b)/(2\pi)}, \tag{4.5}$$

where $\mathrm{d}n_c/\mathrm{d}T$ is the average thermo-optic coefficient of the cavity, and $\varphi_{t/b}$ is the phase shift acquired from the top/bottom DBRs. It is possible to express the resonance wavelength at the elevated temperature based on the room temeprature resonance using Eq. (4.4)

$$\lambda_m(RT+\Delta T) = \frac{m\lambda_m(RT)+2L_c\ \partial n_c/\partial T\ \Delta T}{m-\varphi/\pi}. \tag{4.6}$$

In the 2.5λ ($m = 5$) UVB VCSELs of Paper A, the cavity consists mainly of $Al_{0.6}Ga_{0.4}N$, which has $\partial n_c/\partial T = 5.9\times10^{-5}\,\mathrm{K}^{-1}$. From Fig. 4.5(a) we can also see that over a temperature range of $\Delta T = 50\,^{\circ}\mathrm{C}$, the phase of the mirror reflectance changes marginally. This phase change is $\varphi(RT+\Delta T)-\varphi(RT) = -0.005\pi$. Although this is a seemingly small phase change, it is enough to counteract the expansion of the optical cavity length caused by the AlGaN cavity, resulting in $\lambda_T = 310.07\,\mathrm{nm}$, almost identical to the design wavelength of $\lambda_{RT} = 310.00\,\mathrm{nm}$. Without this phase change, the cavity resonance would be $\lambda_T = 310.38\,\mathrm{nm}$. This brings us to another point. The exact layer thickness of the DBRs is very important to get the Bragg wavelength of the DBRs at the same wavelength as that of the cavity. Just a small shift can result in some nm's of shift in the resonance wavelength, as shown in Section 3.2.2.

4.3.2 The hard-mirror equivalent cavity model

To better understand how mirror phase affects the cavity resonance condition, we adopt the concept of a hard-mirror equivalent cavity, as illustrated in Fig. 4.5(b-c). In this model, the distributed Bragg reflectors (DBRs) are replaced by idealized mirrors with zero phase shift, and the phase normally imparted by the DBRs is accounted for by extending the cavity length. This allows us to express the resonance condition in a form that directly incorporates the impact of DBR phase dispersion.

Within the DBR stopband, the reflection phase varies approximately linearly with wavelength. This linear dependence enables us to reformulate the

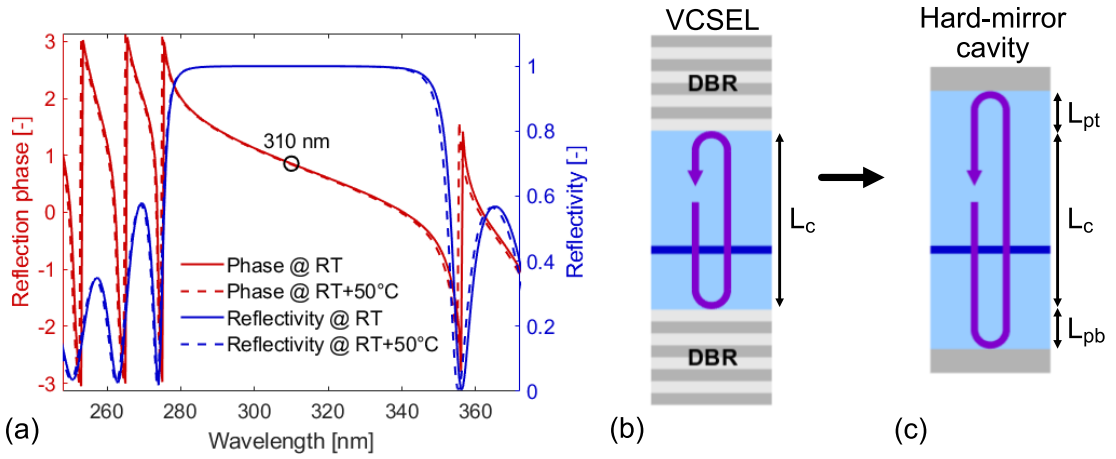

Figure 4.5: (a) Calculated reflection phase (red) and reflectivity (blue) of a 10-pair HfO_2/SiO_2 DBR designed for a Bragg wavelength of 310 nm. Solid lines correspond to room temperature (RT), while dashed lines show results at an elevated temperature of $RT + 50\,°C$. A 10 nm HfO_2 spacer layer, present in the full VCSEL design, is included in the calculation. Due to this spacer, the reflection phase at the Bragg wavelength is non-zero, in contrast to a typical ideal DBR response. (b) Schematic of a VCSEL cavity, and (c) the corresponding hard-mirror equivalent cavity. In this equivalent model, the mirrors are treated as ideal reflectors with zero reflection phase.

resonance condition in terms of the phase penetration depth into the mirrors. From Eq. (4.3), we write

$$2k_0 n_c L_c + 2(k_0 - k_t)\bar{n}_c L_{p,t} + 2(k_0 - k_b)\bar{n}_c L_{p,b} = 2\pi m, \tag{4.7}$$

where $\varphi_{t/b} = 2(k_0 - k_{t/b})\bar{n}_c L_{p,t/b}$ is the phase shift incurred by the mirrors, $k_{t/b} = 2\pi/\lambda_{t/b}$ is the Bragg wavevector of the top and bottom DBR, and $L_{p,t/b}$ is the phase penetration depth into the top and bottom DBRs. Although the penetration depth can be derived from transfer matrix theory [192,193], a more physically intuitive form relates it to the linear slope of the phase within the stopband as $L_{p,t/b} = (\lambda_m^2/(4\pi\bar{n}_c))(-\partial\varphi_{t/b}/\partial\lambda)$. Using Eq. (4.7), we obtain an explicit formula for the resonance wavelength that includes the DBR phase contribution

$$\lambda_m = \frac{2\bar{n}_c L_{eff}}{m + 2\bar{n}_c(L_{p,t}/\lambda_t + L_{p,b}/\lambda_b)}, \tag{4.8}$$

where $L_{eff} = L_c + L_{p,t} + L_{p,b}$ is the effective cavity length in the hard-mirror equivalent cavity model. When the cavity resonance is aligned with the Bragg wavelengths ($\lambda_m = \lambda_t = \lambda_b$), this reduces to the standard Fabry–Pérot resonance condition $\lambda_m = 2\bar{n}_c L_c/m$. This formulation also makes it straightforward to analyze how the mirror phase, and its wavelength dependence, influences the temperature sensitivity of the lasing mode. By differentiating Eq. (4.8) with respect to temperature, we obtain

$$\frac{\mathrm{d}\lambda}{\mathrm{d}T} = \frac{\mathrm{d}\lambda_{FP}/\mathrm{d}T + (2L_{p0}/L_c)\,\mathrm{d}\lambda_{DBR}/\mathrm{d}T}{1 + 2L_{p0}/L_c}, \tag{4.9}$$

where we assume identical DBRs with penetration depth L_{p0}, $\mathrm{d}\lambda_{FP}/\mathrm{d}T = (\lambda_0/n_{c0})/(\,\mathrm{d}n_c/\mathrm{d}T\,)$ is the Fabry–Pérot resonance shift due to cavity material alone, and $\mathrm{d}\lambda_{DBR}/\mathrm{d}T \approx 2(d_L\ \mathrm{d}n_L/\mathrm{d}T + d_H\ \mathrm{d}n_H/\mathrm{d}T\,)$ is the Bragg wavelength shift of the DBRs with temperature.

4.3.3 Engineering an athermal cavity resonance

Equation (4.9) shows that the overall thermal tuning rate arises from two contributions: the intrinsic redshift of the cavity mode due to the positive thermo-optic coefficient of the semiconductor, and the mirror phase shift arising from dielectric materials, which can have a negative thermo-optic coefficient. Taken together, these effects can either reduce, neutralize, or even reverse the redshift, depending on the sign and magnitude of $\mathrm{d}\lambda_{DBR}/\mathrm{d}T$.

This leads to two practical strategies for achieving athermal behavior. In short-cavity designs with dispersive mirrors, the relative contribution of the DBR phase is significant. Using dielectric DBRs with negative $\mathrm{d}n/\mathrm{d}T$, such as TiO_2 [113, 194, 195] or HfO_2 [73], the redshift from the cavity can be partially or fully compensated by a blueshift from the mirrors. For longer cavities, where the DBR phase contribution is reduced due to a larger L_c, athermalization can instead be achieved by embedding dielectric spacer layers (e.g., HfO_2) directly inside the cavity. These layers, chosen for their negative $\mathrm{d}n/\mathrm{d}T$, can offset the positive Fabry–Pérot shift of the semiconductor cavity.

This concept is explored in detail in Paper A [73], where both athermalization strategies are analyzed through simulations. In particular, the short-cavity approach using dielectric DBRs with negative thermo-optic coefficients is also experimentally validated for a 2.5λ UVB VCSEL, as shown in Fig. 4.6. This design yields the most inherently temperature-stable emission wavelength reported from a VCSEL to date. The device exhibits a total wavelength shift of less than 0.1 nm over an 80 °C temperature range. Throughout this range, the thermal tuning rate remains small and negative, with the largest magnitude occurring near room temperature at $-3.4\,\mathrm{pm\,K^{-1}}$, to be compared with the typical wavelength shift of $\approx 15\,\mathrm{pm\,K^{-1}}$ for III-nitride VCSELs [76, 109, 187, 190, 191].

4.4 Single-mode and polarization stable blue VCSELs

Achieving single-mode and polarization-stable emission in blue VCSELs remains a significant challenge. Unlike their infrared (GaAs-based) counterparts, only a handful of viable design strategies have been demonstrated to date. For III-nitride VCSELs, single-mode operation is important in applications such as underwater optical wireless communication, smart glasses, adaptive laser headlights, high-resolution projectors, sensing using tunable diode lasing spectroscopy (TDLS) and atomic clocks.

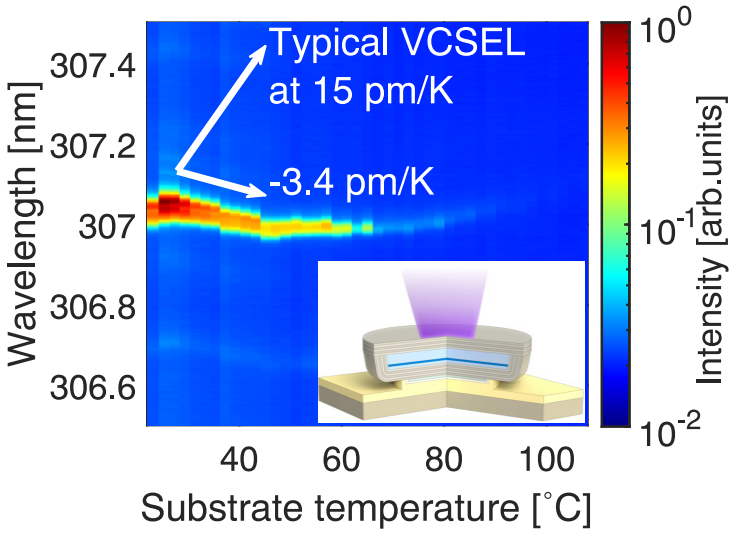

Figure 4.6: Emission spectrum of the 2.5λ UVB VCSEL for different substrate temperatures. The arrows indicate the wavelength shift with temperature of this device ($-3.4\,\mathrm{pm\,K^{-1}}$ near room temperature) compared with the $15\,\mathrm{pm\,K^{-1}}$ of typical III-nitride VCSELs [76, 109, 187, 190, 191].

In GaN-based VCSELs, two main approaches have been explored to achieve single-mode operation. One is to reduce the aperture diameter [140,149], which limits the lateral extent of the optical cavity so that only the fundamental transverse mode can be supported. Higher-order modes are cut off due to their broader spatial variation and inability to satisfy the resonance condition in such a confined cavity. The mechanism is analogous to optical waveguides, where only the fundamental mode can propagate if the waveguide core is sufficiently small relative to the wavelength and index contrast. In VCSELs, the effective index contrast results from vertical cavity length differences between the center and periphery, creating lateral confinement. When the aperture and index step are small enough, only the fundamental mode remains below threshold. However, this approach increases device resistance due to the narrow current path and makes the structure more sensitive to thermal lensing, which can shift the guiding conditions and allow higher-order modes to appear. The small aperture also limits the achievable output power. In addition, such devices lack intrinsic polarization control when grown on the c-plane [196]; while a fixed polarization state may be observed at low drive currents due to residual strain or birefringence, the polarization is often unstable and can switch unpredictably with current or temperature. Growth on non-c-plane substrates can introduce intentional birefringence, causing the two orthogonal polarizations to experience different optical cavity lengths and losses, thereby favoring single polarization [134]. In addition, polarization stability has also been reported for m-plane VCSELs, where it has been attributed to anisotropy in the gain between different polarization states rather than cavity effects [197,198]. How-

ever, c-plane substrates remain the industry standard due to their availability, lower cost, and established growth processes.

An alternative method is to use a long cavity with a curved bottom mirror, which introduces a spatially varying phase shift upon reflection. The fundamental mode has a Gaussian wavefront whose curvature naturally matches that of the mirror, enabling constructive interference after each round trip. In contrast, higher-order modes, with broader and less well-matched wavefronts, accumulate excess phase shift and suffer higher round-trip loss. This intrinsic mode filtering enables single-mode operation even for relatively large apertures. However, fabricating monolithic curved mirrors in GaN is technically demanding. While the use of long cavities improves thermal management by lowering thermal resistance, reducing device temperature, and mitigating thermal lensing, it can also lead to mode hopping between adjacent longitudinal cavity modes. More recent designs address this by introducing a $\lambda/2$-thick Fabry–Pérot spacer in the top DBR to stabilize the longitudinal mode (filtering cavity), but the advantage with broadband dielectric DBR is then lost [137]. As with small-aperture designs, polarization instability remains a challenge, since the cavity does not inherently favor one polarization over the other.

To address these limitations, we propose an alternative approach based on shallow surface reliefs and sub-wavelength gratings, integrated into the top DBR of the VCSEL structure as shown in Fig. 4.7. While such techniques have been explored in other wavelength regimes [199–203], they have not yet been applied to blue-emitting VCSELs. The surface relief laterally modifies the mirror reflectivity, promoting single-mode operation by introducing higher loss for modes with greater lateral extent, see Fig. 4.7(a-b). Meanwhile, a sub-wavelength grating can enable polarization control by creating a birefringent response, and thereby a polarization-dependent mirror reflectivity, favoring one linear polarization over the other, see Fig. 4.7(c-d). In the following subsections, we present simulation results using the 2D effective-index method [103, 104, 204] illustrating the potential of these concepts for achieving single-mode and polarization-stable emission in blue VCSELs. It should be noted that this simulation method does not account for diffraction losses. As a result, the calculated modal discrimination is likely an underestimation of what can be expected in a real device.

4.4.1 Surface relief

A surface relief can be used to suppress higher-order lateral modes in blue GaN-based VCSELs by introducing spatially selective mirror losses in the top DBR. This is achieved by etching a circular region into the DBR with a diameter smaller than the aperture, as shown in Fig. 4.7(b). Since higher-order modes such as LP02 and LP11 extend further out laterally compared to the fundamental LP01 mode, they overlap more strongly with the etched peripheral region, where the reflectivity is reduced. As a result, they experience significantly higher modal loss than the fundamental mode. This effect is clearly illustrated

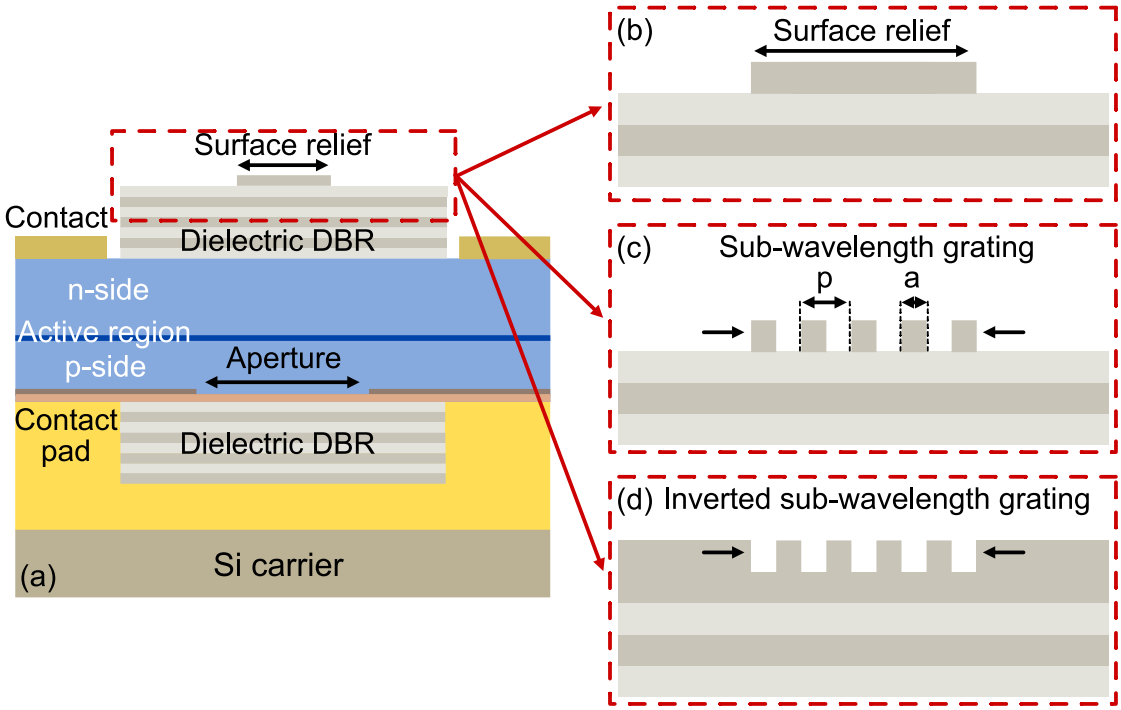

Figure 4.7: a) Schematic of a blue GaN VCSEL with all-dielectric DBRs and a central surface-relief grating. (b) Zoom-in showing a conventional surface relief, where the peripheral part of the final DBR layer has been etched away, leaving a central raised circular region with high reflectivity and (c) a sub-wavelength grating for polarization control. The grating has period p and groove width a, resulting in a duty cycle of a/p. (d) Zoom-in showing an inverted surface relief, where the final DBR layer is extended to $\lambda/2$ thickness and a circular grating is etched into the center to locally restore high reflectivity.

in Fig. 4.8(a), which shows that a surface-relief diameter slightly larger than half the aperture diameter (i.e., 3.5 µm for a 6 µm aperture) introduces a large radial loss for higher-order modes.

The strength of the mirror loss introduced by the relief depends on the number of DBR pairs in the outcoupling mirror and the etch depth. For highly reflective DBRs (e.g., 10 pairs), a shallow etch of $\lambda/4$ results in only a marginal change in reflectivity as shown in Fig. 4.8(b). In contrast, when using fewer pairs (e.g., 8 or 9), etching just one $\lambda/4$ into the DBR can introduce substantial mirror loss and modal discrimination as shown in Fig. 4.8(c-d). This behavior arises from destructive interference: the top Nb_2O_5 DBR layer is removed and replaced by a SiO_2-air interface, which has a lower refractive index contrast and introduces a π phase shift compared to the unetched Nb_2O_5-air interface ($n_{Nb2O5} > n_{SiO2} > n_{air} = 1$). As the DBR is a periodic structure, this leads to periodic maxima in mirror loss with etch depths equal to odd multiples of $\lambda/4$.

However, there is a trade-off. While a lower number of DBR pairs enhances

higher-order mode suppression, it also increases the threshold gain of the fundamental mode, due to higher mirror loss in the center of the cavity as well. This is visible in Fig. 4.8(b–d), where the material threshold gain of the fundamental LP01 mode increases with decreasing DBR pair count for all modes.

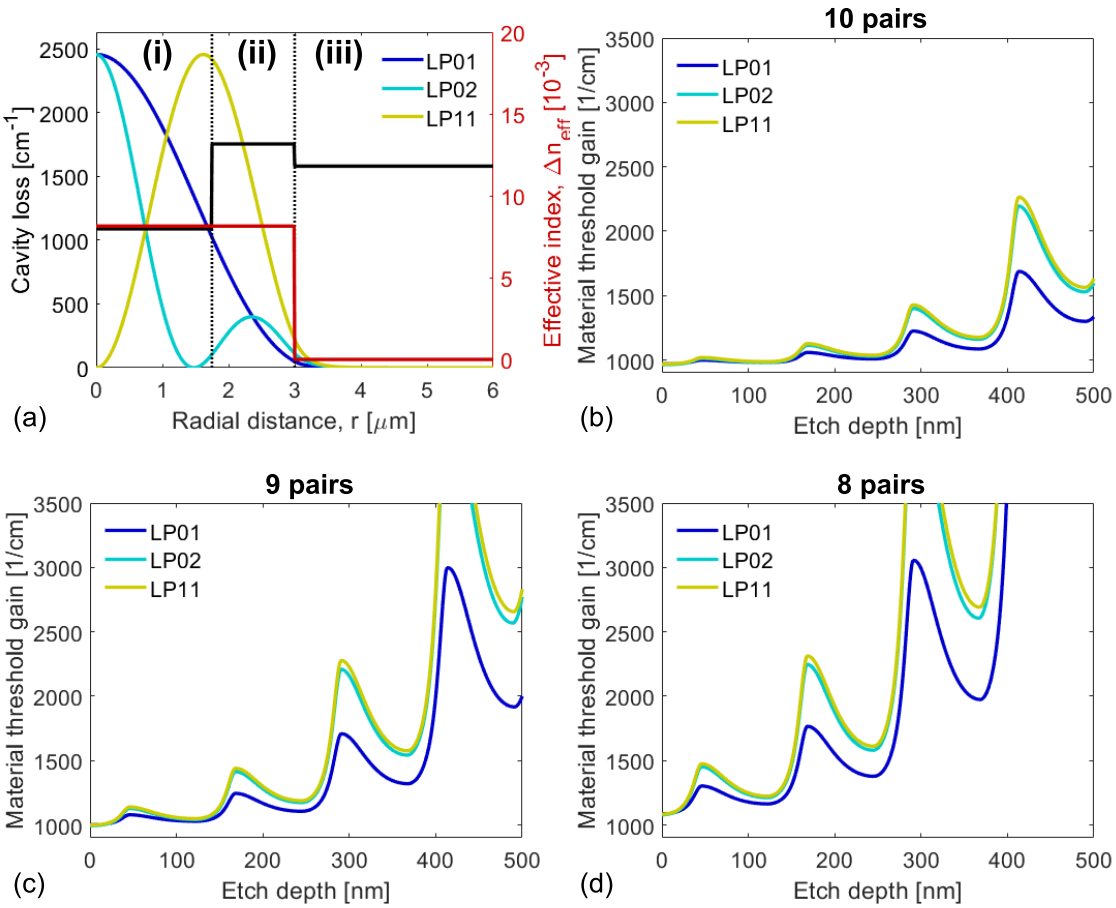

Figure 4.8: Blue GaN VCSEL with a surface relief diameter of 3.5 µm, and aperture diameter of 6 µm. (a) Fundamental mode (LP01), and the first two higher-order modes (LP02, and LP11). The black line shows the radially varying cavity losses caused by the surface relief. Region (i) is un-etched within the aperture, region (ii) is etched with surface relief and inside the aperture, and region (iii) is outside the aperture, also with etched mirror. (b-d) Threshold material gain for the three lowest order modes versus relief depth for different number of Nb_2O_5/SiO_2 pairs for the outcoupling DBR of (b) 10 pairs, (c) 9 pairs, and (d) 8 pairs.

Figure 4.9(a) summarizes the dependence of modal discrimination on the surface-relief diameter for different DBR configurations. Modal discrimination is defined here as the difference in material threshold gain between the fundamental mode (LP01) and the next supported higher-order mode (LP02 or LP11), and serves as a metric for how effectively higher-order modes are suppressed. The optimal relief diameter is around 3.5 µm, yielding the highest

difference in threshold between LP01 and the next supported mode. Notably, modal discrimination is low when using a 10-pair DBR, consistent with the limited reflectivity change achieved by shallow etching. As shown in Fig. 4.9(b), however, this can be compensated by increasing the etch depth into the DBR stack. For example, etching $3\lambda/4$ or $5\lambda/4$ into the DBR with 9 or 10 pairs can recover similar levels of modal discrimination and threshold gain as the $\lambda/4$-etched 8-pair case. This highlights the importance of tailoring both DBR design and etch depth to balance fundamental mode performance and higher-order mode suppression.

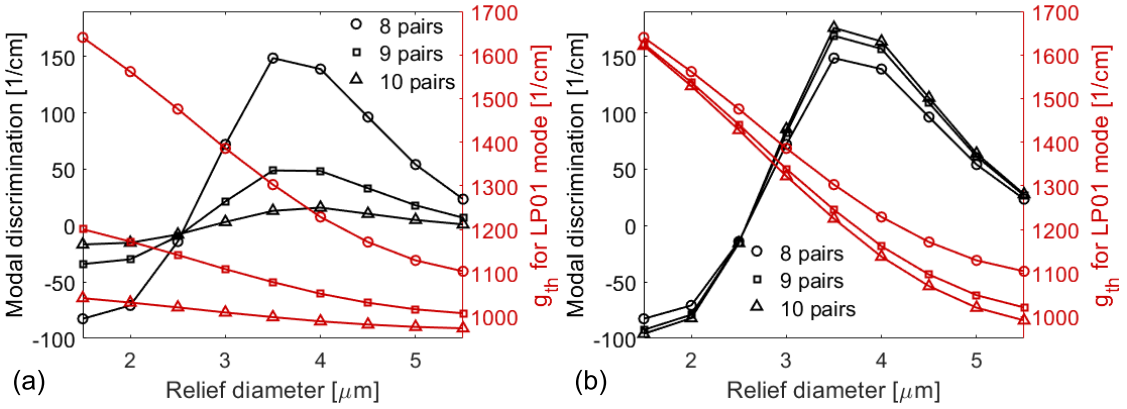

Figure 4.9: Blue GaN VCSEL with varying surface relief of diameter for an aperture diameter 6 µm. (a) Defining the surface relief by etching $\lambda/4$ deep into the outcoupling DBR (etching away the top Nb_2O_5 layer), for three different cases: when the outcoupling DBR has 8 (circles), 9 (squares), and 10 pairs (triangles). (b) Defining the surface relief by etching $\lambda/4$ deep into the outcoupling DBR with 8 pairs (circles), $3\lambda/4$ into the outcoupling DBR with 9 pairs (squares), and $5\lambda/4$ into the outcoupling DBR with 10 pairs (triangles). These cases yield approximately the same modal discrimination and same threshold material gain for the fundamental mode.

4.4.2 Sub-wavelength grating

A sub-wavelength grating can be introduced into the surface-relief structure to control the polarization properties of the emitted light. By etching narrow periodic grooves into the final DBR layer, with a period p much smaller than the wavelength of light, the grating behaves as an anisotropic medium. The electric field components polarized parallel ($E_{\parallel}$) and perpendicular ($E_{\perp}$) to the grooves experience different effective permittivities due to the alternating dielectric and air regions. This leads to polarization-dependent reflectivity, enabling selective suppression of one polarization over the other.

The duty cycle of the sub-wavelength grating is defined as $d = a/p$, where a is the width of the groove and p is the grating period. A duty cycle of $d = 0$ corresponds to an unpatterned air layer, while $d = 1$ corresponds to a uniform

dielectric layer. The effective permittivity for electric fields polarized parallel to the grooves is given by [201]

$$\epsilon_{eff,\parallel} = 1 + d(\epsilon - 1), \tag{4.10}$$

while the effective permittivity for the perpendicular polarization is

$$\epsilon_{eff,\perp} = \frac{\epsilon}{d + \epsilon(1 - d)}, \tag{4.11}$$

where ϵ is the permittivity of the dielectric material (an oxide in this case). As shown in Fig. 4.10 and Table 4.1, this results in two distinct effective refractive indices for each polarization, which in turn modifies the reflectivity of the top DBR in a polarization-selective manner.

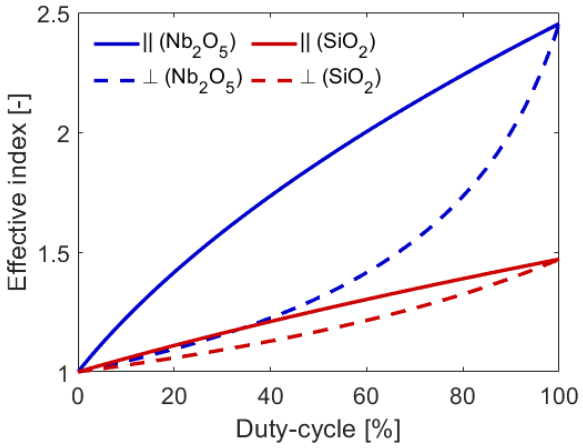

Figure 4.10: Effective refractive index of Nb_2O_5 and SiO_2 in a sub-wavelength grating structure for light polarized parallel ($E_\parallel$) and perpendicular ($E_\perp$) to the grating grooves. At 0% duty cycle the material is a homogeneous air layer, and for a 100% duty cycle the material is homogenous with refractive index given by the dielectric.

Table 4.1: Effective refractive index of Nb_2O_5 and SiO_2 in a sub-wavelength grating structure for light polarized parallel ($E_\parallel$) and perpendicular ($E_\perp$) to the grating grooves for different duty cycles.

Duty cycle	0%	55%	70%	100%
Nb_2O_5 ($\parallel$)	1	1.94	2.12	2.45
Nb_2O_5 ($\perp$)	1	1.36	1.55	2.45
SiO_2 ($\parallel$)	1	1.28	1.35	1.47
SiO_2 ($\perp$)	1	1.19	1.27	1.47

Figure 4.8 shows simulation results for two different surface-relief configurations with sub-wavelength gratings: a conventional design with a central

raised surface-relief region, see Fig. 4.11(a,c), and an inverted design where a central groove is etched into a $\lambda/2$-thick dielectric layer to restore reflectivity, see Fig. 4.11(b,d).

In the conventional design, shown in Fig. 4.7(c), the grating is etched into a protruding central region with high reflectivity. Figure 4.11(a) shows that the modal discrimination peaks around a duty cycle of 70%, where the difference in threshold gain between the two polarizations and any higher-order mode is maximized. Figure 4.11(c) shows the threshold gain as a function of grating etch depth for a fixed duty cycle of 70%.

In contrast, the inverted design, shown in Fig. 4.7(d), uses a $\lambda/2$-thick final DBR layer and etches the grating into the center to restore reflectivity. This configuration is less sensitive to the etch depth, as shown in Fig. 4.11(d). For this design, maximum modal discrimination occurs around 55% duty cycle Fig. 4.11(b), and the polarization perpendicular to the grooves exhibits lower threshold gain at a grating depth of $\lambda/4$.

Physical interpretation of polarization selectivity

The reason why the conventional grating design favors $E_{\parallel}$ polarization is because $\epsilon_{||} > \epsilon_{\perp}$. Before etching, the last Nb_2O_5 mirror layer is $\lambda/4$ thick, so reflections from this layer are in phase with the rest of the DBR, leading to constructive interference and low mirror losses. Etching a grating into the top DBR introduces anisotropy; both $\epsilon_{||}$ and $\epsilon_{\perp}$ are reduced, see Table 4.1, decreasing both the optical thickness and the strength of the mirror reflection. Since $\epsilon_{||} > \epsilon_{\perp}$, the optical thickness seen by $E_{\perp}$ deviates more from the ideal 2π round-trip phase, leading to higher mirror loss for light with perpendicular polarization, as shown in Fig. 4.12(a,c,e). A secondary reflection, ϕ_2, between the remaining unetched top Nb_2O_5 layer and the etched Nb_2O_5 grating region, becomes increasingly out-of-phase with deeper etching for etch depths down to $\lambda/4$. This increases mirror losses for both polarizations and reaches a maximum when the etch depth equals $\lambda/4$ as shown in Fig. 4.11(d).

Deeper etching into the SiO_2 layer introduces additional reflections (ϕ_3, ϕ_4), with ϕ_3 initially in-phase and then moving slightly out of phase with depth. Since $n_{||} \approx n_{\perp}$ in the SiO_2 grating, ϕ_3 is similar for both polarizations. However, the reflection magnitude matters: $|r| = |(n_1 - n_2)/(n_1 + n_2)|$ is larger for $E_{\parallel}$, where $n_{Nb2O5,\parallel} - n_{SiO2,\parallel} = 0.77$, compared to $E_{\perp}$ where $n_{Nb2O5,\perp} - n_{SiO2,\perp} = 0.28$. Thus, $E_{\parallel}$ experiences stronger constructive interference and lower mirror loss, with little change in modal discrimination (since $\phi_{3,\parallel} \approx \phi_{3,\perp}$), consistent with Fig. 4.11(c).

In the inverted grating, the situation is reversed. The unetched DBR layer is $\lambda/2$ thick, and already exhibits destructive interference for both polarizations. Etching the grating restores constructive interference first for perpendicular light due to its lower optical thickness and higher index contrast, as seen in Fig. 4.12(b,d,f). The secondary reflection ϕ_2 reaches constructive interference after $\lambda/4$, resulting in a local minimum in mirror losses, as shown

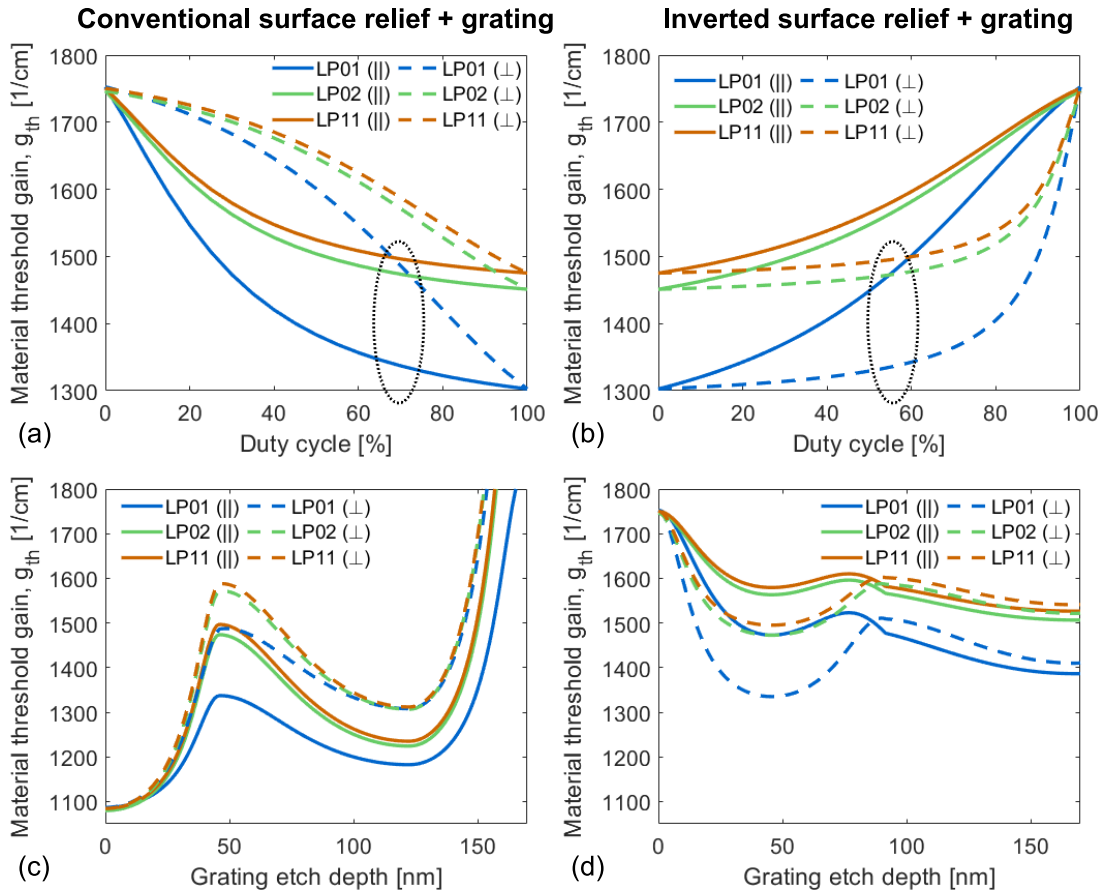

Figure 4.11: Simulated material threshold gain for different transverse modes in blue VCSELs with two types of surface-relief designs with a sub-wavelength grating: (a, c) conventional surface relief with a central protrusion, and (b, d) inverted surface relief, where the final DBR layer is $\lambda/2$ thick and a $\lambda/4$-deep etch is used to restore high reflectivity in the center. The top row (a, b) shows the dependence of material threshold gain on the grating duty cycle for a fixed etch depth of $\lambda/4$. For the conventional design (a), optimal modal discrimination is observed around 70% duty cycle, while the inverted design (b) yields maximum discrimination near 55%. The bottom row (c, d) shows the threshold gain as a function of etch depth, with (c) using a fixed duty cycle of 70% for the conventional design and (d) using 55% for the inverted design. Solid and dashed lines represent the two orthogonal polarization directions. Simulations are based on a blue GaN VCSEL with a 3.5 µm surface-relief diameter, 6 µm aperture diameter, and an 8-pair Nb_2O_5/SiO_2 outcoupling DBR.

in Fig. 4.11(d), opposite to the conventional case. Etching through the top Nb_2O_5 layer introduces additional mirror reflections ϕ_3 and ϕ_4. As before, ϕ_3 starts out in-phase and changes slowly/little when etching deeper into the SiO_2 layer since $n_{SiO2,||} \approx n_{SiO2,\perp} \approx n_{SiO2}$ in the SiO_2 grating. However, reflectivity again matters: for 55% duty cycle, the index contrast for $E_{||}$ is $n_{Nb2O5,||} - n_{SiO2,||} = 0.66$, while for $E_{\perp}$ it is only $n_{Nb2O5,\perp} - n_{SiO2,\perp} = 0.17$. This makes constructive interference more effective for $E_{||}$, leading to a lower

mirror loss for $E_{\parallel}$ compared to $E_{\perp}$ when etching through the Nb_2O_5 layer and into the SiO_2 layer, and a reversal in the lowest loss mode $E_{\perp}$ to $E_{\parallel}$ as shown in Fig. 4.11(d).

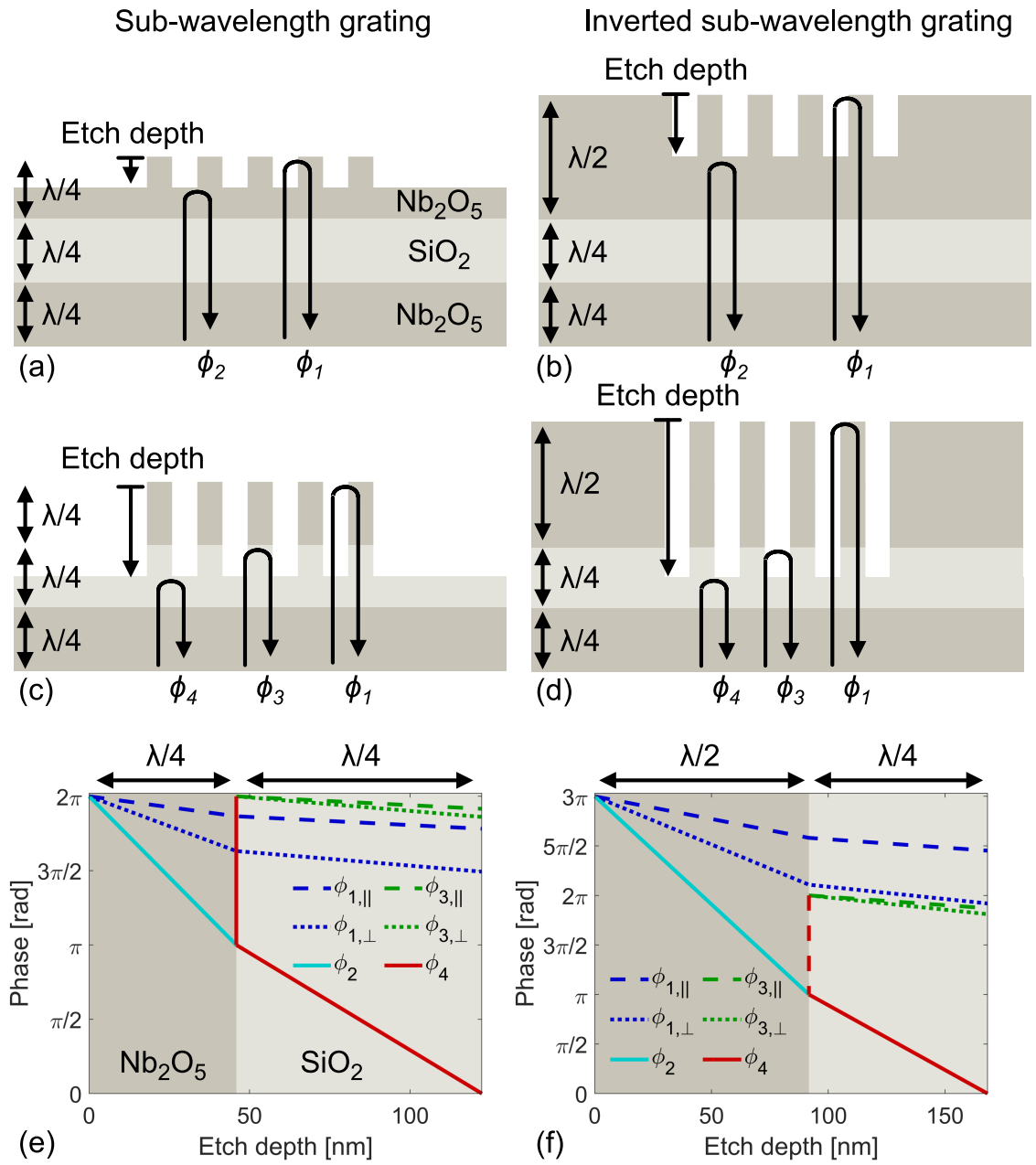

Figure 4.12: Schematic and phase analysis for VCSELs with sub-wavelength grating structures. (a), (c), and (e) show the conventional surface-relief + grating design, while (b), (d), and (f) show the inverted surface-relief + grating design. (a)–(b) illustrate shallow etching into the top Nb_2O_5 layer, while (c)–(d) show deeper etching through Nb_2O_5 and into the SiO_2 layer. (e)–(f) plot the phase ϕ_i of reflections from the central etched region as a function of etch depth. When ϕ is near an integer multiple of 2π, reflections are in-phase and losses are low; when ϕ is near an odd multiple of π, reflections interfere destructively, increasing mirror loss. Solid lines represent unetched dielectric layers; dashed and dotted lines correspond to light polarized parallel ($||$) and perpendicular ($\perp$) to the grating grooves.

Chapter 5

Photonic-crystal surface-emitting lasers

High power or high beam quality — for most semiconductor lasers, you can have one or the other. EELs can deliver watts of output but with a highly divergent beam, while VCSELs produce clean, narrow beams but at much lower powers. What if a single device could give you both? A PCSEL can achieve exactly this combination, attracting growing attention in recent years. Initially demonstrated in the infrared, and more recently in the visible, PCSELs raise the question: can this technology also be pushed into the UV?

This chapter begins with a brief overview of the state of the art in PCSEL research, followed by a discussion of fundamental operating principles. We then introduce the finite-size three-dimensional coupled-wave theory (3D-CWT) framework for modeling real, finite-sized PCSELs. This model is compared to an alternative approach, k-space weighted loss estimation (kSWLE), with a focus is on comparing and understanding the predicted losses of the optical modes by the two models as a function of photonic crystal geometry.

5.1 Introduction

To understand what sets PCSELs apart, it helps to have a look at how light stays within the cavity. Confining light, vertically and laterally, is essential for a laser to reach threshold and to control its spatial confinement and beam quality. EELs and VCSELs achieve this in very different ways, and PCSELs introduce a third approach. This difference in confinement mechanism is at the heart of why PCSELs can combine the strengths of both EELs and VCSELs.

In an EEL as shown in Fig. 5.1(a), vertical confinement is provided by a ridge waveguide: the core region has a higher refractive index than the cladding layers, so light is guided by total internal reflection and remains in the higher-index region, as if "attracted" to it. In optical terms, this higher-index region

acts like a potential well for light: as long as the boundaries change slowly, light remains trapped inside. Lateral confinement is partial and mainly comes from reflections at the cleaved mirror facets.

In a VCSEL, see Fig. 5.1(b), vertical confinement is provided by two highly reflective DBRs, forming a short Fabry–Pérot cavity. Lateral confinement is typically achieved with an aperture structure, which creates an effective index step in the transverse plane. This can be interpreted in the "effective index" picture (Secion 3.7) as a form of waveguiding. However, it arises from changes in mode phase and diffraction loss that have a lens-like effect, rather than from a bulk refractive-index increase as in the slab waveguide of an edge-emitting laser (EEL).

In a PCSEL, see Fig. 5.1(c), vertical confinement is again provided by waveguiding, as in an EEL, with a high-index core layer bounded by lower-index cladding layers. Lateral confinement, however, comes from the photonic crystal, a two-dimensional periodic modulation of the refractive index, which provides two-dimensional distributed feedback. The photonic crystal selectively couples guided waves together that satisfy the in-plane Bragg condition, leading to a discrete set of in-plane modes. Like a grating, it also couples part of the light out vertically giving rise to the surface emission. These modes form the allowed "guided" solutions, known as bands, of the 2D feedback system, and lasing occurs when one of them experiences sufficient gain to overcome its losses.

PCSELs inherit many benefits from both EELs and VCSELs. Due to the 2D feedback, the device area can be made larger than in EELs, enabling higher output powers. The large area also allows very small beam divergence, typically $\leq 1°$. This is much smaller than the typical $\gtrsim 10°$ for VCSELs that are limited by not being able to scale up the aperture due to the onset of multiple modes. PCSELs can be single mode even for large apertures if one mode is engineered to have lower losses than the others. From a fabrication perspective, their surface emission also enables wafer-level testing, similar to VCSELs.

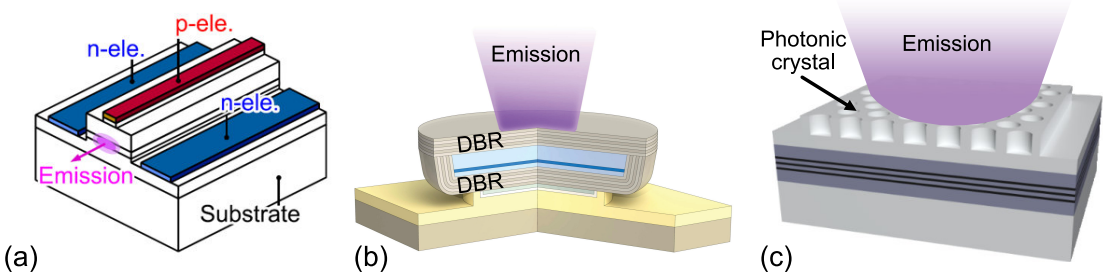

Figure 5.1: Schematic of: (a) EEL [205], (b) VCSEL, and (c) PCSEL.

There are many ways to model the band structure of an infinitely extending photonic crystal, including guided-mode expansion (GME) [206], rigorous coupled-wave analysis (RCWA) [207], finite-difference time-domain (FDTD)

[208], and coupled-wave theory (CWT) [209, 210]. However, real PCSELs have a photonic crystal of a finite lateral size, and to estimate optical losses in such lasers, both vertical radiation and lateral leakage must be carefully considered. In an ideal, infinitely extended PCSEL where the unit cell and its perturbation (e.g., a perfectly circular air hole) preserve the full lattice symmetry, certain modes are symmetry-protected and cannot couple to vertical radiation. In a finite device, however, the boundaries act as a perturbation, mixing the guided modes with other, potentially leaky modes, and introducing nonzero outcoupling rates [210]. This effect becomes increasingly important for smaller devices, making finite-size modeling essential for accurate loss estimation.

While FDTD can, in principle, capture both vertical and lateral losses, its prohibitive demands on simulation time and computer memory make it unsuitable for realistic PCSELs containing millions of unit cells [211, 212]. A practical alternative is finite three-dimensional coupled-wave theory (finite-CWT) [210], which can account for both vertical and lateral losses.

There is also another way, as implied by the title of Häggström's 2007 article [213], "Problem solving is often a matter of cooking up an appropriate Markov chain", almost anything can be tackled with a Markov chain, even the vertical and lateral losses in a PCSEL. More recently, this idea has been applied in the form of probabilistic Markov chain (PMC) modeling, where the photonic crystal is represented as a network of scattering sites that redistribute light according to coupling probabilities [214–217]. Its main limitation is that it does not explicitly track phase and interference effects between propagating waves. Such effects is, perhaps, to some extent implicitly included in the coupling constants which are used as coupling probabilities in the model.

The main drawback of finite-CWT, on the other hand, is that its underlying infinite photonic crystal bandstructure model relies on certain simplifications, as discussed in Paper C. This motivates the need for a more flexible framework in which more accurate infinite-structure models can be used. This motivation led to the development of kSWLE, a general method that enables the calculation of vertical and lateral losses for any underlying bandstructure model.

5.2 State-of-the-art: PCSELs

The first demonstration of lasing in a PCSEL was achieved in 1999 by Imada et al. using an InP-based structure emitting in the infrared (IR) at $\sim$1.27 µm [38]. This proof-of-concept established the viability of using a two-dimensional photonic crystal for both optical feedback and vertical outcoupling. Since then, the PCSEL concept has been extended across the near-IR and visible spectrum. The state-of-the-art IR PCSELs have demonstrated remarkable performance, with output powers exceeding 50 W in CW, single-mode operation and beam divergences as narrow as $< 0.05°$, as achieved by Kyoto University [39]. These devices benefit from the high material quality, mature fabrication processes in GaAs-based systems and used a square double lattice photonic crystal.

Figure 5.2 summarizes the evolution of III-nitride-based PCSELs over the past 20 years, highlighting the shift from optically pumped and electrically driven blue and UVA devices to optically pumped emitters in the UVC range. Solid markers indicate electrically injected devices, while open markers denote optically pumped devices. Transitioning toward shorter wavelengths, blue-emitting PCSELs based on InGaN quantum wells were first demonstrated in 2008 [44]. However, significant breakthroughs in performance came much later. In 2022, a high-power blue PCSEL emitting at 438 nm demonstrated 1 W output under pulsed operation and 320 mW in CW, establishing it as the highest-performing III-nitride PCSEL to date [58]. The device maintained high beam quality ($M^2 \sim 1$) and narrow divergence (0.2°), making it suitable for applications in laser lighting, display technologies, and machining of difficult-to-process materials such as copper and carbon-fiber reinforced plastics.

Green PCSELs were demonstrated more recently in 2024 [218], overcoming significant challenges such as the "green gap" [219] and increased strain in the quantum wells. These devices, operating near 520 nm, have been reported with tens of milliwatts of output power under pulsed operation, marking progress but still trailing the performance of their blue counterparts.

Pushing further into the ultraviolet, PCSELs are now being explored based on AlGaN. Our group recently demonstrated the first UVC-emitting PCSELs under optical pumping, achieving single-mode operation around 279 nm with beam divergence below 1°. These devices incorporate a hexagonal photonic crystal, etched into the p-side of the device in contrast to many other PCSELs that have an overgrown photonic crystal on the n-side. Our ongoing work aims to realize electrically injected UVC PCSELs, but this is complicated by the limited current spreading in AlGaN, as discussed in Section 2.4, which makes it difficult to achieve uniform injection across large apertures. This constraint likely necessitates reducing the PCSEL diameter; however, shrinking the device also increases optical lateral losses, and excessive losses may prevent lasing altogether. This trade-off between electrical injection uniformity and lateral optical losses motivates detailed investigations of in-plane loss mechanisms, e.g. using finte-CWT simulations.

5.3 PCSEL operation

Lasing threshold of a PCSEL is determined by the total loss of the laser. The total loss includes both the vertical radiation and lateral loss

$$g_{th} = \frac{1}{\Gamma_{QW}}\big(\alpha_{rad} + \alpha_{lat} + \alpha_{abs} + \alpha_{scat}\big), \tag{5.1}$$

where α_{rad} is the radiation loss, α_{lat} is the lateral in-plane loss, α_{abs} is the absorption loss, and α_{scat} is the scattering losses caused by lattice imperfections, hole roughness, or any other material defects in the semiconductor crystal or dielectrics. In many existing PCSEL simulation models (assuming an infinite

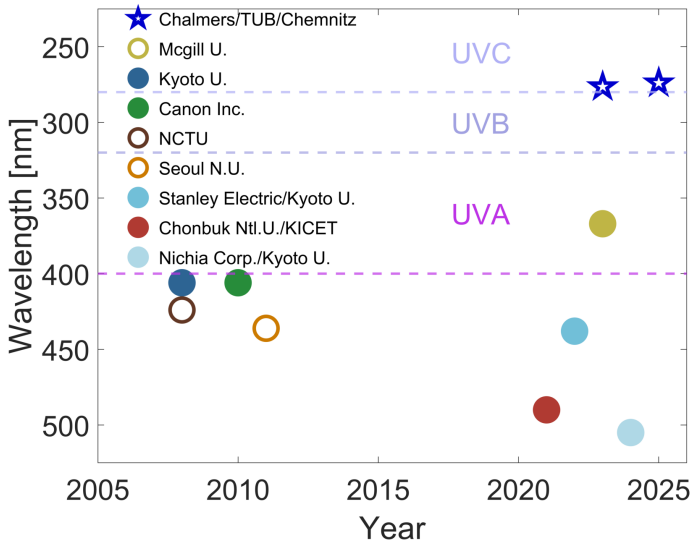

Figure 5.2: Timeline of demonstrated III-nitride PCSELs across the UV-visible spectrum [44,45,58,218,220–224]. Vertical axis shows emission wavelength; horizontal axis shows the year of demonstration. Solid markers = electrical injection; open markers = optical pumping.

PCSEL lattice) only α_{rad} is considered. Only considering vertical radiation is insufficient to determine the actual lasing mode since the lateral loss is absent. Especially in UVC PCSELs were the PCSEL has to be made smaller due to limited current injection, lateral loss plays a large role, or when highly symmetric hole shapes (such as circular holes) are used, then infinite PCSEL models predict zero radiation loss, which isn't true, and the field perturbation around the edges of the PCSEL causes radiation despite having symmetry protected modes.

In this section we discuss the photonic bandstructure, working principle of the PCSEL, and the origin of vertical radiation loss and the role of mode symmetries on the radiation losses. Lateral loss, however, is considered in the following sections of this chapter.

5.3.1 Bandstructure 101: a DBR analogy

Before discussing the two-dimensional photonic crystals used in PCSELs, it is useful to revisit the one-dimensional DBR, already familiar from VCSELs, as a simple example of a periodic optical system. In VCSELs, a DBR is typically analysed in terms of its reflectivity spectrum, where a broad high-reflectivity stopband enables low-threshold lasing. This same periodicity, when viewed from the perspective of an infinite structure, i.e. a DBR with an infinite number of DBR pairs, naturally leads to the concept of a photonic bandstructure, a central concept for understanding PCSELs.

A DBR consists of alternating layers with low and high refractive indices,

n_L and n_H, and thicknesses $d_L = \lambda_0/4n_L$ and $d_H = \lambda_0/4n_H$. The structure repeats with period $a = d_L + d_H$. By Bloch's theorem, in any periodic medium the electric field satisfies

$$E(x + a) = e^{jk_B a}E(x), \tag{5.2}$$

where k_B is the Bloch wavevector, which may be real (for propagating modes) or complex (for evanescent modes).

Using the transfer matrix method (TMM) discussed in Section 3.2.1, we can also express the periodicity of the electric field as

$$E(x + a) = ME(x), \tag{5.3}$$

where M is the transfer matrix for a single unit cell (one period of the infinite DBR) which can be expressed as

$$M = M_{inter,n_2,n_1} M_{prop,n_2} M_{inter,n_1,n_2} M_{prop,n_1}, \tag{5.4}$$

with M_{inter} and M_{prop} as defined in Section 3.2.1. Applying Bloch's theorem to Eq. (5.3) gives

$$ME(x) = e^{jk_B a}E(x), \tag{5.5}$$

which is an eigenvalue problem for M, with eigenvalues

$$\mu_\pm = e^{\pm jk_B a}. \tag{5.6}$$

For the 2x2 matrix M, the eigenvalues satisfy the characteristic equation

$$\mu^2 - Tr(M)\mu + \det(M) = 0, \tag{5.7}$$

where $Tr(M) = M_{11} + M_{22}$ is the trace of M. For a lossless DBR, $\det(M) = 1$, so the eigenvalues lie on the unit circle in the complex plane. Solving Eq. (5.7) yields the dispersion relation

$$\cos(k_B a) = \frac{1}{2}Tr(M) = \frac{1}{2}(M_{11} + M_{22}). \tag{5.8}$$

This expression directly relates the Bloch wavevector k_B to the layer parameters, and thus defines the photonic bandstructure of the infinite DBR. When $|\cos(k_B a)| \leq 1$, k_B is real and Bloch modes can propagate; when $|\cos(k_B a)| > 1$, k_B is complex and the mode is evanescent, corresponding to a photonic bandgap.

Figure 5.3(a,c) shows an example for a HfO_2/SiO_2 DBR. The shaded region marks the stopband in which no propagating Bloch modes exist. For a finite DBR with a given number of periods, the same stopband appears as a high-reflectivity region in the TMM-calculated spectrum, see Fig. 5.3(b,d), with slight deviations at the edges due to the finite number of periods. This direct correspondence between the infinite-structure bandgap and the finite-structure reflectivity stopband illustrates how the bandstructure perspective naturally generalises from the familiar 1D DBR to the 2D photonic crystals used in PCSELs, which will be discussed in the following sections.

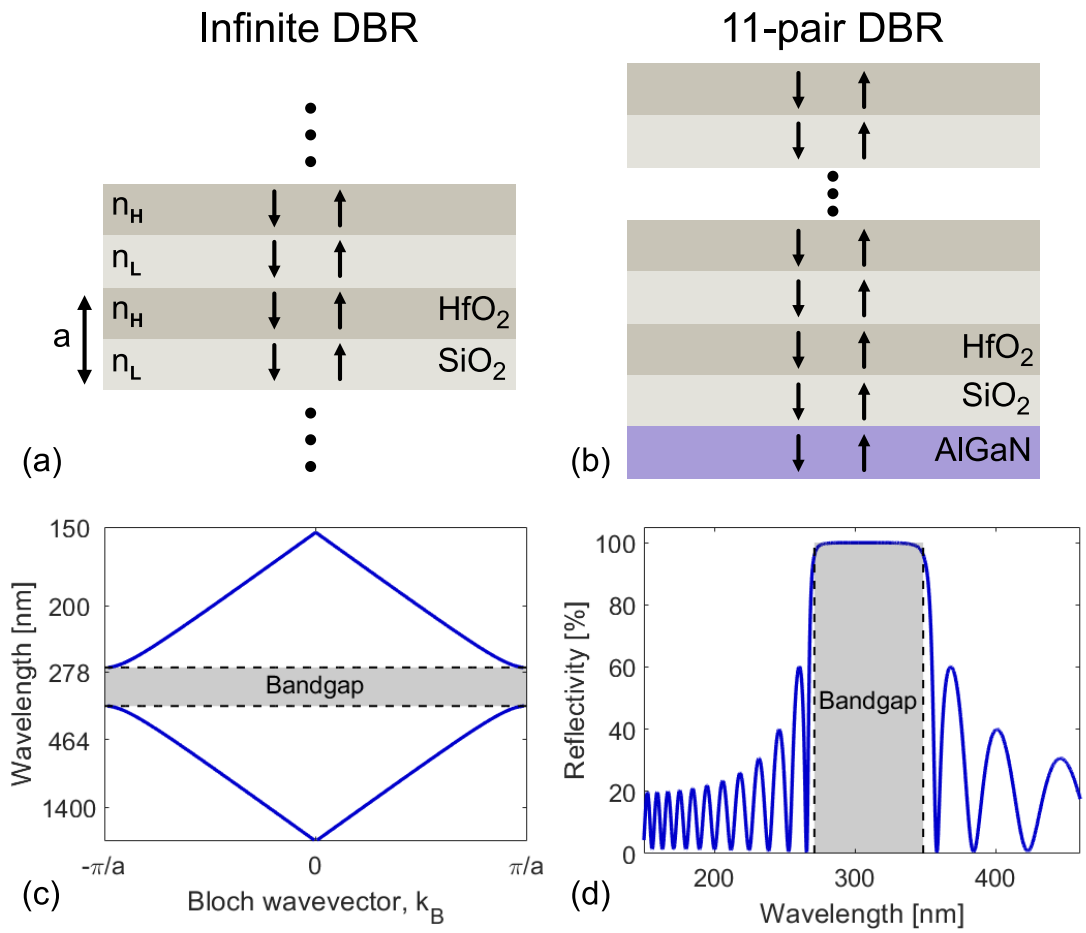

Figure 5.3: Illustration of the connection between the photonic bandstructure of an infinite DBR and the reflectivity spectrum of a finite DBR. (a) Schematic of an infinite periodic SiO_2/HfO_2 DBR. (b) Example of a finite DBR structure with 11 pairs of SiO_2/HfO_2 on an AlGaN substrate. (c) Photonic band diagram of the infinite SiO_2/HfO_2 DBR, calculated using the transfer matrix formalism and Bloch's theorem. The shaded region indicates the photonic bandgap, where the Bloch wavevector k_B is complex and no propagating Bloch modes exist. (d) Reflectivity spectrum of the finite 11-pair DBR calculated using the transfer matrix method. The high-reflectivity stopband (shaded) corresponds directly to the infinite-structure bandgap in (c). Small deviations from unity reflectivity near the band edges arise from the finite number of DBR periods.

5.3.2 Photonic band structure and 2D feedback in PCSELs

In the broadest sense, photonic crystals are periodic dielectric structures composed of alternating regions with high and low refractive index, with a periodicity on the order of the wavelength of light. Such structures resemble large-scale versions of atomic crystals, where the periodic potential modulates electron propagation. In photonic crystals, however, it is the periodic modu-

lation of the refractive index that governs photon propagation. This analogy highlights the close connection between photonic and semiconductor crystals, and there is a significant overlap in terminology and outcomes between these two fields.

In contrast to VCSELs, PCSELs do not rely on DBRs for feedback. Instead, they exploit the photonic bandstructure of a two-dimensional photonic crystal slab. At high-symmetry points of the Brillouin zone, such as the Γ-point, see Fig. 5.4, the group velocity of the Bloch modes approaches zero, leading to standing waves and a high-quality cavity that confines the optical mode. This mechanism provides strong in-plane feedback and enables large-area coherent oscillation. This allows PCSELs to support narrow-linewidth single-mode lasing across apertures much larger than those achievable in conventional VCSELs.

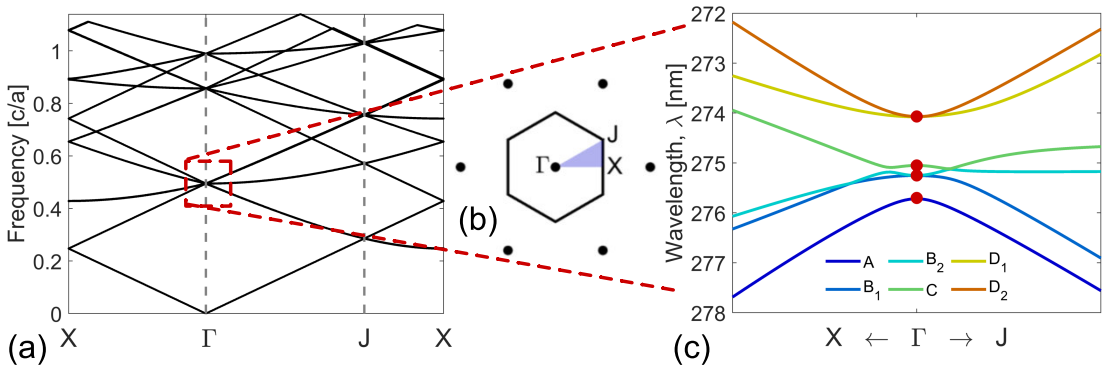

Figure 5.4: (a) Photonic bandstructure of a hexagonal photonic crystal slab along the $X-\Gamma-J$ directions, calculated using a 2D finite-element method (FEM) model in COMSOL. (b) First Brillouin zone of the hexagonal lattice, indicating the symmetry points. (c) Zoom-in around the second-order Γ-point, showing the six lowest-order bands. The red dots mark the zero-group-velocity points where Bloch modes form standing waves, providing the feedback mechanism for PCSEL operation.

PCSELs are typically designed to operate at the second-order Γ-point, since this provides both strong in-plane feedback from Bragg scattering in multiple directions (60°, 120°, and 180° couplings for a hexagonal lattice) and the vertical outcoupling occurs via first-order diffraction into the surface-normal direction [225]. In contrast, lasing at the X- or J-points also occurs at zero-group-velocity states but involves feedback only along restricted directions: at the X-point, coupling is limited to one-dimensional feedback along $\Gamma - X$, essentially forming six independent DFB-like cavities, while at the J-point lasing arises from two sets of 120° couplings [225, 226]. These geometries support tilted rather than surface-normal emission and do not offer the same coherence over large apertures. Higher-order Γ-points are also avoided, as they would require a larger lattice constant and lead to multiple diffraction orders that reduce the radiative efficiency.

The strength of the in-plane feedback in a PCSEL depends both on the photonic crystal design and vertical waveguide structure. Stronger periodic

modulation, determined by the hole fill factor and the refractive index contrast, increases the coupling between forward- and back-propagating waves. The mode overlap with the photonic crystal, Γ_{PC}, is also important since only the fraction of the optical mode residing in the photonic crystal layer contributes effectively to the feedback process. Finally, the device diameter $2L$ sets the interaction length over which feedback can accumulate, with larger apertures enabling stronger feedback and lower lateral losses.

5.3.3 Bandgap narrowing analogy

In semiconductors, disorder creates potential fluctuations which allow states to exist in regions where none previously did. These tail states, which can localize electrons and holes, effectively cause a narrowing of the electronic bandgap. In PCSELs, modes (states) represent coherent standing waves formed through Bragg diffraction. Here, disorder (e.g. irregularities in the hole shapes and placement, or crystal defects which can cause scattering) may disrupt the constructive interference required for coupling between specific reciprocal lattice vectors (like higher-order wavevector components) as discussed in Paper C. So rather than creating new states (as in semiconductors), disorder suppresses coupling to higher-order wavevector components by degrading phase coherence. A weaker optical feedback brings the photonic bands closer together, resulting in a smaller photonic bandgap. For example, this occurs when Γ_{PC} is reduced by moving the photonic crystal further away from the active region, which weakens the two-dimensional feedback. In this sense, the behavior resembles electronic bandgap narrowing. However, the underlying mechanism is different: one creates new localized states, while the other reduces the strength of feedback by disrupting coherent contributions from higher-order components.

This bandgap narrowing effect can for example be simulated by moving the PC away from the active region were the mode is located to decrease Γ_{PC}. As shown in Fig. 5.5 this has the effect of narrowing the separation between the bands in analogy to the bandgap narrowing of the bandgap in semiconductors.

5.3.4 Vertical outcoupling via diffraction in PCSELs

The 2D-photonic crystal also functions as a grating coupler [227], providing spatially coherent coupling across the device and enabling narrow-divergence surface emission. At the Γ-point, the lasing mode can be regarded as a standing wave formed by degenerate counter-propagating in-plane guided Bloch modes with a propagation constant approximately given by the waveguide mode $\beta \approx n_{eff}k_0$, where n_{eff} is the effective index of the mode and k_0 is the free-space wavevector. Although such a mode carries no net in-plane momentum at the Γ-point, it can still couple to radiation modes via Bragg diffraction from the photonic crystal.

For any guided mode inside the waveguide to radiate vertically, the in-plane component of its wavevector must match that of a radiated (or scat-

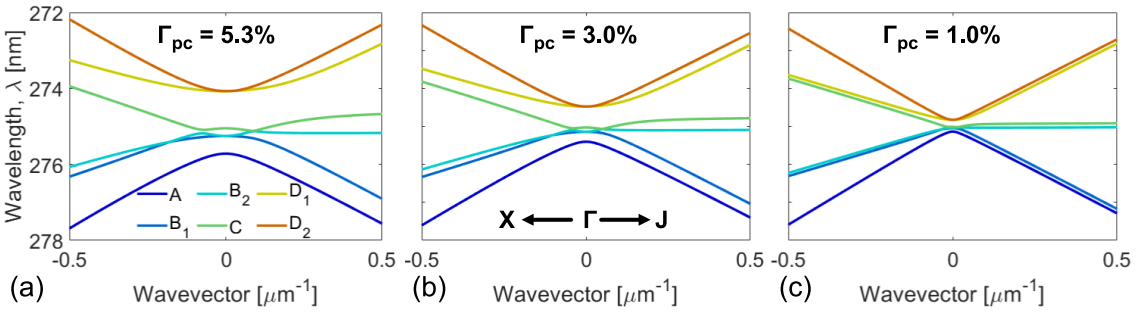

Figure 5.5: Infinite PCSEL bandstructure for a hexagonal lattice in the vicinity of the second-order Γ-point. Everything is the same in the simulations shown, including the fill-factor, $FF = 15\%$, except that the proximity of the PC layer is moved further away from the active region were the mode intensity is largest, thus decreasing the overlap between the mode and the PC layer, thereby reducing the feedback strength. (a) $\Gamma_{PC} = 5.3\%$. (b) $\Gamma_{PC} = 3.0\%$. (c) $\Gamma_{PC} = 1.0\%$.

tered/diffracted) mode in the external medium. This requirement, known as phase matching or in-plane momentum conservation, follows from Maxwell's equations, which demand continuity of the tangential electric and magnetic field components across an interface. In the presence of a photonic crystal, discrete reciprocal lattice vectors $|G|$ are available to provide or remove in-plane momentum in integer multiples of $q|G|$, where q is the diffraction order. The general phase-matching condition can be expressed as

$$k_0 n_i \sin\theta = \beta - q|G|, \tag{5.9}$$

where n_i denotes the refractive index of the medium into which radiation occurs (air or substrate) and θ is the diffraction angle relative to the surface normal. The sign of q indicates whether the grating momentum is added or subtracted from the guided mode's propagation constant.

The k-space diagram in Fig. 5.6 illustrates these conditions: the circles represent the maximum allowed in-plane wavevector for radiation into each medium, $k_0 n_{air}$ and $k_0 n_{sub}$. For diffraction to occur, the total in-plane wavevector of the diffracted mode, $\beta - q|G|$, must lie within the corresponding circle.

For the mode to remain guided in the slab waveguide, its propagation constant must satisfy $\beta = k_0 n_{eff} > k_0 n_{sub} > k_0 n_{air}$, which ensures confinement by total internal reflection. This inequality implies that any radiated diffraction order must have less in-plane momentum than the guided mode, which in turn motivates the use of the minus sign in Eq. (5.9) for emission.

In a PCSEL, it is typically desirable to have emission in the surface-normal direction (i.e. $\theta = 0$), which simplifies Eq. (5.9) to

$$a = q\frac{\lambda_0}{n_{eff}} \quad \text{for square lattice,} \tag{5.10}$$

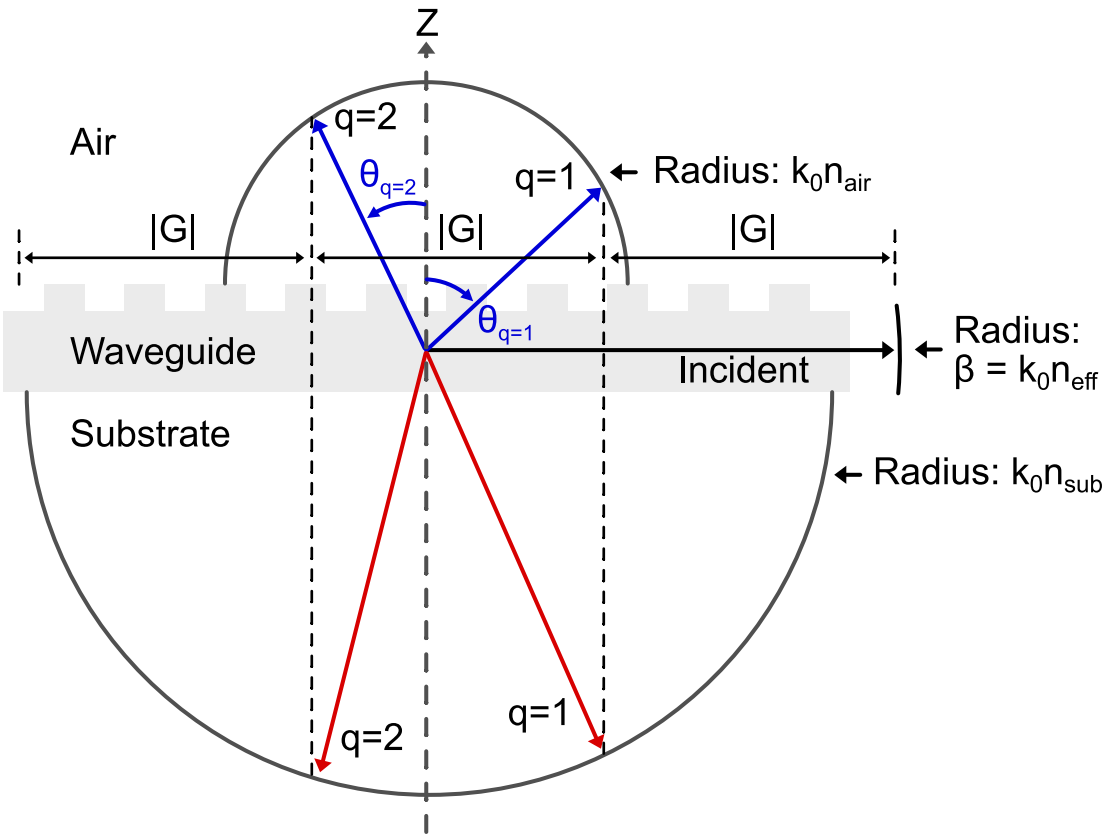

Figure 5.6: k-space diagram showing possible diffraction orders of a PCSEL. A guided wave incident upon a grating will couple some energy into diffracted waves. The angle at which diffracted beams leave is determined by the phase matching conditions. The circle radii represent the maximum allowed in-plane wavevector for radiation into each medium (air or substrate), i.e. $k_0 n_{air}$ and $k_0 n_{sub}$.

or

$$a = q\frac{2}{\sqrt{3}}\frac{\lambda_0}{n_{eff}} \quad \text{for hexagonal lattice,} \tag{5.11}$$

where $|G| = 2\pi/a$ for a square lattice, $|G| = 4\pi/(\sqrt{3}a)$ for a hexagonal lattice, and a is the lattice constant, i.e., the center-to-center spacing between adjacent holes. In addition to requiring surface-normal emission, it is also desirable to restrict the output to a single diffraction order, so that only one beam emerges from the PCSEL. This condition is satisfied when $q = 1$. Then, higher orders ($q \geq 2$) fall outside the allowed k-space region for radiation into air, as seen in Fig. 5.6. This is because the magnitude of $\beta - q|G|$ exceeds $k_0 n_{air}$.

Using a subwavelength lattice ($a \leq \lambda_0/n_{eff}$ for square, $a \leq 2\lambda_0/(\sqrt{3}n_{eff})$ for hexagonal) ensures that only the $q = 1$ order is phase-matched for vertical outcoupling. From a fabrication perspective, this requirement forces the lattice constant to shrink as λ_0 decreases. In the UVC, where λ_0 is short ($< 280\,\text{nm}$), the smaller lattice constant makes hole etching more challenging and increases

the risk of neighboring holes merging since the holes have not perfectly vertical side-walls, especially during deep etching. At the top surface where the etching starts, the hole diameter can be wider than intended due to lateral etching, so adjacent holes may touch at the surface even if the diameter deeper in the etch is close to the target. The hexagonal lattice offers a modest advantage: for the same diffraction condition, its lattice constant is $2/\sqrt{3} = 1.154$ times larger than in a square lattice, relaxing fabrication tolerances.

5.3.5 Radiation loss and the role of symmetry

The efficiency of vertical radiation outcoupling in PCSELs depends on both the photonic lattice's Fourier spectrum and the spatial symmetry of the optical mode. At the Γ-point, symmetry arguments predict that in a hexagonal lattice with circular symmetric holes, the modes such as A, B_1, B_2, and C are non-radiative, while D_1 and D_2 are radiative. Sometimes these arguments are illustrated by plotting selected field components, for example the real parts of the in-plane electric fields (E_x, E_y) and the real part of the out-of-plane magnetic field (H_z). An example is shown in Fig. 5.7(a-b) for the non-radiative A mode and the radiative D_1 mode. However, such partial field plots can be misleading, since they do not represent the full power flow or phase relations. Examining only selected components (E_x, E_y, or H_z) is insufficient to determine radiative losses, because the net Poynting flux depends on the complete vector field and relative phase. To rigorously assess whether a mode is radiative or non-radiative, one must evaluate the vertical component of the Poynting vector

$$S_z = \frac{1}{2}\mathrm{Re}\big(E_x H_y^* - E_y H_x^*\big), \tag{5.12}$$

where S_z describes the power flow in the vertical direction. Figures 5.7(c–d) illustrate this for the A and D_1 modes. Although both appear antisymmetric in H_z, the the computed Poynting flux reveals a key difference: destructive interference cancels the outgoing contributions for the A mode, while for the D_1 mode they add constructively, leading to strong vertical radiation.

In approximate models such as finite-CWT that are needed to simulate finite-sized PCSELs, the full vectorial fields are not solved. Instead, only the in-plane electric fields are retained, and radiation loss is estimated from the overlap of these fields with vertical radiation channels. The radiated power is taken as

$$\text{Radiated power} \propto \left| \int_{\text{unit cell}} \mathbf{E}_{||}(\mathbf{r}) \cdot \mathbf{E}_{rad}^*(\mathbf{r}) d\mathbf{r} \right|^2, \tag{5.13}$$

where $\mathbf{E}_{||}$ is the in-plane electric field of the mode and $\mathbf{E}_{rad}$ is the field pattern of the radiated plane wave. While this neglects the full vectorial nature of Poynting analysis, it captures the essential symmetry-based selection rules that govern vertical leakage, and has been shown to agree well with full-wave simulations [228].

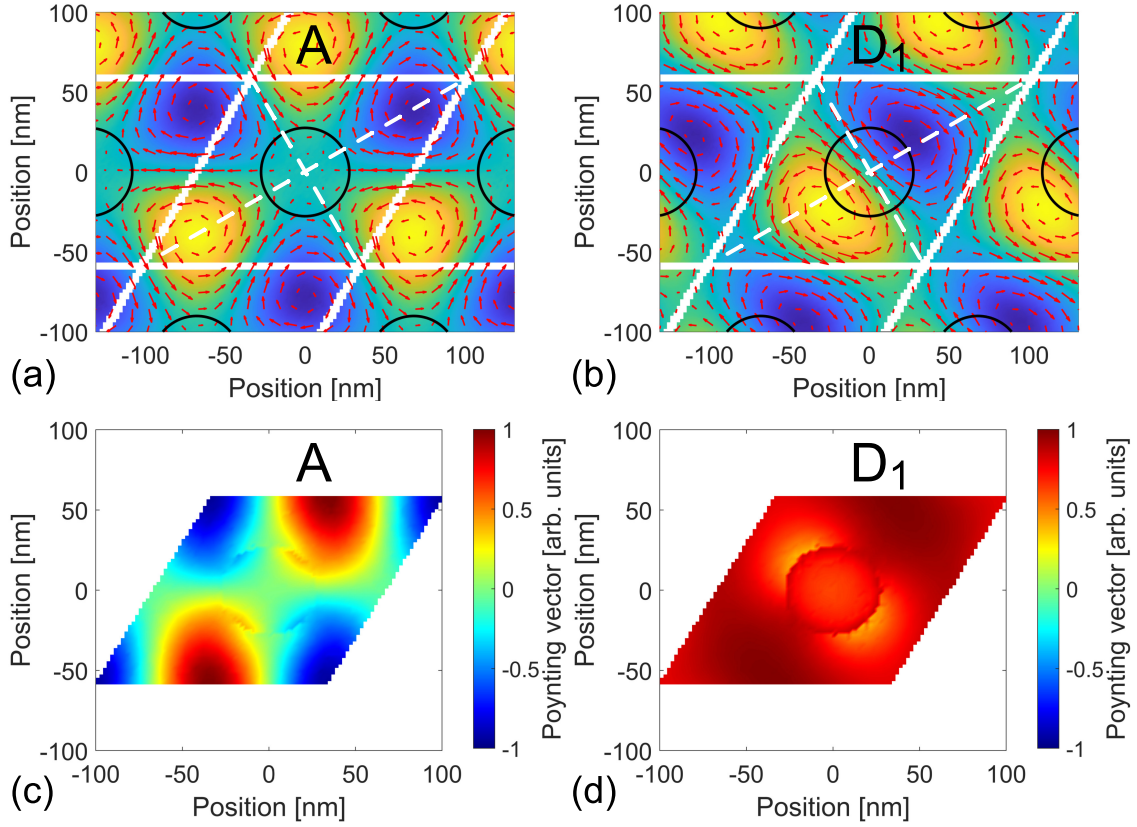

Figure 5.7: 3D COMSOL finite element method simulations of the non-radiative A mode (a,c) and the radiative D_1 mode (b,d). (a–b) In-plane electric field $\mathrm{Re}(E_x, E_y)$ (arrows) and magnetic field $\mathrm{Re}(H_z)$ (color map), which exhibit similar symmetry features for both modes. The black circles indicate air holes in the photonic crystal lattice. (c–d) Corresponding normalized vertical Poynting vector S_z. For the A mode (c), destructive interference of the radiated contributions cancels the net power flow, resulting in negligible radiation. For the D_1 mode (d), the radiative contributions add constructively, leading to strong vertical leakage.

5.4 Finite-size three-dimensional coupled-wave theory

To model the optical properties of PCSELs, we have implemented a three-dimensional coupled-wave theory (3D-CWT) framework based on the method developed by Yong Liang et al. [209, 210, 228]. Unlike full-field numerical methods such as FDTD or FEM, which are computationally demanding for large-area photonic structures, the 3D-CWT offers a semi-analytical approach that efficiently captures the essential physics near the second-order Γ-point. It extends conventional coupled-wave theory [229] by including in-plane distributed feedback from the photonic crystal together with vertical emission into free space, enabling the calculation of both lateral-leakage and vertical radiation

loss.

The electromagnetic field is expanded into six in-plane Bloch waves (R_1, S_1, R_2, S_2, R_3, S_3) near the second-order Γ-point. These waves couple through both the photonic-crystal periodicity and the cavity geometry, and their common vertical profile is computed using the transfer-matrix method [230]. The finite-size problem is formulated as a generalized eigenvalue equation, discretized on a staggered-hexagonal grid to account for the device geometry [228], as shown in Fig. 5.8. This formulation describes the evolution of the wave amplitudes across the lateral plane. For modes at the Γ-point, the generalized eigenvalue problem becomes [210]

$$(\gamma + j\alpha_{tot}) \begin{bmatrix} R_1 \\ S_1 \\ R_2 \\ S_2 \\ R_3 \\ S_3 \end{bmatrix} = \mathbf{C} \begin{bmatrix} R_1 \\ S_1 \\ R_2 \\ S_2 \\ R_3 \\ S_3 \end{bmatrix} + j \begin{bmatrix} \frac{1}{2}\,\partial R_1/\partial x - \frac{\sqrt{3}}{2}\,\partial R_1/\partial y \\ -\frac{1}{2}\,\partial S_1/\partial x + \frac{\sqrt{3}}{2}\,\partial S_1/\partial y \\ \frac{1}{2}\,\partial R_2/\partial x + \frac{\sqrt{3}}{2}\,\partial R_2/\partial y \\ -\frac{1}{2}\,\partial S_2/\partial x - \frac{\sqrt{3}}{2}\,\partial S_2/\partial y \\ \partial R_3/\partial x \\ -\,\partial S_3/\partial x \end{bmatrix} \tag{5.14}$$

Here, the 6×6 matrix $\mathbf{C}$ contains the coupling coefficients between the waves and incorporates vertical radiation losses [210]. The real part of the eigenvalue corresponds to the frequency detuning δ from the Bragg condition, while the imaginary part α_{tot} represents the total modal loss, including both vertical radiation and lateral leakage. This formulation enables the calculation of field profiles, far-field patterns, and threshold modal gain, and has been shown to agree well with experimental observations [210]. As shown in Paper C, the total loss, α_{tot}, can be separated into vertical and lateral components:

$$\alpha_{rad} = \frac{\iint 2\,\mathrm{Im}\,(\boldsymbol{A}_H \boldsymbol{C} \boldsymbol{A})\,dxdy}{\iint \sum_{j=1}^{6} |\boldsymbol{A}(i)|^2 dxdy}, \tag{5.15}$$

and

$$\alpha_{lat} = \frac{\sum_{j=1}^{3} \iint \partial/\partial x_j \left(|R_j|^2 - |S_j|^2\right) dxdy}{\iint \sum_{j=1}^{6} |\boldsymbol{A}(i)|^2 dxdy}, \tag{5.16}$$

where $\mathbf{A} = [R_1, S_1, R_2, S_2, R_3, S_3]^T$ contains the wave amplitudes in each cell.

In the infinite-size limit, the lateral derivatives vanish and Eq. (5.14) simplifies to $(\gamma + j\alpha_{rad})\mathbf{A} = \mathbf{C}\mathbf{A}$. By using this form, it is possible to calculate the dispersion relation of an infinite PCSEL structure by introducing a small perturbation to the in-plane wavevector $\Delta\vec{k}$ around the second-order Γ point. However, this α_{rad} excludes finite-size effects, which can substantially increase the radiation loss of the highly symmetric A, B_1, B_2, and C modes in a hexagonal lattice.

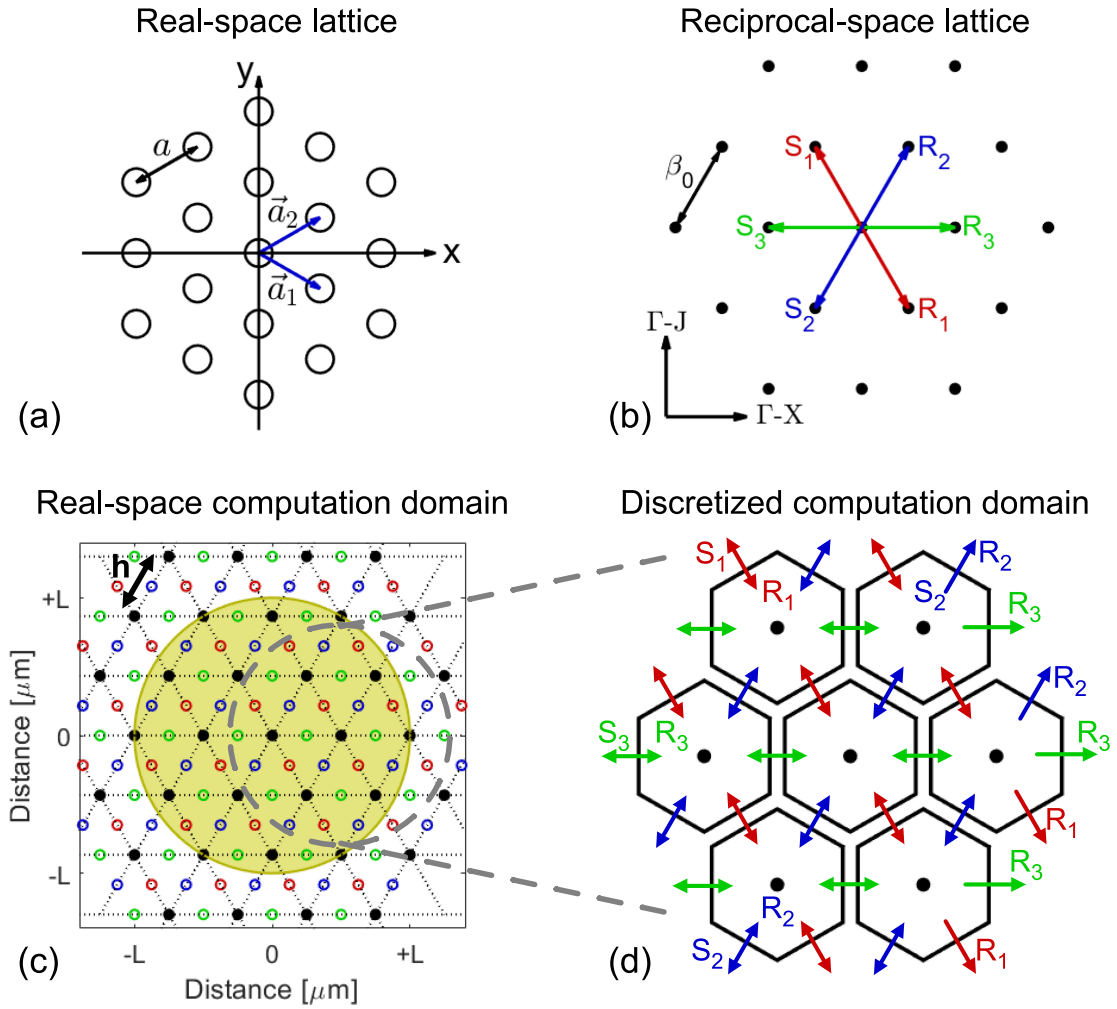

Figure 5.8: Illustration of 3D-CWT for a hexagonal-lattice PCSEL. (a) Real-space lattice. (b) Reciprocal lattice with forward (R_i) and backward (S_i) fundamental waves along the three principal axes. (c–d) Finite-size computation domain: the lattice is discretized over a circular device of radius $L = Nh$ (h is the grid spacing; $N = 2$ in (c) for clarity; $N \geq 7$ results in good convergence). Black solid markers denote positions where the the fields for the infinite PCSEL are solved to obtain the 6×6 coupling matrix $\mathbf{C}$ (these points are not part of the finite-difference grid). These points represent a domain that contains many real-space PCSEL unit cells (with lattice constant a), and is therefore much larger than a single unit cell. Colored hollow points are the finite-difference grid on which the finite PCSEL problem is solved. As shown in (d), each border region supports six outward-propagating waves (both R_i and S_i) that couple to neighboring cells; at the outer boundary we impose a non-reflecting condition so all power crossing this boundary leaves the PCSEL.

5.4.1 Discretization

To solve Eq. (5.14) numerically we must first discretize it, i.e.

$$\big(\delta + i\alpha_{tot}\big)\underbrace{\frac{1}{2}\mathbf{M}\overbrace{\begin{bmatrix}\mathbf{A}_1\\ \mathbf{A}_2\\ \vdots\end{bmatrix}}^{\substack{\text{stored values at}\\ \text{cell interfaces}}}}_{\substack{\text{interpolated values}\\ \text{at cell centers}}} = \tilde{\mathbf{C}}\frac{1}{2}\mathbf{M}\begin{bmatrix}\mathbf{A}_1\\ \mathbf{A}_2\\ \vdots\end{bmatrix} + i\underbrace{\frac{1}{h}\mathbf{D}\begin{bmatrix}\mathbf{A}_1\\ \mathbf{A}_2\\ \vdots\end{bmatrix}}_{\substack{\text{derivatives}\\ \text{at cell centers}}}, \tag{5.17}$$

where $\mathbf{A}_m = [R_1^m, S_1^m, R_2^m, S_2^m, R_3^m, S_3^m]^T$ are the fundamental wave amplitudes stored at the borders of cell m, see Fig. 5.8(b-d), and m is the cell number. The block matrix $\tilde{\mathbf{C}}$ is given by

$$\tilde{\mathbf{C}} = \begin{bmatrix}\mathbf{C} & & \mathbf{O}\\ & \mathbf{C} & \\ \mathbf{O} & & \ddots\end{bmatrix}, \tag{5.18}$$

where $\mathbf{C}$ is the 6x6 matrix obtained by solving the infinite PCSEL structure problem [210]. The matrix $\mathbf{M}$ can be populated

$$M_{6m+r,\,6n+s} = \begin{cases}1, & \text{if } r = s \text{ and } m = n\\ & \text{or } r = s \text{ and } (p,q)_m = (p,q)_n + \mathbf{d}_r,\\ 0, & \text{otherwise,}\end{cases}$$

where $r, s = 1, ..., 6$ are the row and column indices for the 6x6 cell block with row m and column n, and $(p,q)_{m/n}$ are the spatial coordinates of the current cell (m) and any cell (n). The vector $\mathbf{d}_r$ specifies the direction for each wave component, as illustrated in Fig. 5.8(b-d), and is used to check if cells are adjacent or not, and is given by

$$\mathbf{d}_r = \begin{cases}(1,0), & r = 1\ (R_1),\\ (-1,0), & r = 2\ (S_1),\\ (0,1), & r = 3\ (R_2),\\ (0,-1), & r = 4\ (S_2),\\ (1,1), & r = 5\ (R_3),\\ (-1,-1), & r = 6\ (S_3).\end{cases} \tag{5.19}$$

The matrix $\mathbf{D}$ is analogous to $\mathbf{M}$, but with off-diagonal entries set to -1. For a grid with N subdivisions ($L = Nh$, and h is the distance between two grid points as defined in Fig. 5.8(c)), the total number of cells is $3N(N+1)+1$. The full matrices $\mathbf{M}$, $\mathbf{D}$ and $\tilde{\mathbf{C}}$ are therefore of size $6[3N(N+1)+1]$ x $6[3N(N+1)+1]$.

Equation 5.17 is a generalized eigenvalue problem, but it can be converted to a standard eigenvalue problem by multiplying both sides by $2\mathbf{M}^{-1}$

$$\left(\delta + i\alpha_{tot}\right) \begin{bmatrix} \mathbf{A}_1 \\ \mathbf{A}_2 \\ \vdots \end{bmatrix} = \mathbf{M}^{-1} \left(\tilde{\mathbf{C}}\,\mathbf{M} \begin{bmatrix} \mathbf{A}_1 \\ \mathbf{A}_2 \\ \vdots \end{bmatrix} + i\,\frac{2}{h}\,\mathbf{D} \begin{bmatrix} \mathbf{A}_1 \\ \mathbf{A}_2 \\ \vdots \end{bmatrix} \right), \tag{5.20}$$

which can be solved with standard eigenvalue solvers, with computation times of a few seconds. The wavelength of the modes can be computed from the obtained frequency deviation δ as

$$\lambda = \frac{2\pi n_{eff}}{\beta_0 + \delta}. \tag{5.21}$$

As an example, Fig. 5.9 shows a finite-size 3D-CWT simulation obtained by solving Eq. (5.20) for a UVC PCSEL with $a = 136\,\text{nm}$, $FF = 15\%$, and diameter $2L = 300\,\mu\text{m}$. The normalized threshold gain $\alpha_{tot}L$ is shown as a function of mode frequency deviation in Fig. 5.9(b). To identify which of these finite-size solutions correspond to the fundamental modes ($A - D_2$), a mode decomposition is carried out following the procedure described in Paper C. Figure 5.9(c) shows the fractional power overlap with the infinite-structure eigenmodes, while Fig. 5.9(d) shows the corresponding near-field patterns. For this large PCSEL diameter, the fundamental finite-size modes closely resemble the infinite ones. The A, B_1, B_2, and C modes can be identified, as indicated by the colored frames in Fig. 5.9(d). Additional modes are also visible, including the whispering-gallery W-mode [210,231] (mode index 2), higher-order C-modes (indices 5 and 6), and higher-order B_1 and B_2 modes (indices 7 and 8).

5.5 Loss dependence on PCSEL diameter

The total modal losses in a PCSEL depend strongly on the finite device size. As the diameter decreases, both lateral and radiation losses increase, even for modes that would be perfectly bound in the infinite structure. This finite-size dependence is crucial to explain why PCSELs with circular holes can emit light: in an infinite PCSEL model, the modes would still lase internally but with zero outcoupling, i.e. no external emission would be observed. Finite device boundaries provide the necessary perturbation for outcoupling to occur.

To illustrate, we simulated a UVC PCSEL with a hexagonal lattice of circular air holes, varying the device diameter. The results (Fig. 5.10) show that for large diameters, the total loss is dominated by radiation, and the six fundamental modes $A - D_2$ exhibit negligible lateral leakage. As the diameter is reduced, however, the finite PCSEL boundary perturbs the in-plane fields, and both lateral and radiation losses increase.

The lateral losses in Fig. 5.10(b) follow a scaling of approximately $\approx 1/L^2$. This can be understood from a simple boundary argument: the fraction of the

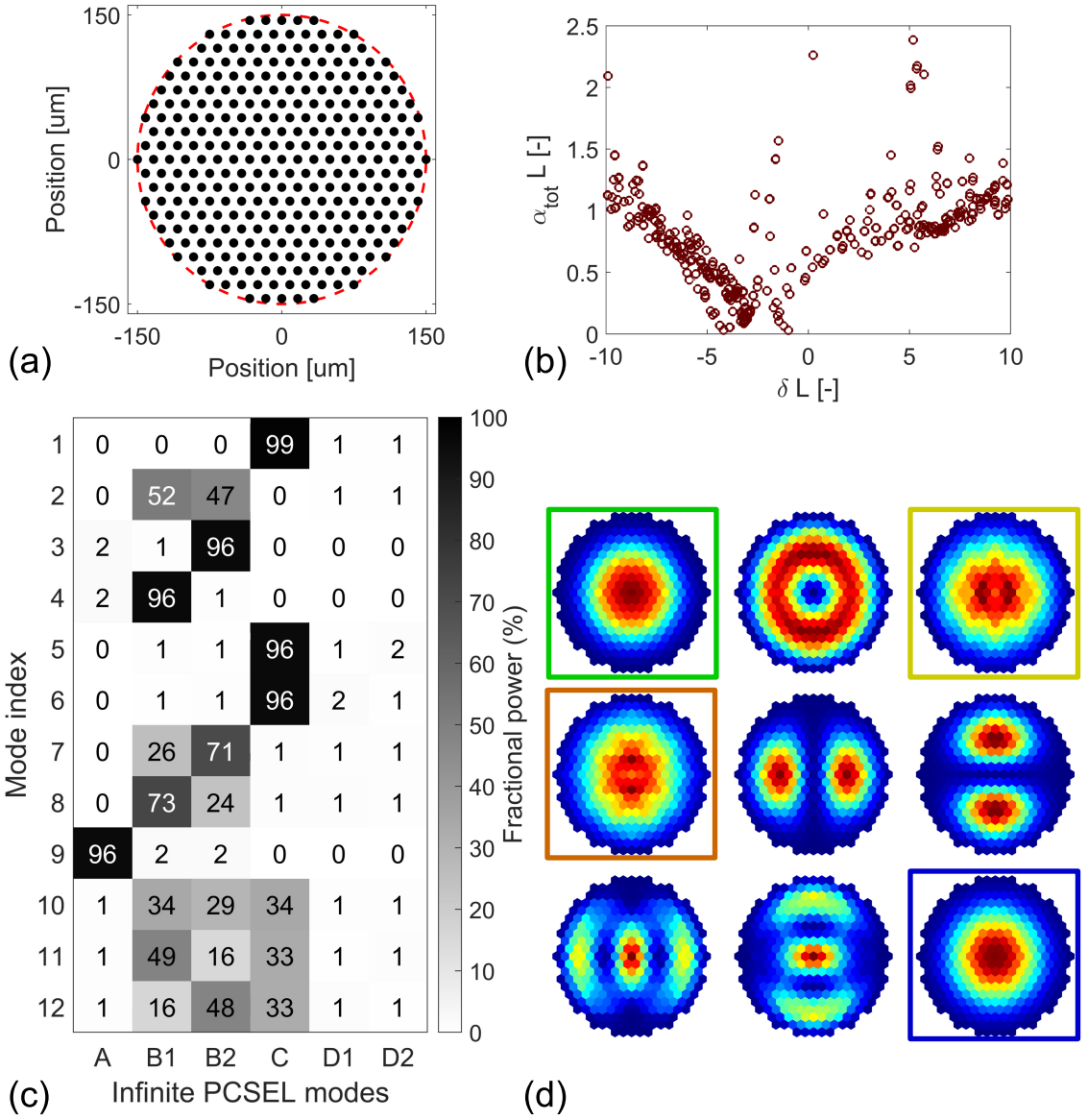

Figure 5.9: A finite-size 3D-CWT simulation of a UVC PCSEL. (a) Discretization of the computational domain with device diameter $2L = 300\,\mu\text{m}$ and grid size $N = 9$. (b) Normalized threshold gain $\alpha_{tot}L$ from Eq. (5.20) as a function of normalized frequency deviation δL. (c) Mode decomposition of the first 12 lowest-loss finite solutions into the eigenmodes of the infinite structure ($A - D_2$), showing the (rounded) fractional power contained in each band. (d) Near-field mode profiles of the lowest-loss modes with mode index 1-9. The fundamental modes C (index 1, green), B_1 (index 4, yellow), B_2 (index 3, orange), and A (index 9, blue) are highlighted by squares. $FF = 15\%$, $a = 136\,\text{nm}$, and $\Gamma_{PC} = 5.3\%$.

mode field leaking out from the device boundary scales with the perimeter-to-area ratio $2\pi L/(\pi L^2) \sim 1/L$. Since the power loss is quadratic in the field amplitude, the resulting power loss scales as $\sim 1/L^2$.

The radiation losses in Fig. 5.10(c) also show an approximate $\approx 1/L^2$ dependence for modes B_1, B_2, and C. This behavior can be interpreted as diffraction from a finite aperture: a mode confined to a disk of diameter $2L$ produces an angular spread of $\theta \sim \lambda/(2L)$. The total radiated power is obtained by integrating the radiation intensity over the divergence cone. Assuming the intensity is approximately constant, I_0, across this narrow cone, we can write

$$P_{rad} = I_0 \int_0^{2\pi} d\varphi \int_0^{\theta} \sin\vartheta d\vartheta = 2\pi I_0(1-\cos\theta) \approx \pi I_0 \theta^2, \tag{5.22}$$

where the last step uses the small-angle approximation $\cos\theta \approx 1 - \theta^2/2$. The radiation loss coefficient is then obtained by normalizing the radiated power to the mode energy U and group velocity v_g

$$\alpha_{lat} \sim \frac{P_{rad}}{v_g U} \propto \pi I_0 \theta^2 \propto \left(\frac{\lambda}{L}\right)^2, \tag{5.23}$$

consistent with the observed $\approx 1/L^2$ trend for the B_1, B_2, and C modes in Fig. 5.10(c). Thus, both lateral and radiation losses in finite PCSELs naturally follow an inverse-square scaling with device size, explaining why small devices experience large losses.

5.6 Far-field emission pattern for identification of lasing modes

When measuring the bandstructure below threshold in real devices, the bands are typically broad, making it difficult to resolve the exact wavelength of each mode [45]. Above threshold, the lasing line may also shift relative to the below-threshold photonic bandstructure. Such shifts can arise from spatial variations in lattice constant, fill-factor, hole depth, hole tilt, or other imperfections across the PCSEL area. For devices with circular holes, most emission originates from the edges of the device with radius L. If lasing begins only locally rather than uniformly across the PCSEL, the emission may instead come from regions other than the perimeter at radius L. In that case, the measured lasing wavelength may deviate from the below-threshold bandstructure due to spatial gradients in fabrication parameters.

Since it may be challenging to identify the lasing modes experimentally by bandstructure measurements, an alternative approach is needed. One way is to experimentally measure the far-field emission pattern and its polarization components and compare those to simulated ones. Finite-CWT simulations allow calculation of the far-field intensity and polarization for the $A-D_2$ modes, assuming the lattice orientation shown in Fig. 5.8(a-b). Proper experimental alignment is therefore important to enable comparison with simulations. Non-radiative modes exhibit characteristic doughnut-shaped far-fields, which can be understood from the radiation loss dispersion (Fig. 5.16). Near the Γ-point,

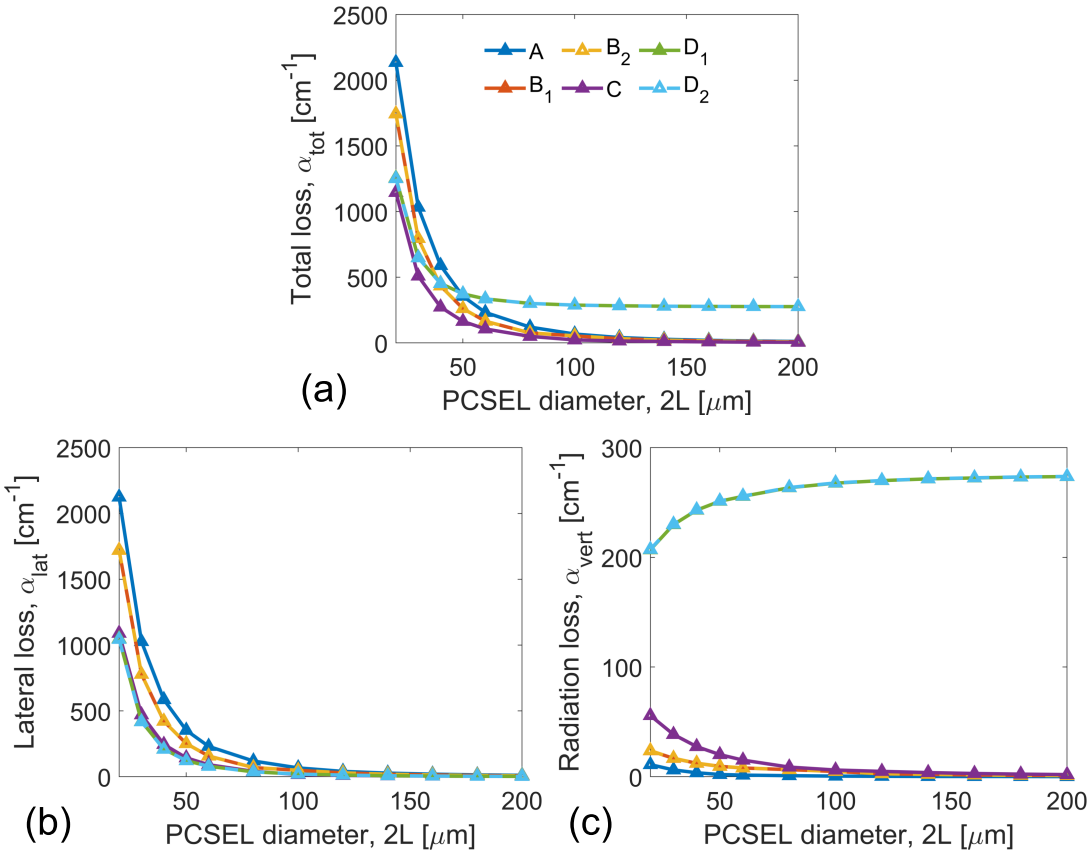

Figure 5.10: Simulated total (a), lateral (b), and radiation (c) modal losses of a UVC PCSEL with a hexagonal lattice of circular air holes, shown as a function of device diameter for the six fundamental modes $A - D_2$. $FF = 15\%$, $a = 136\,\text{nm}$, and $\Gamma_{PC} = 5.3\%$.

the loss dispersion is approximately parabolic, leading to negligible emission at Γ and a ring-shaped doughnut pattern see Fig. 5.11. Weak side lobes in the calculated far-field originate from numerical artifacts due to the abrupt truncation of the radiation field in the simulation [210].

While most lasing modes can be distinguished by analyzing the far-field emission and its polarization components, in a hexagonal lattice the B_2 and C modes cannot be uniquely identified in this way, since both exhibit very similar doughnut-shaped far-field and close to identical polarization-resolved patterns as shown in Fig. 5.11.

Further insights into how the PCSEL lase can be obtained by studying the FWHM of the far-field. The FWHM scales with PCSEL diameter, following the classical diffraction "rule-of-thumb" for a circular aperture

$$\theta_{FWHM} = C\frac{\lambda_0}{2L}, \tag{5.24}$$

where C is a fitting constant. Analytically, diffraction of a plane wave through

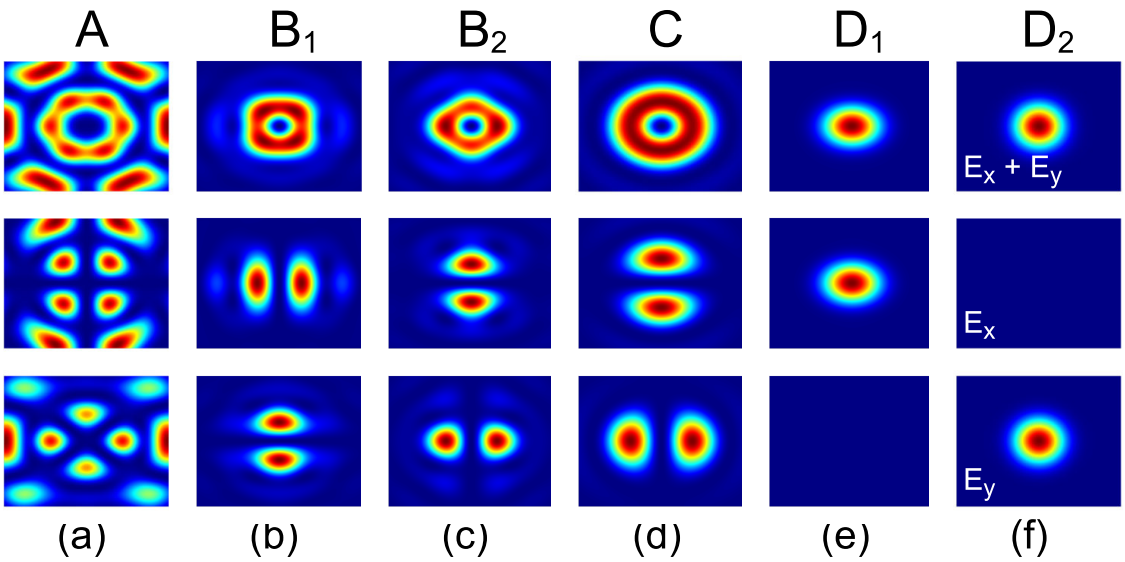

Figure 5.11: Simulated far-field emission of modes $A-D_2$. Each column corresponds to one mode. The first row shows the total far-field, while the second and third rows show the x- and y-polarized components, respectively. $FF = 15\%$, $a = 136\,\text{nm}$, and $\Gamma_{PC} = 5.3\%$.

a circular aperture gives $C = 2.44$ [95]. For the C-mode, the simulated far-field fits well with $C = 2.32$, as shown in Fig. 5.12, confirming the expected inverse scaling of beam divergence with aperture size. This explains why PCSELs, with diameters typically exceeding 100 µm, can achieve extremely small beam divergence compared to VCSELs, which typically have diameters below 10 µm.

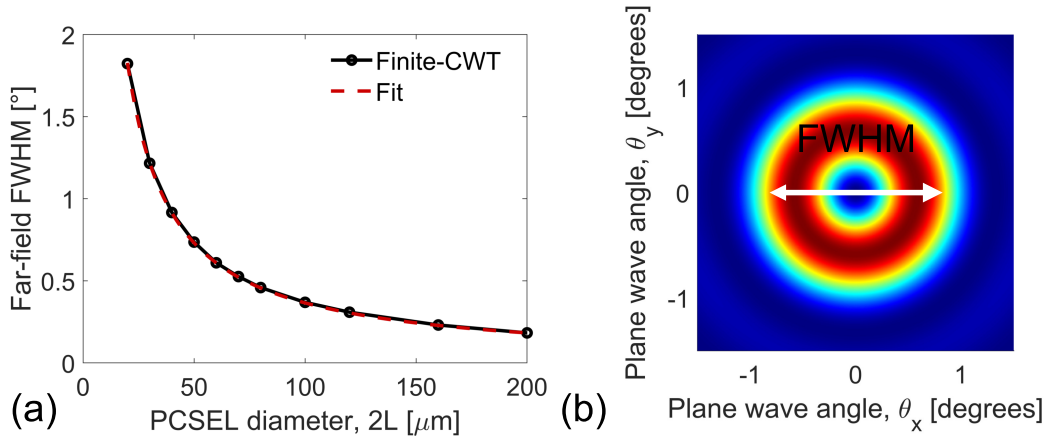

Figure 5.12: (a) Simulated FWHM beam divergence of the C-mode as a function of PCSEL diameter, $2L$. (b) Far-field intensity of the C-mode showing the characteristic doughnut-shaped profile (linear-scale). $FF = 15\%$, $a = 136\,\text{nm}$, and $\Gamma_{PC} = 5.3\%$.

5.7 Hexagonal vs square lattices and hole shape effects

The in-plane coupling strength in a photonic crystal laser depends both on the lattice geometry including hole shape and Γ_{PC}. In a square lattice, the fundamental couplings can be divided into 1D coupling at 180° (κ_{1D}) and 2D coupling at 90° (κ_{2D}). In contrast, a hexagonal lattice gives rise to three types of coupling due to its higher symmetry: 1D coupling at 180° (κ_{1D}), and 2D couplings at 60° (κ_{2Da}) and 120° (κ_{2Db}), as illustrated in Fig. 5.13. A key distinction between a square and hexagonal lattice is that the 2D coupling coefficients are generally stronger in hexagonal lattices than in square lattices [58, 221]. This is because the hexagonal lattice supports two independent channels for 2D feedback (κ_{2Da} and κ_{2Db}), while the square lattice has only one (κ_{2D}). The coupling coefficients can be calculated from the Fourier components of the unit cell's permittivity distribution as [229, 232, 233]

$$\kappa_G = -\frac{\pi}{\lambda_0\sqrt{\epsilon_{avg}}}\epsilon_G, \tag{5.25}$$

where ϵ_G are the Fourier coefficients of the permittivity of the unit cell. For the square lattice, the lowest-order couplings are given by $\kappa_{2D} = \Gamma_{PC}\kappa_G(|G| = \sqrt{2}\beta_0)$ and $\kappa_{1D} = \Gamma_{PC}\kappa_G(|G| = 2\beta_0)$, where $\beta_0 = 2\pi/a$. For the hexagonal lattice, the 2D couplings at 60° and 120° arise from $\kappa_{2Da} = \Gamma_{PC}\kappa_G(|G| = \beta_0)$ and $\kappa_{2Db} = \Gamma_{PC}\kappa_G(|G| = \sqrt{3}\beta_0)$, while 1D (180°) coupling is given by $\kappa_{1D} = \Gamma_{PC}\kappa_G(|G| = 2\beta_0)$, with $\beta_0 = 4\pi/(\sqrt{3}a)$. Figure 5.14 compares the calculated κ_{1D} and κ_{2D} values for square and hexagonal lattices as a function of fill factor. Both lattices achieve similar maximum 2D coupling strengths, but the presence of two strong 2D channels in the hexagonal lattice makes its overall 2D feedback more robust. This property can be useful in novel material systems for first demonstrations, where hole roughness, fabrication non-uniformities, or material defects may otherwise disrupt the delicate balance required for 2D oscillation.

Since the number of non-radiative modes in a square lattice is smaller than in a hexagonal lattice, it is easier to enhance the radiation constants of all non-radiative modes in the square lattice by breaking the lattice symmetry. For square lattices, increasing asymmetry from circular holes to equilateral triangular holes and finally right-angled isosceles triangular holes lifts the degeneracy of the A and B bands, resulting in a larger separation in radiation losses between them. This makes the square lattice more favorable for mode discrimination and single-mode operation as long as a strong enough 2D coupling can be obtained. Figures 5.15 and 5.16 illustrate this effect for square and hexagonal lattices, respectively. In both cases, the top row shows the Fourier coefficients for three hole shapes, circular cylinder, equilateral triangle, and right-angled isosceles triangle, representing increasing levels of asymmetry. The middle row shows the corresponding band structures, while the bottom row shows the calculated radiation losses. In the square lattice, introducing asymmetry breaks the degeneracy of the A and B modes, allowing one mode

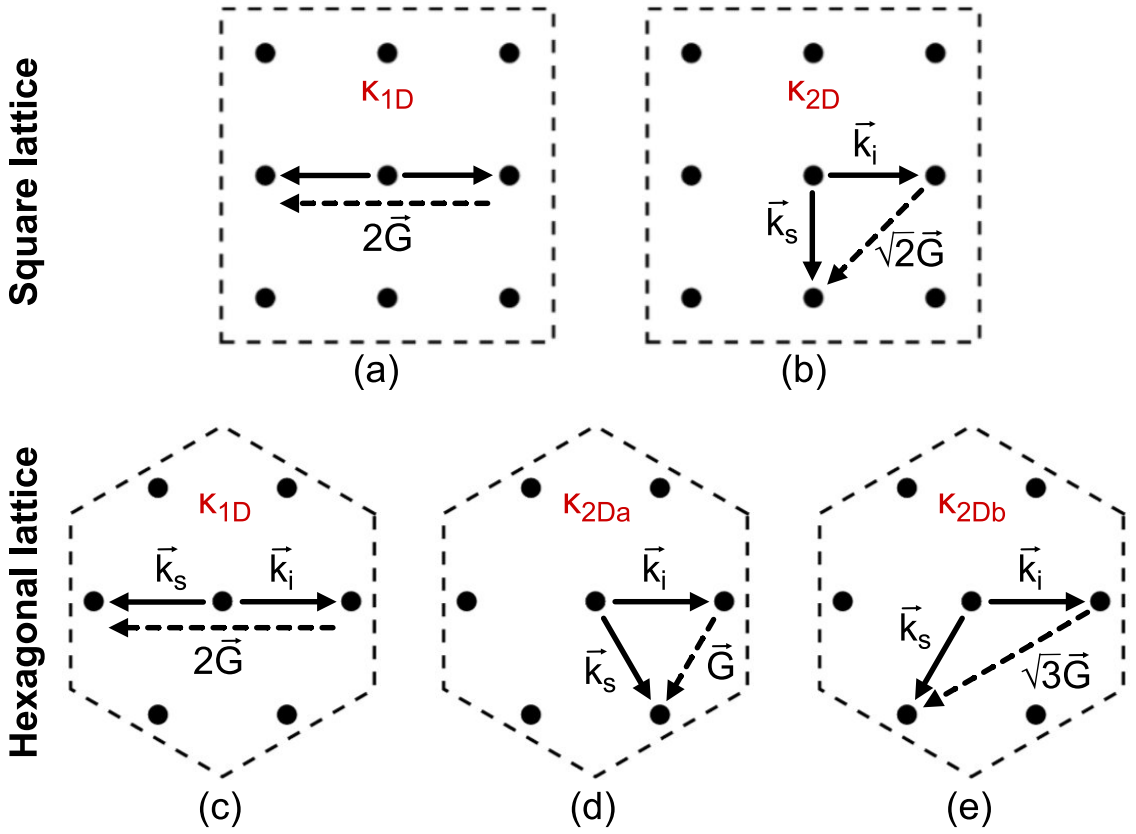

Figure 5.13: Coupling channels in square and hexagonal photonic crystal lattices. 1D coupling at 180° (a) and 2D coupling at 90° (b) for a square lattice. 1D coupling at 180° (c), and 2D coupling at60° (d) and 120° (e) for a hexagonal lattice.

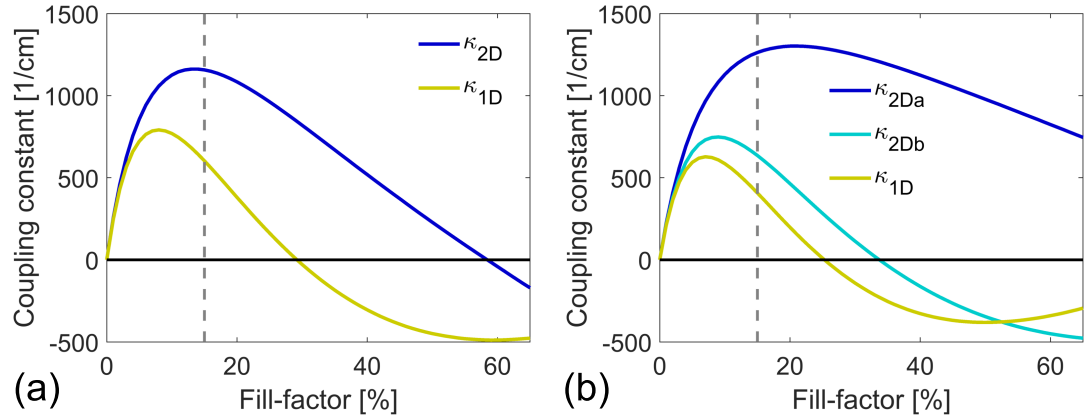

Figure 5.14: Coupling constants as a function of air-hole fill factor for circular holes. (a) Square lattice: 1D coupling at 180° (κ_{1D}) and 2D coupling at 90° (κ_{2D}). (b) Hexagonal lattice: 1D coupling at 180° (κ_{1D}), and 2D couplings at 60° (κ_{2Da}) and 120° (κ_{2Db}). The vertical dotted line indicates $FF = 15\%$.

to act as a low-loss lasing mode while pushing the others to higher losses. In contrast, in the hexagonal lattice, the higher symmetry ensures that the A, B_1, B_2, and C modes remain nearly degenerate even with asymmetric hole shapes, leading to vanishing radiation loss differences. Thus, square lattices are better suited for single-mode operation, whereas hexagonal lattices provide stronger intrinsic 2D feedback but less flexibility in selecting the lasing mode.

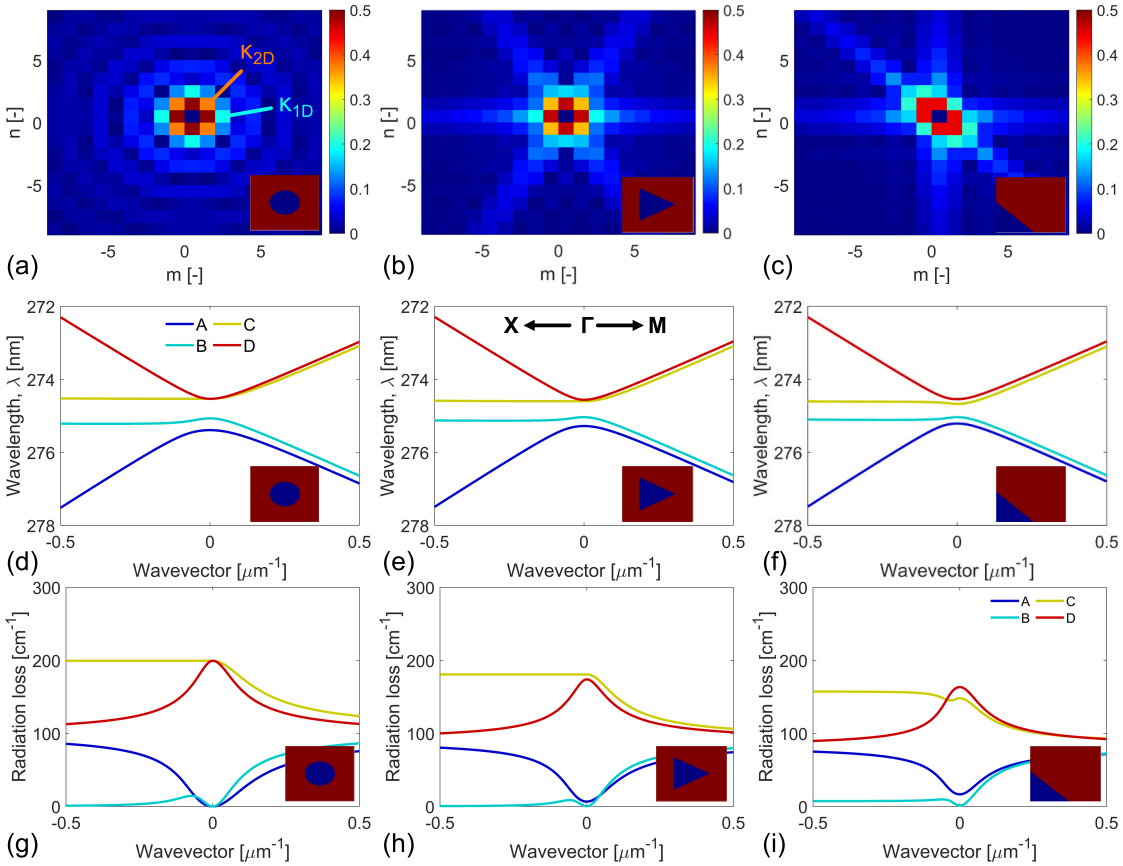

Figure 5.15: Square-lattice UVC PCSEL with fill factor $FF = 15\%$ and lattice constant $a = 118\,\text{nm}$ for three air-hole shapes: circular, equilateral triangular, and right-isosceles triangular, as indicated by the insets. (a–c) Coupling coefficients, shown versus reciprocal lattice indices m and n [209] (d–f) Bandstructures. (g–i) Radiation losses. $FF = 15\%$, $a = 118\,\text{nm}$, and $\Gamma_{PC} = 5.3\%$.

Recent work has also demonstrated that double-square-lattice PCSELs can overcome the symmetry limitations of single square lattices [39, 58]. By combining two square lattices with a small displacement, the degeneracy between the A and B bands can be lifted, while also enhancing the vertical radiation loss of the lowest-loss mode. This strategy enables both single-mode lasing and high output power, as the lasing mode maintains a loss margin relative to competing modes while still coupling efficiently to free space.

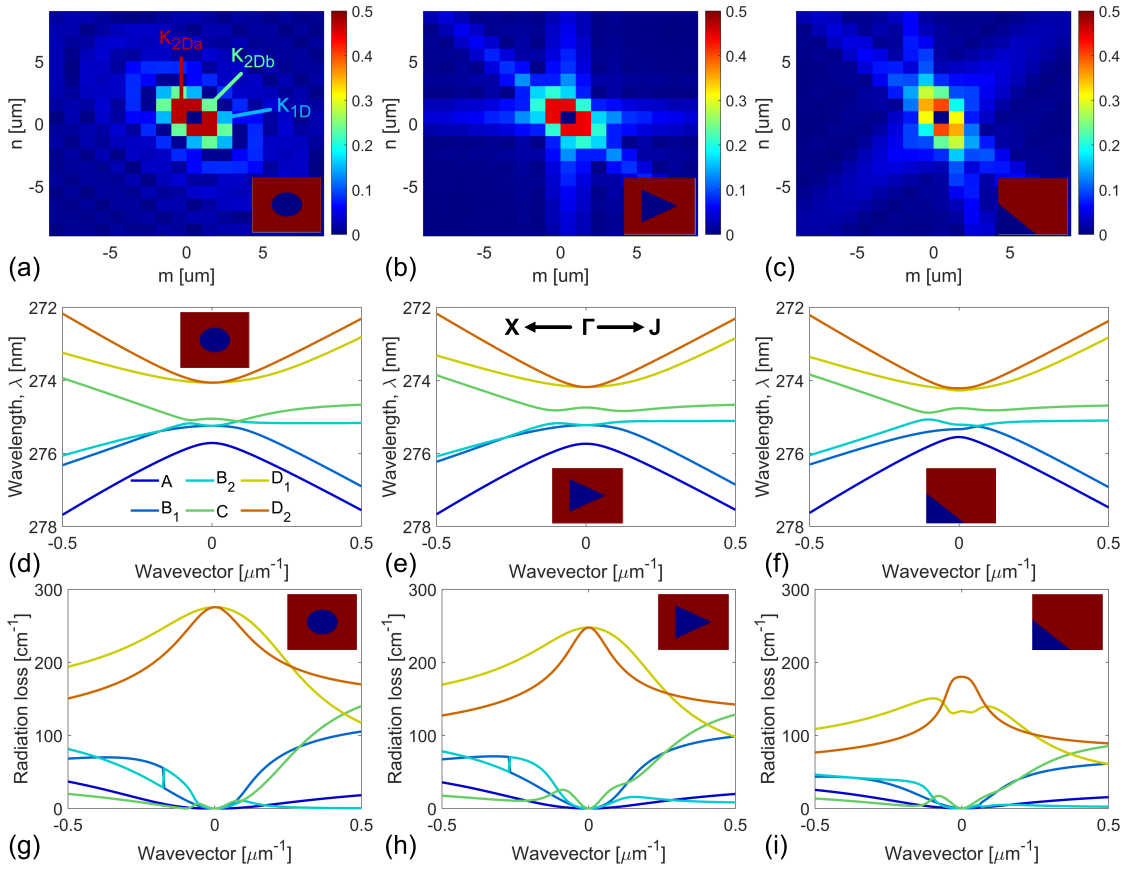

Figure 5.16: Hexagonal-lattice UVC PCSEL with fill factor $FF = 15\%$ and lattice constant $a = 136\,\text{nm}$ for three air-hole shapes: circular, equilateral triangular, and right-isosceles triangular, as indicated by the insets. (a–c) Coupling coefficients, shown versus reciprocal lattice indices m and n [210]. (d–f) Bandstructures. (g–i) Radiation losses. $FF = 15\%$, $a = 136\,\text{nm}$, and $\Gamma_{PC} = 5.3\%$.

5.8 k-space weighted loss estimation

The main drawback of finite-CWT, despite its efficiency, is that it relies on simplified assumptions in the underlying infinite-structure band model. This limits its accuracy when compared with more rigorous infinite-structure approaches such as GME or RCWA. To overcome this limitation, the k-space weighted loss estimation (kSWLE) method was developed together with Chemnitz University of Technology as a general framework for calculating vertical and lateral losses of finite-size PCSELs directly from their infinite-structure bandstructure. Because quantities such as dispersion, group velocity, and outcoupling strength are readily obtained from infinite-structure calculations, kSWLE provides a versatile bridge between band models and finite-size loss estimation.

5.8.1 kSWLE framework

The key physical idea behind kSWLE is that a finite device cannot sustain a perfectly sharp Γ-point mode. Truncation at the cavity boundary introduces diffraction, which broadens the optical field in reciprocal space. As a result, the lasing mode is no longer associated with a single Bloch state of the infinite photonic crystal, but instead occupies a distribution of in-plane wavevectors.

Finite-CWT simulations confirm that this k-space distribution is well described by a circularly symmetric Gaussian centered at the Γ-point, with a width inversely proportional to the device radius, $\sigma_k = \pi/(2L)$. An example is shown in Fig. 5.17, where the Fourier-transformed finite-CWT mode closely follows a Gaussian fit. This observation motivates the approximation used in kSWLE, where the in-plane field distribution of a finite mode is modeled as

$$I(\mathbf{k}) = \frac{1}{2\pi\sigma_k^2} \exp\Big(-\frac{|\mathbf{k}|^2}{2\sigma_k^2}\Big), \quad \sigma_k = \pi/(2L). \tag{5.26}$$

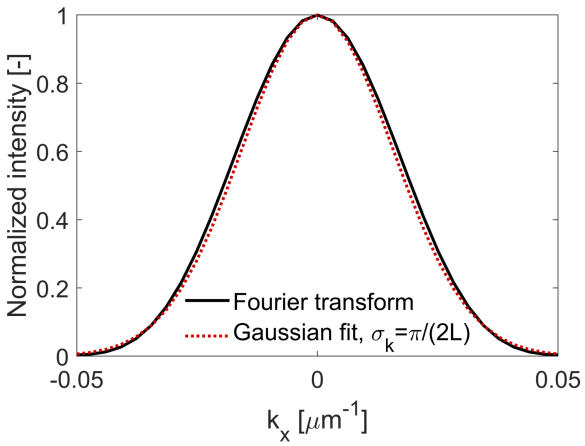

Figure 5.17: Fourier-transformed in-plane field profile of the finite-CWT B_1 mode (solid black) for a device radius of $L = 100\,\mu\text{m}$, compared with a Gaussian fit (dashed red) using $\sigma_k = \pi/(2L)$. The close agreement shows that the k-space distribution of the finite-size mode is well described by a Gaussian envelope, providing a simple and accurate choice for $I(\mathbf{k})$ in the kSWLE framework.

An example of a bandstructure is shown in Fig. 5.18, where the wavelength, vertical loss , and group velocity dispersions are plotted for the fundamental bands. These dispersions illustrate the physical basis of the kSWLE framework. Although the A, B_1, B_2, and C modes are non-radiative exactly at the Γ-point, they become radiative for finite in-plane wavevectors, meaning that their overall radiative losses differ depending on the detailed shape of the imaginary dispersion surface. Likewise, the real part of the dispersion is different for each band, and its slope determines the group velocity that governs lateral leakage. Consequently, even modes that are symmetry-protected at $k = 0$

acquire different effective losses once the Gaussian distribution strays away from Γ.

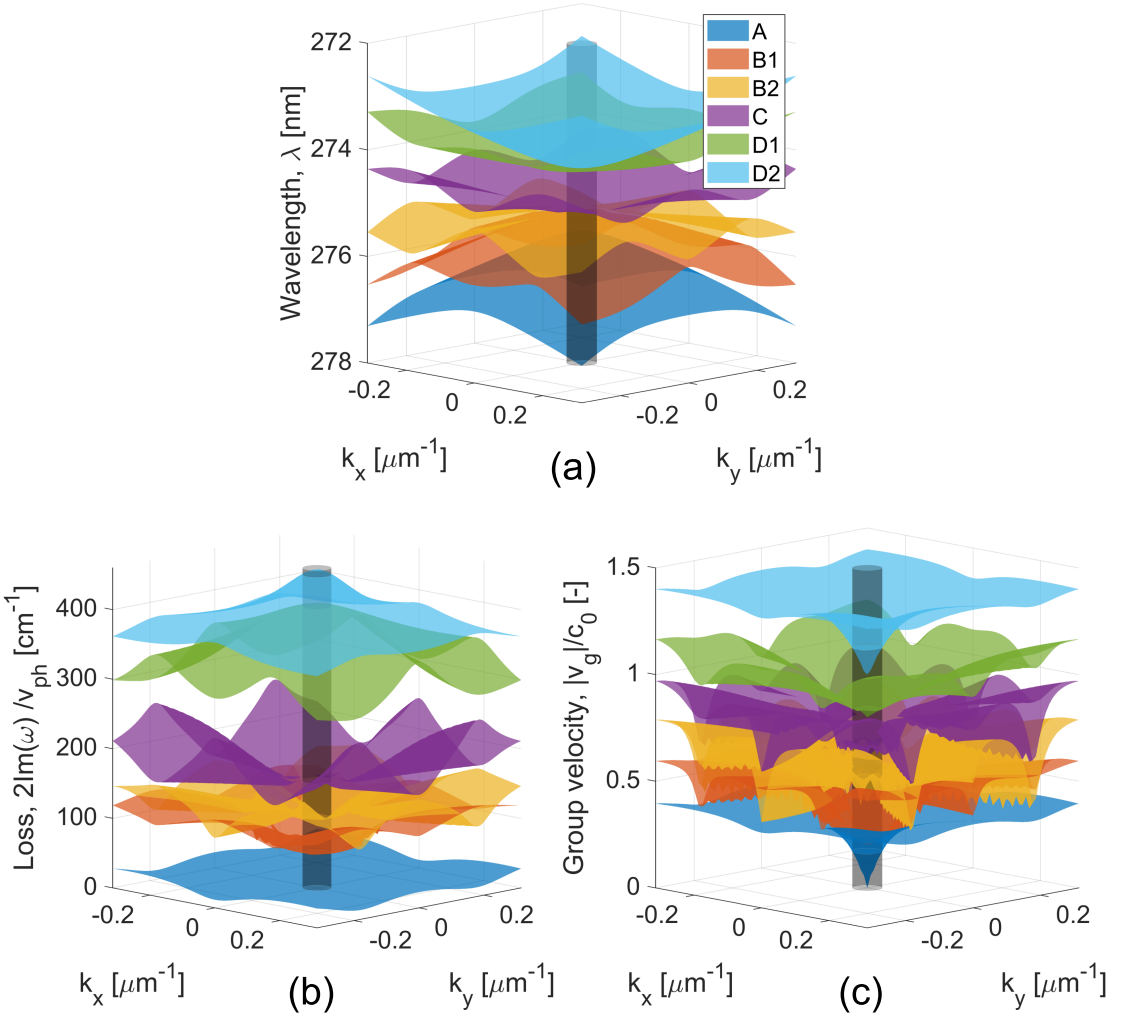

Figure 5.18: 2D infinite PCSEL bandstructure for a hexagonal lattice with circular air holes, calculated using 3D-CWT. The plots show (a) wavelength dispersion, (b) vertical loss dispersion, and (c) normalised group velocity dispersion for the fundamental bands. The dark cylinder indicates the reciprocal-space region, $\sigma_k = \pi/(2L)$, corresponding to a device radius of $L = 50\,\mu\text{m}$, which provides the dominant contribution to the finite-size losses in Eqs. (5.27) and (5.28). In (b), the losses of each band are offset by $50\,\text{cm}^{-1}$ relative to the band below for clarity, while in (c) the group velocities of each band are offset by $0.2|v_{gr}|/c_0$. $FF = 15\%$, $a = 136\,\text{nm}$, and $\Gamma_{PC} = 5.3\%$.

With this picture in mind, the finite-size losses can be expressed as Gaussian-weighted averages over the bandstructure quantities. The vertical loss is obtained from the imaginary part of the frequency, $\text{Im}[\omega(\mathbf{k})]$, which quantifies outcoupling into radiation modes. The lateral loss, is associated with energy transport out of the device boundary and is proportional to the

group velocity $|\nabla_k \omega(\mathbf{k})|$. Both quantities are readily available from infinite photonic crystal bandstructure calculations, whether obtained by CWT, GME, or other methods. By integrating the bandstructure properties over the Gaussian distribution, one obtains

$$\alpha_{\text{vert}} = \frac{1}{v_{ph}} \int I(\mathbf{k}) 2\text{Im}[\omega(\mathbf{k})] dk_x dk_y, \tag{5.27}$$

$$\alpha_{\text{lat}} = \frac{1}{v_{ph}} \int I(\mathbf{k}) \frac{|\nabla_k \omega(\mathbf{k})|}{2L} dk_x dk_y, \tag{5.28}$$

where $v_{ph} = c_0/n_{eff}$ is the phase velocity of the guided mode. The denominator of α_{lat} contains a factor of $2L$, corresponding to the characteristic escape length across the device. This choice affects only the absolute magnitude of the lateral loss but not its scaling with radius, as shown in Section 5.8.2. The total modal loss is simply the sum,

$$\alpha_{tot} = \alpha_{vert} + \alpha_{lat}. \tag{5.29}$$

The resulting loss behavior is illustrated in Fig. 5.19, which shows the calculated total, lateral, and vertical losses as a function of device diameter for the six different modes $A - D_2$. All losses decrease with increasing radius, except for the D radiation loss, reflecting the narrowing of the k-space envelope and the reduced overlap with lossy states.

These results also highlight a key distinction between finite-CWT and kSWLE. In finite-CWT, the bands B_1/B_2 and D_1/D_2 remain degenerate at Γ and are predicted to have identical losses. In contrast, kSWLE explicitly accounts for the dispersion near the Γ-point, which lifts this degeneracy and predicts distinct radiative and lateral losses for these modes.

5.8.2 Scaling laws

As discussed in the previous subsection, the finite-size mode can be described as a Gaussian envelope in reciprocal space, whose width narrows as the device radius increases. In the large-radius limit, this narrowing ensures that the mode is strongly localized near the Γ-point, where the band dispersion can be approximated by a parabolic expansion

$$\text{Re}[\omega(\mathbf{k})] \approx \omega_0 + \frac{b}{2}k^2, \quad \text{Im}[\omega(\mathbf{k})] \approx \gamma_0 + \frac{l}{2}k^2, \tag{5.30}$$

where $k = |\mathbf{k}|$. Here, b describes the curvature of the real part of the dispersion, while l characterizes the curvature of the imaginary part, which governs the vertical loss rate. The constant γ_0 represents the loss at the Γ-point: it vanishes for non-radiative bands such as $A - C$, but is finite for radiative D modes.

Using these parabolic forms together with the Gaussian distribution $I(\mathbf{k})$, the integrals in Eqs. (5.27) and (5.28) can be evaluated analytically. This leads to closed-form scaling laws for the two main contributions to the modal loss

$$\alpha_{lat} \propto bL^{-2}, \quad \alpha_{vert} \propto lL^{-2}. \tag{5.31}$$

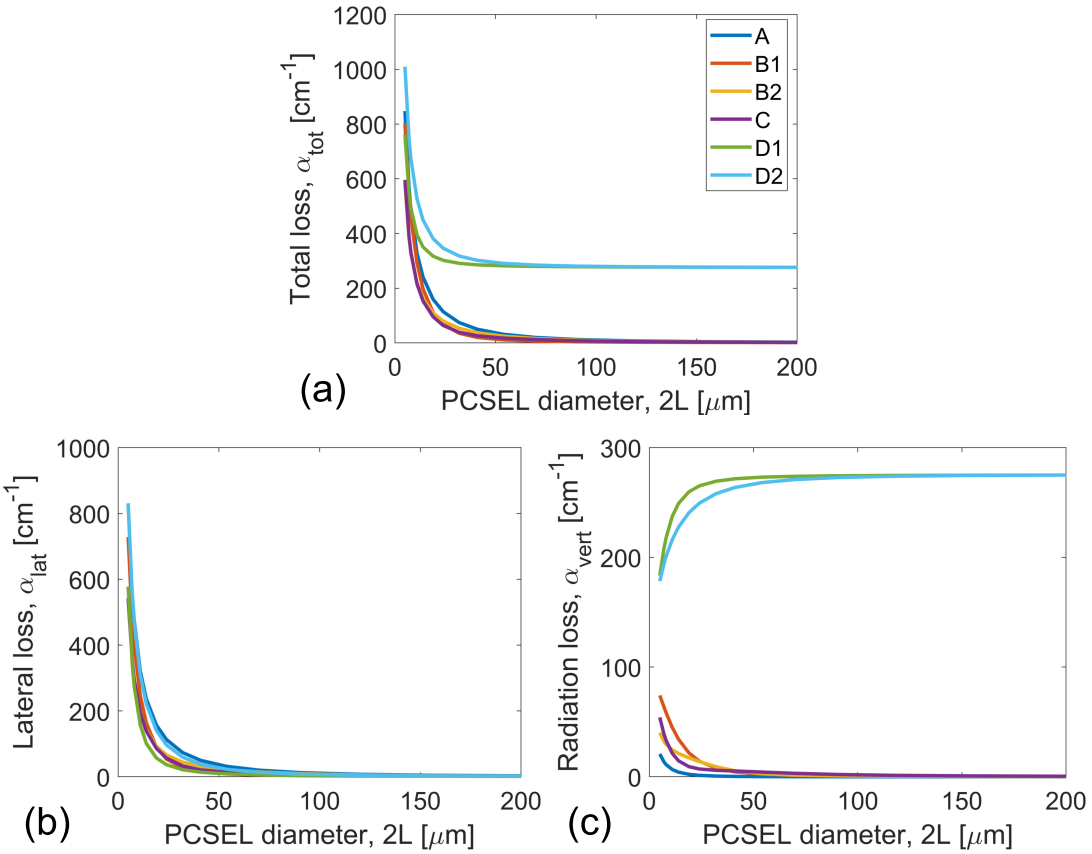

Figure 5.19: An example of finite-size losses using the kSWLE method. The plots show (a) total modal losses, (b) lateral losses, and (c) radiation (vertical) losses as a function of PCSEL diameter for the fundamental bands. $FF = 15\%$, $a = 136\,\text{nm}$, and $\Gamma_{PC} = 5.3\%$.

The physical origin of this L^{-2} behavior can be understood from the narrowing of the Gaussian envelope in reciprocal space as the device radius increases. Since its width scales as $\sigma_k \sim 1/L$, the relevant region of the bandstructure shrinks towards the Γ-point. For lateral losses, the group velocity varies linearly in k, giving $|\nabla_k \omega(\mathbf{k})| \sim 1/L$, which when combined with the escape length $2L$ in the denominator of Eq. (5.28) leads to $\alpha_{lat} \propto 1/L^2$. For vertical losses, the imaginary part of the frequency grows quadratically with k, i.e. $\text{Im}[\omega(\mathbf{k})] \sim k^2 \sim 1/L^2$, producing the same scaling. While the prefactors depend on the band curvature parameters b and l, the L^{-2} dependence itself is independent of such details, at least until other effects such as material absorption or disorder-induced scattering begin to dominate.

Chapter 6

Summary and outlook

This thesis has addressed thermal and optical effects in III-nitride surface-emitting lasers. By combining experimental characterization, device-level modeling, and theoretical development, the work has aimed to clarify many of the key challenges facing these devices and to identify opportunities for future improvement.

One area facing many challenges is the development of electrically injected UVB and UVC VCSELs. So far, only optically pumped VCSELs emitting in the UVB and UVC have been demonstrated, showing that achieving high-reflectivity mirrors, high-quality cavities, and accurate cavity length control in the UV is now possible. However, electrically injected UV VCSELs remain an elusive goal. Key issues include achieving a conductive and transparent p-side for efficient current spreading, together with robust electrical and optical confinement schemes. An often overlooked but equally critical challenge is the poor thermal conductivity of Al-rich AlGaN, which we show in Paper B will become a bottleneck for CW operation. This thesis has demonstrated strategies for reducing thermal resistance, which will be essential in the development of future electrically injected UV devices. Chapter 4.2 and Paper B presented simulations showing how cavity length, mirror design, and contact placement affect the thermal resistance of blue and UV VCSELs. In Chapter 4.3 and Paper A, we developed design concepts for achieving an athermalized emission wavelength in VCSELs using a hard-mirror equivalent cavity model, and we experimentally demonstrated this approach in an optically pumped UVB VCSEL with strongly reduced temperature sensitivity of the lasing wavelength. Together, these contributions show both how thermal resistance can be mitigated by design, and how its impact on wavelength stability can be counteracted.

For blue VCSELs, recent demonstrations of high-efficiency devices indicate that these devices are approaching commercialization. Remaining challenges include scaling to larger apertures while maintaining single-mode operation and optimizing current confinement schemes. It is still not clear which mirror con-

figuration, hybrid or all-dielectric, will ultimately prove most advantageous, as both approaches show promising results [28, 150]. Likewise, the optimal aperture design is still unclear: shallow etches provide both lateral guiding and confinement [140] but may struggle at high current densities, while combined etched–dielectric schemes offer stronger electrical confinement [109] but introduce fabrication challenges related to alignment. Continued progress in these areas will determine how rapidly blue VCSELs can penetrate applications such as high-resolution displays, augmented reality, and underwater optical communication. In this context, the work presented in Chapter 4.4 addressed how to obtain sigle-mode operation in blue VCSELs. Two different approaches were explored, based on surface-relief structuring and sub-wavelength gratings, demonstrating that transverse mode and polarization control is possible using such structures. This demonstrates that relatively simple-to-implement fabrication schemes can provide an effective path toward high-performance, single-mode blue VCSELs.

PCSELs provide a complementary route to high-power surface-emitting lasers with excellent beam quality, but extending them into the ultraviolet remains highly challenging. To date, the only demonstration in the UVC rely on optical pumping [45], and key issues such as electrical injection, thermal management, and mode control remain unresolved. These difficulties are exacerbated by the smaller lattice constant at short wavelengths, which imposes tight fabrication constraints. In the UVC, hexagonal lattices are typically preferred because they permit larger lattice spacing and are therefore easier to fabricate, while also making it easier to achieve sufficiently strong two-dimensional coupling. However, their high symmetry makes it very challenging to introduce controlled asymmetries for robust single-mode operation. In parallel, efficient electrical injection remains an open issue due to the poor conductivity of Al-rich AlGaN, calling for novel current-spreading concepts, such as distributed polarization doping [33, 34]. In addition, lateral current spreading poses a further challenge, and is even more demanding in PCSELs than in EELs, since the current must be distributed over much larger areas. At the same time, finite-size effects grow increasingly important in the UVC, since smaller device dimensions and higher intrinsic losses strongly influence threshold and mode competition. The methods developed in Chapter 5, including 3D-CWT and the kSWLE framework, provide powerful tools to quantify these effects, offering guidance for the design of practical UV PCSELs. If such strategies can be realized, UV PCSELs could emerge as compact, efficient sources for photolithography, disinfection and sterilization applications, including water purification, air treatment in ventilation systems, and surface sterilization of medical equipment.

Chapter 7

Summary of papers

Paper A

Athermalization of the lasing wavelength in vertical-cavity surface-emitting lasers

Laser & Photonics Reviews, 17, 2300009, 2023.

A concept for vertical-cavity surface-emitting lasers (VCSELs) is proposed and demonstrated to obtain a lasing wavelength with unprecedented temperature stability. The concept is based on incorporating a dielectric material with a negative thermo-optic coefficient, $\mathrm{d}n/\mathrm{d}T$, in the distributed Bragg reflectors (DBRs) to compensate the positive $\mathrm{d}n/\mathrm{d}T$ of the semiconductor cavity. In a short cavity, the optical field has a significant overlap with the DBRs, and the redshift of the lasing wavelength caused by the semiconductor cavity can be compensated by the negative $\mathrm{d}n/\mathrm{d}T$ of the DBRs. Here, proof of this concept is presented for optically-pumped VCSELs emitting at 310 nm, demonstrating a lasing wavelength that even blueshifts by less than 0.1 nm over an 80 °C range with a maximum slope of $-3.4\,\mathrm{pm\,K^{-1}}$. This is to be compared with a redshift of 1–1.5 nm over the same temperature range reported for III-nitride blue-emitting VCSELs. Furthermore, this method can also be implemented in VCSELs with longer cavity lengths by including a dielectric layer between the semiconductor and the DBR. The approach used here to obtain a temperature-stable lasing wavelength is generic and can therefore be applied to VCSELs in all material systems and lasing wavelengths.

My contributions: I carried out the analytical modeling, effective-index simulations, optical and temperature-dependent photoluminescence measurements, and calculations of the carrier-induced refractive index change. I also wrote the manuscript and Supplementary Information with input from the co-authors.

Paper B

Improving thermal resistance in III-nitride blue and UV vertical-cavity surface-emitting lasers

Optics Express, 33, 34242–34254, 2025.

Different mirror concepts are being explored in parallel for III-N vertical-cavity surface-emitting lasers (VCSELs), each with their own pros and cons. A general belief is that epitaxial distributed Bragg reflectors (DBRs) offer a VCSEL with superior thermal performance compared to all-dielectric DBRs. We here show that this is not the case for GaN-based VCSELs designed for 440 nm emission with cavity lengths $\geq 10\lambda$ due to a laterally dominated heat flow caused by the high thermal conductivity of GaN cavity material in contrast to the lower thermally conductive DBRs. If the same cavity design that is used for blue GaN VCSELs is applied to ultraviolet-C (UVC) AlGaN-VCSELs this will lead to detrimentally high internal temperatures (up to 370 °C) due to the very low thermal conductivity of AlGaN which would prevent lasing. Increasing the cavity length to 30λ reduces the thermal resistance from 4400 K/W to 2600 K/W, but this is not enough. To drastically lower the internal temperature, we propose adding 300 nm AlN spacer layers to the AlGaN cavity, which reduces thermal resistance to 1100 K/W, which is similar to that of blue VCSELs. The low thermal resistance of this design shows promise for realizing electrically injected, continuous-wave AlGaN-based UVC VCSELs.

My contributions: I carried out all thermal modeling, simulations, and data analysis. I wrote the original draft of the paper and Supplementary Information, and edited them based on feedback from the co-authors.

Paper C

Finite-size effects in photonic-crystal surface-emitting lasers – critical discussion of different approximations

Submitted to Optics Express, 2025.

We present a comparative study of vertical and lateral loss estimation in photonic-crystal surface-emitting lasers (PCSELs), focusing on how finite-size effects are influenced by the choice of an infinite-structure band model. Finite coupled-wave theory (finite-CWT) provides accurate simulations for realistically sized devices but relies on the simplified infinite-CWT model. To complement this, we introduce k-space weighted loss estimation (kSWLE), a framework that estimates outcoupling and in-plane leakage using arbitrary infinite bandstructure models and allows deriving analytical expressions for the scaling behavior in the limit of large-sized PCSELs. We apply kSWLE with both CWT and guided-mode expansion (GME) models and show that the underlying bandstructure significantly affects predicted losses and spectral characteristics. In regimes where the lasing mode is dominated by a single band, kSWLE reproduces similar scaling trends as finite-CWT. However, for small devices or at specific fill factors, broader spectral distributions lead to ambiguous mode classification and limit the applicability of both methods. The results highlight the strengths and limitations of different bandstructure models and establish kSWLE as a practical tool for evaluating size-dependent loss mechanisms in PCSELs.

My contributions: I implemented the 3D finite-CWT method and performed the finite-size simulations. The mode decomposition and the development of the kSWLE framework were carried out together with the co-authors, and Moritz Riedel performed the GME simulations. I also wrote the manuscript and Supplementary Information with input from the co-authors.

Chapter 8

Appendices

Appendix A - for pulsed heating at infinity

The change in thermal energy stored in the system (VCSEL) is governed by the balance between input heating power $P(t)$ and the rate of heat dissipation. The thermal energy is related to the average temperature as

$$Q(t) = \rho c_p V T(t), \tag{8.1}$$

where ρ is the material density, c_p is the specific heat capacity, V is the volume of the region, and $T(t)$ is the average temperature. Differentiating and equating with net heat input yields

$$\frac{\mathrm{d}Q}{\mathrm{d}t} = P(t) - \dot{Q}_{loss}(t). \tag{8.2}$$

To model thermal loss, we use the definition of the thermal resistance, assuming

$$\dot{Q}_{loss}(t) = \frac{T(t) - T_{amb}}{R_{th}}, \tag{8.3}$$

leading to the full ODE

$$\rho c_p V \frac{\mathrm{d}T}{\mathrm{d}t} = P(t) - \frac{T(t) - T_{amb}}{R_{th}}. \tag{8.4}$$

This equation has an analytical solution when $P(t) = P_0$ is a constant

$$T(t) = T_{amb} + P_0 R_{th}\Big[1 - \exp(-t/\tau)\Big]. \tag{8.5}$$

with time constant

$$\tau = R_{th} C_{th} = R_{th} \rho c_p V, \tag{8.6}$$

where $C_{th} = \rho c_p V$ is the thermal capacitance, which quantifies the amount of heat required to change the temperature by a certain amount, and R_{th}

represents the difficulty of heat flowing out of the system. Together, these parameters determine the rate at which the system responds to heating and cooling. During the off-phase (e.g., between pulses), when $P(t) = 0$, the cooling behavior is

$$T(t) = T_{amb} + (T_0 - T_{amb}) \exp(-t/\tau), \tag{8.7}$$

where T_0 is the device temperature at the start of the cooling phase. This model captures the essential heating and cooling dynamics under pulsed conditions and enables insight into the characteristic response time of the structure.

The on-pulse is defined as $t_{on} = a\tau$, and the off-pulse as $t_{off} = b\tau$, and the duty cycle can be expressed as

$$D = \frac{t_{on}}{t_{on} + t_{off}} = \frac{a}{a + b} \tag{8.8}$$

Recurrence relation

It is possible to derive the minimum and maximum temperature after an infinite amount of heating and cooling cycles analytically using a recurrence relation. If T_n is the temperature at the start of the n-th cycle, just before heating starts, $T_{n,on}$ is the temperature at the end of the on-phase, and $T_{n+1} = T_{n,off}$ is the temperature after the off-phase (i.e. the start of the next cycle), then during the on-time ($t_{on} = a\tau$) we have

$$T_{n,on} = T_n + R_{th} P_0 \Big[1 - \exp(-a)\Big]. \tag{8.9}$$

During the off-time ($t_{off} = b\tau$), the system cools exponentially

$$T_{n+1} = T_{amb} + (T_{n,on} - T_{amb}) \exp(-b). \tag{8.10}$$

If we choose to express everything relative to the ambient temperature T_{amb}

$$\Delta T_n = T_n - T_{amb}, \tag{8.11}$$

the recurrence relation becomes

$$\Delta T_{n+1} = \Big(\Delta T_n + R_{th} P_0 \big[1 - \exp(-a)\big]\Big) \exp(-b) = r \Delta T_n + Ar, \tag{8.12}$$

where $A = R_{th} P_0 (1 - \exp(-a))$ and $r = \exp(-b)$, so that $0 < r < 1$ is introduced for convenience. This captures the cumulative heating: each cycle adds a fixed amount of heat during the on-pulse, and then some fraction of it decays during the off-time. This is a first-order linear inhomogeneous recurrence relation the solution and has a standard solution

$$\Delta T_n = C r^n + T_p \tag{8.13}$$

where the first term on the righ-hand-side is the homogenoeus solution, and the second term the particular solution. To find the particular solution, we assume a constant solution $\Delta T_{n+1} = \Delta T_n = T_p$

$$T_p = rT_p + Ar \rightarrow T_p = \frac{Ar}{1-r} = \frac{R_{th}P_0\Big[1-\exp(-a)\Big]}{1-\exp(-b)}. \tag{8.14}$$

For the homogeneous solution we have

$$\Delta T_{n+1} = r\Delta T_n \rightarrow \Delta T_n^h = Cr^n. \tag{8.15}$$

Now we apply the initial condition (device temperature is equal to the ambient temperature before pulsed operation) $\Delta T(t=0) = 0$

$$0 = Cr^0 + T_p \rightarrow C = -T_p. \tag{8.16}$$

The full solution becomes

$$\Delta T_n = T_p(1-r^n) = \frac{R_{th}P_0\Big[1-\exp(-a)\Big]}{1-\exp(-b)}\Big[1-\exp(-bn)\Big]. \tag{8.17}$$

After an infinite amount of on and off cycles, the temperature rise at the end of the off-pulse becomes

$$\Delta T_{off}^{\infty} = \lim_{n\to\infty}\Delta T_n = \frac{R_{th}P_0\Big[1-\exp(-a)\Big]}{1-\exp(-b)}. \tag{8.18}$$

At the end of the following on-cycle, the temperature becomes

$$\Delta T_{on}^{\infty} = \Delta T_{off}^{\infty} + R_{th}P_0\Big[1-\exp(-a)\Big] = R_{th}P_0\Big[1-\exp(-a)\Big]\frac{2-\exp(-b)}{1-\exp(-b)}. \tag{8.19}$$

The analytical expressions derived above describe the steady-state minimum and maximum temperatures under periodic pulsed heating using a lumped thermal model. In this model, heat accumulation and dissipation are treated as exponential processes governed by a single thermal time constant τ. Interestingly, even when the off-time $t_{off} \gg \tau$, the model predicts a nonzero residual temperature rise after each cooling phase. This is because, under the exponential decay assumption, no finite cooling period fully removes the injected heat, a small fraction always remains. Over an infinite number of pulses, these residual contributions accumulate and converge to a steady-state minimum temperature. While this behavior is mathematically consistent with the lumped model, it slightly overestimates cumulative heating in the regime where the off-time is much longer than the heating time and thermal response time.

References

[1] A. L. Schawlow and C. H. Townes, "Infrared and optical masers," *Physical Review*, vol. 112, no. 6, pp. 1940–1949, 1958.

[2] T. H. Maiman, "Stimulated optical radiation in ruby," *Nature*, vol. 187, no. 4736, pp. 493–494, 1960.

[3] "Introduction and overview," in *Understanding Lasers*. John Wiley & Sons, Ltd, 2018, pp. 1–20, section: 1 _eprint: https://onlinelibrary.wiley.com/doi/pdf/10.1002/9781119310693.ch1.

[4] Y. Développement, "VCSELs-Market and technology trends 2020," *Lyon-Villeurbanne, France, Tech. Rep*, 2020.

[5] H. Soda, K.-i. Iga, C. Kitahara, and Y. Suematsu, "GaInAsP/InP surface emitting injection lasers," *Japanese Journal of Applied Physics*, vol. 18, no. 12, p. 2329, 1979.

[6] J. A. Tatum, A. Clark, J. K. Guenter, R. A. H. Iii, and R. H. Johnson, "Commercialization of Honeywell's VCSEL technology," in *Vertical-Cavity Surface-Emitting Lasers IV*, vol. 3946. SPIE, 2000, pp. 2–13.

[7] K. Iga, "Forty years of vertical-cavity surface-emitting laser: Invention and innovation," *Japanese Journal of Applied Physics*, vol. 57, no. 8S2, p. 08PA01, 2018.

[8] K. J. Ebeling, R. Michalzik, and H. Moench, "Vertical-cavity surface-emitting laser technology applications with focus on sensors and three-dimensional imaging," *Japanese Journal of Applied Physics*, vol. 57, no. 8S2, p. 08PA02, 2018.

[9] R. Michalzik, "VCSEL Fundamentals," in *VCSELs: Fundamentals, Technology and Applications of Vertical-Cavity Surface-Emitting Lasers*, R. Michalzik, Ed. Berlin, Heidelberg: Springer, 2013, pp. 19–75.

[10] H. P. Maruska and J. J. Tietjen, "The preparation and properties of vapor-deposited single-crystalline GaN," *Applied Physics Letters*, vol. 15, no. 10, pp. 327–329, 1969.

[11] J. Pankove, E. Miller, and J. Berkeyheiser, "GaN electroluminescent diodes," in *1971 International Electron Devices Meeting*, 1971, pp. 78–78.

[12] H. Maruska, D. Stevenson, and J. Pankove, "Violet luminescence of Mg-doped GaN," *Applied Physics Letters*, vol. 22, no. 6, pp. 303–305, 1973.

[13] B. G. Levi, "Nobel prize in physics recognizes research leading to high-brightness blue LEDs," *Physics Today*, vol. 67, no. 12, pp. 14–17, 2014.

[14] Z. Sun, P. Zhang, W. Liu, and W. He, "Nobel prizes and materials science," in *Fundamentals of Materials Science: From Basic Theories to Critical Properties*, Z. Sun, P. Zhang, W. Liu, and W. He, Eds. Singapore: Springer Nature, 2025, pp. 609–640.

[15] H. Amano, N. Sawaki, I. Akasaki, and Y. Toyoda, "Metalorganic vapor phase epitaxial growth of a high quality GaN film using an AlN buffer layer," *Applied Physics Letters*, vol. 48, no. 5, pp. 353–355, 1986.

[16] H. Amano, K. Masahiro, H. Kazumasa, and A. Isamu, "P-type conduction in Mg-doped GaN treated with low-energy electron beam irradiation (LEEBI)," *Japanese Journal of Applied Physics*, vol. 28, no. 12A, p. L2112, 1989.

[17] S. Nakamura, N. Iwasa, M. S. M. Senoh, and T. M. T. Mukai, "Hole compensation mechanism of p-type GaN films," *Japanese Journal of Applied Physics*, vol. 31, no. 5R, p. 1258, 1992.

[18] S. Nakamura, T. Mukai, M. Senoh, and N. Iwasa, "Thermal annealing effects on p-type Mg-doped GaN films," *Japanese Journal of Applied Physics*, vol. 31, no. 28, pp. L139–L142, 1992.

[19] S. Nakamura, T. M. T. Mukai, and M. S. M. Senoh, "High-power GaN p-n junction blue light-emitting diodes," *Japanese Journal of Applied Physics*, vol. 30, no. 12A, p. L1998, 1991.

[20] S. Nakamura, T. Mukai, and M. Senoh, "Candela-class high-brightness InGaN/AlGaN double-heterostructure blue-light-emitting diodes," *Applied Physics Letters*, vol. 64, no. 13, pp. 1687–1689, 1994.

[21] S. Nakamura, M. Senoh, N. Iwasa, and S.-i. N. S.-i. Nagahama, "High-brightness InGaN blue, green and yellow light-emitting diodes with quantum well structures," *Japanese Journal of Applied Physics*, vol. 34, no. 7A, p. L797, 1995.

[22] S. Nakamura, M. Senoh, S.-i. Nagahama, N. Iwasa, T. Yamada, T. Matsushita, H. K. H. Kiyoku, and Y. S. Y. Sugimoto, "InGaN multi-quantum-well-structure laser diodes with cleaved mirror cavity facets," *Japanese Journal of Applied Physics*, vol. 35, no. 2B, p. L217, 1996.

[23] S. Nakamura, M. Senoh, S.-i. Nagahama, N. Iwasa, T. Yamada, T. Matsushita, H. K. H. Kiyoku, and Y. S. Y. Sugimoto, "InGaN-based multi-quantum-well-structure laser diodes," *Japanese Journal of Applied Physics*, vol. 35, no. 1B, p. L74, 1996.

[24] S. Nakamura, M. Senoh, S. Nagahama, N. Iwasa, T. Yamada, T. Matsushita, Y. Sugimoto, and H. Kiyoku, "Room-temperature continuous-wave operation of InGaN multi-quantum-well structure laser diodes," *Applied Physics Letters*, vol. 69, no. 26, pp. 4056–4058, 1996.

[25] T.-C. Lu, J.-T. Chu, S.-W. Chen, B.-S. Cheng, H.-C. Kuo, and S.-C. Wang, "Lasing behavior, gain property, and strong coupling effects in GaN-based vertical-cavity surface-emitting lasers," *Japanese Journal of Applied Physics*, vol. 47, no. 8S1, p. 6655, 2008.

[26] Y. Higuchi, K. Omae, H. Matsumura, and T. Mukai, "Room-temperature CW lasing of a GaN-based vertical-cavity surface-emitting laser by current injection," *Applied Physics Express*, vol. 1, no. 12, p. 121102, 2008.

[27] T. Makino, M. Ito, K. Hayashi, M. Ohara, H. Miyahara, K. Sato, Y. Nakamura, T. Watanabe, Y. Kikuchi, T. Jyokawa, Y. Hoshina, E. Nakayama, R. Koda, N. Futagawa, and T. Hamaguchi, "Highly efficient and three-modes controlled GaN-based VCSELs with a long cavity and a curved mirror structure." Hawai'i, USA, 2024.

[28] N. Shibahara, T. Nishikawa, R. Watanabe, M. Yanagawa, S. Arakawa, A. Tokushi, T. Kitamura, S. Kamiyama, M. Iwaya, and T. Takeuchi, "In-plane distribution and high wall-plug efficiency of GaN-based vertical-cavity surface-emitting lasers," in *International Conference on Nitride Semiconductors (ICNS)*, Malmö, Sweden, 2025, oD-Mon-2*.

[29] T. Takeuchi, "Developments and prospects of GaN-based VCSELs," in *International Conference on Nitride Semiconductors (ICNS)*, Malmö, Sweden, 2025.

[30] F. Hjort, J. Enslin, M. Cobet, M. A. Bergmann, J. Gustavsson, T. Kolbe, A. Knauer, F. Nippert, I. Häusler, M. R. Wagner, T. Wernicke, M. Kneissl, and Å. Haglund, "A 310 nm optically pumped AlGaN vertical-cavity surface-emitting laser," *ACS Photonics*, vol. 8, no. 1.

[31] Z. Zheng, Y. Mei, H. Long, J. Hoo, S. Guo, Q. Li, L. Ying, Z. Zheng, and B. Zhang, "Algan-based deep ultraviolet vertical-cavity surface-emitting laser," *IEEE Electron Device Letters*, vol. 42, no. 3, pp. 375–378, 2021.

[32] E. Torres, J. Ciers, M. A. Bergmann, J. Hröpfner, S. Graupeter, M. Grigoletto, M. Guttmann, T. Kolbe, T. Wernicke, M. Kneissl, and Å. Haglund, "Ultraviolet-b resonant-cavity light-emitting diodes with tunnel junctions and dielectric mirrors," *ACS Photonics*, vol. 11, no. 8.

[33] T. Saito, R. Miyake, R. Yamada, Y. Imoto, S. Maruyama, Y. Sasaki, S. Karino, S. Iwayama, H. Miyake, K. Naniwae, S. Kamiyama, T. Takeuchi, and M. Iwaya, "Enhancing the carrier injection efficiency in AlGaN-based UV-b laser diodes," *physica status solidi (a)*, vol. n/a, no. n/a, p. 2500100, _eprint: https://onlinelibrary.wiley.com/doi/pdf/10.1002/pssa.202500100.

[34] T. Saito, R. Miyake, R. Yamada, Y. Imoto, S. Maruyama, Y. Sasaki, S. Karino, S. Iwayama, H. Miyake, K. Naniwae, S. Kamiyama, T. Takeuchi, and M. Iwaya, "Impact of growth temperature on heterostructure interface steepness in ultraviolet-B AlGaN-based laser diodes," *Applied Physics Letters*, vol. 126, no. 8, p. 082102, 2025.

[35] K. Sato, S. Yasue, K. Yamada, S. Tanaka, T. Omori, S. Ishizuka, S. Teramura, Y. Ogino, S. Iwayama, H. Miyake, M. Iwaya, T. Takeuchi, S. Kamiyama, and I. Akasaki, "Room-temperature operation of AlGaN ultraviolet-B laser diode at 298 nm on lattice-relaxed $Al_{0.6}$ $Ga_{0.4}$ N/AlN/sapphire," *Applied Physics Express*, vol. 13, no. 3, p. 031004, 2020.

[36] T. Sakai, M. Kushimoto, Z. Zhang, N. Sugiyama, L. J. Schowalter, Y. Honda, C. Sasaoka, and H. Amano, "On-wafer fabrication of etched-mirror UV-C laser diodes with the ALD-deposited DBR," *Applied Physics Letters*, vol. 116, no. 12, p. 122101, 2020.

[37] Z. Zhang, M. Kushimoto, T. Sakai, N. Sugiyama, L. J. Schowalter, C. Sasaoka, and H. Amano, "A 271.8 nm deep-ultraviolet laser diode for room temperature operation," *Applied Physics Express*, vol. 12, no. 12, p. 124003, 2019.

[38] M. Imada, S. Noda, A. Chutinan, T. Tokuda, M. Murata, and G. Sasaki, "Coherent two-dimensional lasing action in surface-emitting laser with triangular-lattice photonic crystal structure," *Applied Physics Letters*, vol. 75, no. 3, pp. 316–318, 1999.

[39] M. Yoshida, S. Katsuno, T. Inoue, J. Gelleta, K. Izumi, M. De Zoysa, K. Ishizaki, and S. Noda, "High-brightness scalable continuous-wave single-mode photonic-crystal laser," *Nature*, vol. 618, no. 7966, pp. 727–732, 2023.

[40] Vector Photonics, "Vector photonics – a revolution in laser technology," https://www.vectorphotonics.co.uk/, accessed: 2025-08-19, 2025.

[41] R. J. E. Taylor, D. Childs, and R. Hogg, "Vector photonics: the commercial journey of PCSELs and their pathway to high power," in *High-Power Diode Laser Technology XX*, vol. PC11983. SPIE, 2022, p. PC1198304.

[42] Kyoto University, "Kyoto University PCSEL Research Center," https://ku-pcsel-center.or.jp/en/, accessed: 2025-08-19, 2025.

[43] S. Noda, "On the establishment of center of excellence for photonic-crystal surface-emitting lasers," in *High-Power Diode Laser Technology XX*, vol. PC11983. SPIE, 2022, p. PC1198303.

[44] H. Matsubara, S. Yoshimoto, H. Saito, Y. Jianglin, Y. Tanaka, and S. Noda, "GaN photonic-crystal surface-emitting laser at blue-violet wavelengths," *Science*, vol. 319, no. 5862, pp. 445–447, 2008.

[45] D. Apaydin, L. Uhlig, J. Ciers, H. Andersson, S. Graupeter, G. Cardinali, T. Wernicke, M. Kneissl, P. Tassin, U. T. Schwarz, and Å. Haglund, "UVC photonic crystal surface-emitting lasers with low-divergent far-fields," 2023.

[46] M. Kneissl, T.-Y. Seong, J. Han, and H. Amano, "The emergence and prospects of deep-ultraviolet light-emitting diode technologies," *Nature Photonics*, vol. 13, no. 4, pp. 233–244, 2019.

[47] N. Demeersseman, V. Saegeman, V. Cossey, H. Devriese, and A. Schuermans, "Shedding a light on ultraviolet-C technologies in the hospital environment," *Journal of Hospital Infection*, vol. 132, pp. 85–92, 2023.

[48] M. H. Memon, H. Yu, H. Jia, D. Li, R. Wang, J. Yao, Y. Kang, W. Chen, S. Li, J. Zheng, J. Zhang, C. Shen, T. Tao, B. S. Ooi, and H. Sun, "Micro-trench deep-ultraviolet LEDs with boosted efficiency for high-speed solar-blind optical communication," *Journal of Lightwave Technology*, vol. 43, no. 5, pp. 2248–2254, 2025.

[49] F. J. García de Abajo, R. J. Hernández, I. Kaminer, A. Meyerhans, J. Rosell-Llompart, and T. Sanchez-Elsner, "Back to normal: an old physics route to reduce SARS-CoV-2 transmission in indoor spaces," *ACS Nano*, vol. 14, no. 7, pp. 7704–7713, 2020.

[50] United Nations, "The 17 Goals | Sustainable Development," https://sdgs.un.org/goals, accessed: 2025-08-20, 2015.

[51] ASTM International, "ASTM G173-03(2008) Standard Tables for Reference Solar Spectral Irradiances: Direct Normal and Hemispherical on 37° Tilted Surface," http://rredc.nrel.gov/solar/spectra/am1.5/ASTMG173/ASTMG173.xls, downloaded at 2011-02-01, 2008.

[52] S. Khan, D. Newport, and S. Le Calvé, "Gas detection using portable deep-uv absorption spectrophotometry: a review," *Sensors*, vol. 19, no. 23, p. 5210, 2019.

[53] S. M. Brewer, J.-S. Chen, A. M. Hankin, E. R. Clements, C. W. Chou, D. J. Wineland, D. B. Hume, and D. R. Leibrandt, "$^{27}Al^{+}$ quantum-logic clock with a systematic uncertainty below 10^{-18}," *Physical Review Letters*, vol. 123, no. 3, p. 033201, 2019.

[54] T. Hamaguchi, H. Nakajima, M. Ito, J. Mitomo, S. Satou, N. Fuutagawa, and H. Narui, "Lateral carrier confinement of GaN-based vertical-cavity surface-emitting diodes using boron ion implantation," *Japanese Journal of Applied Physics*, vol. 55, no. 12, p. 122101, 2016.

[55] S. Hoshino, Y. Kita, and M. Uchida, "Challenges for the laser scanning headlamps to realize safe driving experience," in *Proceedings of the 12th International Symposium on Automotive Lighting*, vol. 17. München, Germany: Herbert Utz Verlag GmbH, 2017, pp. 299–305.

[56] J. Hager, M. Seitz, and C. Bemmer, "Handling 17 w of scanning laser power — three years of exploration in the ilas project," in *Proceedings of the 12th International Symposium on Automotive Lighting*, vol. 17. München, Germany: Herbert Utz Verlag GmbH, 2017, pp. 271–280.

[57] J. Baghdady, K. Miller, S. Osler, K. Morgan, W. Li, E. Johnson, and B. Cochenour, "Blue-light digital communication in underwater environments utilizing orbital angular momentum," in *Ocean Sensing and Monitoring VIII*, vol. 9827. SPIE, 2016, pp. 114–121.

[58] K. Emoto, T. Koizumi, M. Hirose, M. Jutori, T. Inoue, K. Ishizaki, M. De Zoysa, H. Togawa, and S. Noda, "Wide-bandgap GaN-based watt-class photonic-crystal lasers," *Communications Materials*, vol. 3, no. 1, pp. 1–8, 2022.

[59] S. D. Lester, F. A. Ponce, M. G. Craford, and D. A. Steigerwald, "High dislocation densities in high efficiency GaN-based light-emitting diodes," *Applied Physics Letters*, vol. 66, no. 10, pp. 1249–1251, 1995.

[60] S. Nakamura, "The roles of structural imperfections in InGaN-based blue light-emitting diodes and laser diodes," *Science*, vol. 281, no. 5379, pp. 956–961, 1998.

[61] S. Nakamura, "Nobel Lecture: Background story of the invention of efficient blue InGaN light emitting diodes," *Reviews of Modern Physics*, vol. 87, no. 4, pp. 1139–1151, 2015.

[62] M. Ali Johar, H.-G. Song, A. Waseem, J.-H. Kang, J.-S. Ha, Y.-H. Cho, and S.-W. Ryu, "Ultrafast carrier dynamics of conformally grown semipolar (112[combining macron]2) GaN/InGaN multiple quantum well coaxial nanowires on m-axial GaN core nanowires," *Nanoscale*, vol. 11, no. 22, pp. 10 932–10 943, 2019.

[63] A. David, N. G. Young, C. Lund, and M. D. Craven, "Review — the physics of recombinations in III-nitride emitters," *ECS Journal of Solid State Science and Technology*, vol. 9, no. 1, p. 016021, 2019.

[64] Q. Dai, M. F. Schubert, M. H. Kim, J. K. Kim, E. F. Schubert, D. D. Koleske, M. H. Crawford, S. R. Lee, A. J. Fischer, G. Thaler, and M. A. Banas, "Internal quantum efficiency and nonradiative recombination coefficient of GaInN/GaN multiple quantum wells with different dislocation densities," *Applied Physics Letters*, vol. 94, no. 11, p. 111109, 2009.

[65] A. Bojarska-Cieślińska, Ł. Marona, J. Smalc-Koziorowska, S. Grzanka, J. Weyher, D. Schiavon, and P. Perlin, "Role of dislocations in nitride laser diodes with different indium content," *Scientific Reports*, vol. 11, no. 1, p. 21, 2021.

[66] H. Morkoç, *Handbook of nitride semiconductors and devices, materials properties, physics and growth.* John Wiley & Sons, 2009, google-Books-ID: 00TL1DmoA0QC.

[67] I. Vurgaftman, M. P. Lumb, and J. R. Meyer, *Bands and photons in III-V semiconductor quantum structures.* Oxford, United Kingdom: Oxford University Press, 2021.

[68] F. Della Sala, A. Di Carlo, P. Lugli, F. Bernardini, V. Fiorentini, R. Scholz, and J.-M. Jancu, "Free-carrier screening of polarization fields in wurtzite GaN/InGaN laser structures," *Applied Physics Letters*, vol. 74, no. 14, pp. 2002–2004, 1999.

[69] G. Muziol, M. Hajdel, M. Siekacz, K. Szkudlarek, S. Stanczyk, H. Turski, and C. Skierbiszewski, "Optical properties of III-nitride laser diodes with wide InGaN quantum wells," *Applied Physics Express*, vol. 12, no. 7, p. 072003, 2019.

[70] B. Witzigmann, F. Römer, M. Martens, C. Kuhn, T. Wernicke, and M. Kneissl, "Calculation of optical gain in AlGaN quantum wells for ultraviolet emission," *AIP Advances*, vol. 10, no. 9, p. 095307, 2020.

[71] H. Morkoc, *Nitride semiconductor devices - fundamentals and applications*, 1st ed. Weinheim: Wiley-VCH Verlag GmbH, 2013.

[72] I. Vurgaftman and J. R. Meyer, "Band parameters for nitrogen-containing semiconductors," *Journal of Applied Physics*, vol. 94, no. 6, pp. 3675–3696, 2003.

[73] L. Persson, F. Hjort, G. Cardinali, J. Enslin, T. Kolbe, T. Wernicke, M. Kneissl, J. Ciers, and Å. Haglund, "Athermalization of the lasing wavelength in vertical-cavity surface-emitting lasers," *Laser & Photonics Reviews*, vol. 17, no. 8.

[74] E. Hashemi, J. Bengtsson, J. Gustavsson, M. Calciati, M. Goano, and Å. Haglund, "Thermal lensing effects on lateral leakage in GaN-based vertical-cavity surface-emitting laser cavities," *Optics Express*, vol. 25, no. 9.

[75] U. T. Schwarz, E. Sturm, W. Wegscheider, V. Kümmler, A. Lell, and V. Härle, "Optical gain, carrier-induced phase shift, and linewidth enhancement factor in InGaN quantum well lasers," *Applied Physics Letters*, vol. 83, no. 20, pp. 4095–4097, 2003.

[76] C. Holder, J. S. Speck, S. P. DenBaars, S. Nakamura, and D. Feezell, "Demonstration of nonpolar GaN-based vertical-cavity surface-emitting lasers," *Applied Physics Express*, vol. 5, no. 9, p. 092104, 2012.

[77] C. Liu and J. Zhang, "Influence of quantum well design on light polarization switching in AlGaN ultraviolet emitters," *AIP Advances*, vol. 8, no. 8, p. 085125, 2018.

[78] S. L. Chuang and C. S. Chang, "$k \cdot p$ method for strained wurtzite semiconductors," *Physical Review B*, vol. 54, no. 4, pp. 2491–2504, 1996.

[79] R. G. Banal, M. Funato, and Y. Kawakami, "Optical anisotropy in [0001]-oriented $al_xga_{1-x}n$/aln quantum wells ($x > 0.69$)," *Physical Review B*, vol. 79, no. 12, p. 121308, 2009.

[80] A. Larsson, *Semiconductor optoelectronics: device physics and technologies*. Gothenburg: Chalmers University of Technology, 2015, unpublished course textbook, Photonics Laboratory, Department of Microtechnology and Nanoscience - MC2.

[81] C. G. Van de Walle and J. Neugebauer, "First-principles calculations for defects and impurities: Applications to III-nitrides," *Journal of Applied Physics*, vol. 95, no. 8, pp. 3851–3879, 2004.

[82] F. Mehnke, X. T. Trinh, H. Pingel, T. Wernicke, E. Janzén, N. T. Son, and M. Kneissl, "Electronic properties of si-doped $al_xga_{1-x}n$ with aluminum mole fractions above 80%," *Journal of Applied Physics*, vol. 120, no. 14, p. 145702, 2016.

[83] G. Y. Zhang, Y. Z. Tong, Z. J. Yang, S. X. Jin, J. Li, and Z. Z. Gan, "Relationship of background carrier concentration and defects in GaN grown by metalorganic vapor phase epitaxy," *Applied Physics Letters*, vol. 71, no. 23, pp. 3376–3378, 1997.

[84] M. L. Nakarmi, N. Nepal, J. Y. Lin, and H. X. Jiang, "Photoluminescence studies of impurity transitions in Mg-doped AlGaN alloys," *Applied Physics Letters*, vol. 94, no. 9, p. 091903, 2009.

[85] S. Y. Karpov, "Visible light-emitting diodes," in *Nitride Semiconductor Devices: Principles and Simulation*. John Wiley & Sons, Ltd, 2007, pp. 303–325, section: 14 _eprint: https://onlinelibrary.wiley.com/doi/pdf/10.1002/9783527610723.ch14.

[86] K. Sato, S. Yasue, Y. Ogino, S. Tanaka, M. Iwaya, T. Takeuchi, S. Kamiyama, and I. Akasaki, "Light confinement and high current density in UVB laser diode structure using Al composition-graded p-AlGaN cladding layer," *Applied Physics Letters*, vol. 114, no. 19, p. 191103, 2019.

[87] K. Kiyohara, M. Odawara, T. Takeuchi, S. Kamiyama, M. Iwaya, I. Akasaki, and T. Saito, "Room-temperature continuous-wave operations of GaN-based vertical-cavity surface-emitting lasers with buried GaInN tunnel junctions," *Applied Physics Express*, vol. 13, no. 11, p. 111003, 2020.

[88] S. Lee, C. A. Forman, J. Kearns, J. T. Leonard, D. A. Cohen, S. Nakamura, and S. P. DenBaars, "Demonstration of GaN-based vertical-cavity surface-emitting lasers with buried tunnel junction contacts," *Optics Express*, vol. 27, no. 22, pp. 31 621–31 628, 2019.

[89] A. Filatova-Zalewska, Z. Litwicki, T. Suski, and A. Jeżowski, "Thermal conductivity of thin films of gallium nitride, doped with aluminium, measured with 3 omega method," *Solid State Sciences*, vol. 101, p. 106105, 2020.

[90] S. Adachi, "Lattice thermal conductivity of group-IV and III–V semiconductor alloys," *Journal of Applied Physics*, vol. 102, no. 6, p. 063502, 2007.

[91] J. Piprek, T. Troger, B. Schroter, J. Kolodzey, and C. Ih, "Thermal conductivity reduction in GaAs-AlAs distributed Bragg reflectors," *IEEE Photonics Technology Letters*, vol. 10, no. 1, pp. 81–83, 1998.

[92] E. Hashemi, J. Bengtsson, J. Gustavsson, M. Stattin, G. Cosendey, N. Grandjean, and Å. Haglund, "Analysis of structurally sensitive loss in GaN-based VCSEL cavities and its effect on modal discrimination," *Optics Express*, vol. 22, no. 1.

[93] E. F. Schubert, *Light-emitting diodes*, 2nd ed. Cambridge: Cambridge University Press, 2006.

[94] Å. Haglund, E. Hashemi, J. Bengtsson, J. Gustavsson, M. Stattin, M. Calciati, and M. Goano, "Progress and challenges in electrically pumped GaN-based VCSELs," in *Semiconductor Lasers and Laser Dynamics VII*, vol. 9892. SPIE, 2016, pp. 161–180.

[95] J. Peatross and M. Ware, *Physics of light and optics*, 2015th ed., 2015.

[96] M. A. Bergmann, J. Enslin, F. Hjort, T. Wernicke, M. Kneissl, and Å. Haglund, "Thin-film flip-chip UVB LEDs realized by electrochemical etching," *Applied Physics Letters*, vol. 116, no. 12, p. 121101, 2020.

[97] J. Ciers, M. A. Bergmann, F. Hjort, J.-F. Carlin, N. Grandjean, and Å. Haglund, "Smooth GaN membranes by polarization-assisted electrochemical etching," *Applied Physics Letters*, vol. 118, no. 6, p. 062107, 2021.

[98] E. Torres, J. Ciers, N. Rebelo, F. Hjort, M. A. Bergmann, S. Graupeter, J. Enslin, G. Cardinalli, T. Wernicke, M. Kneissl, and Å. Haglund, "Ultraviolet-c vertical-cavity surface-emitting lasers with precise cavity length control," *Laser & Photonics Reviews*, vol. n/a, no. n/a.

[99] P. Blood, *Quantum confined laser devices: optical gain and recombination in semiconductors*. Oxford: Oxford University Press, 2015.

[100] T.-C. Lu, B.-S. Cheng, and M.-C. Liu, "Temperature dependent gain characteristics in GaN-based vertical-cavity surface-emitting lasers," *Optics Express*, vol. 17, no. 22, pp. 20 149–20 154, 2009.

[101] C. Hentschel, C. P. Allford, S.-J. Gillgrass, J. Travers-Nabialek, R. Forrest, J. Baker, J. Meiklejohn, D. Powell, W. Meredith, M. Haji, J. I. Davies, S. Shutts, and P. M. Smowton, "Gain measurements on VCSEL material using segmented contact technique," *Journal of Physics D: Applied Physics*, vol. 56, no. 7, p. 074003, 2023.

[102] "Scrutinizing lasers," *Nature Photonics*, vol. 11, no. 3, pp. 139–139, 2017.

[103] G. R. Hadley, "Effective index model for vertical-cavity surface-emitting lasers," *Optics Letters*, vol. 20, no. 13, p. 1483, 1995.

[104] G. Hadley, K. Lear, M. Warren, K. Choquette, J. Scott, and S. Corzine, "Comprehensive numerical modeling of vertical-cavity surface-emitting lasers," *IEEE Journal of Quantum Electronics*, vol. 32, no. 4, pp. 607–616, 1996.

[105] "Engineering the lateral optical guiding in gallium nitride-based vertical-cavity surface-emitting laser cavities to reach the lowest threshold gain," vol. 52.

[106] M. Yoshida, M. De Zoysa, K. Ishizaki, Y. Tanaka, M. Kawasaki, R. Hatsuda, B. Song, J. Gelleta, and S. Noda, "Double-lattice photonic-crystal resonators enabling high-brightness semiconductor lasers with symmetric narrow-divergence beams," *Nature Materials*, vol. 18, no. 2, pp. 121–128, 2019.

[107] J. Bengtsson, J. Gustavsson, Å. Haglund, A. Larsson, A. Bachmann, K. Kashani-Shirazi, and M.-C. Amann, "Diffraction loss in long-wavelength buried tunnel junction VCSELs analyzed with a hybrid coupled-cavity transfer-matrix model," *Optics Express*, vol. 16, no. 25, pp. 20 789–20 802, 2008.

[108] N. Hayashi, J. Ogimoto, K. Matsui, T. Furuta, T. Akagi, S. Iwayama, T. Takeuchi, S. Kamiyama, M. Iwaya, and I. Akasaki, "A GaN-based VCSEL with a convex structure for optical guiding," *physica status solidi (a)*, vol. 215, no. 10, p. 1700648, 2018.

[109] M. Kuramoto, S. Kobayashi, T. Akagi, K. Tazawa, K. Tanaka, T. Saito, and T. Takeuchi, "High-output-power and high-temperature operation of blue GaN-based vertical-cavity surface-emitting laser," *Applied Physics Express*, vol. 11, no. 11, p. 112101, 2018.

[110] S. Lin, J. Chang, J. Sun, and P. Xu, "Improvement of the detection sensitivity for tunable diode laser absorption spectroscopy: a review," *Frontiers in Physics*, vol. 10, 2022.

[111] Y. Y. Jiang, A. D. Ludlow, N. D. Lemke, R. W. Fox, J. A. Sherman, L.-S. Ma, and C. W. Oates, "Making optical atomic clocks more stable with 10^{-16}-level laser stabilization," *Nature Photonics*, vol. 5, no. 3, pp. 158–161, 2011.

[112] K. Iga and J. Tatum, "Single-mode VCSELs for sensing applications," in *VCSEL Industry.* John Wiley & Sons, Ltd, 2021, pp. 169–187.

[113] V. A. Shchukin, N. N. Ledentsov, T. Slight, W. Meredith, N. Y. Gordeev, A. M. Nadtochy, A. S. Payusov, M. V. Maximov, S. A. Blokhin, A. A. Blokhin, Y. M. Zadiranov, N. A. Maleev, V. M. Ustinov, and K. D. Choquette, "Passive cavity surface-emitting lasers: option of temperature-insensitive lasing wavelength for uncooled dense wavelength division multiplexing systems," in *Vertical-Cavity Surface-Emitting Lasers XX*, vol. 9766. SPIE, 2016, pp. 30–39.

[114] A. Liu, P. Wolf, J. A. Lott, and D. Bimberg, "Vertical-cavity surface-emitting lasers for data communication and sensing," *Photonics Research*, vol. 7, no. 2, pp. 121–136, 2019.

[115] S. F. Yu, *Analysis and design of vertical-cavity surface-emitting lasers.* Hoboken, N.J: Wiley-Interscience, 2003.

[116] P. Harrison and A. Valavanis, *Quantum wells, wires and dots: theoretical and computational physics of semiconductor nanostructures.* Chichester, West Sussex, United Kingdom ; Hoboken, NJ, USA: Wiley, 2016.

[117] M. Levinshtein, S. Rumyantsev, and M. Shur, "Properties of advanced semiconductor materials : GaN, AlN, InN, BN, SiC, SiGe," 2001.

[118] I. Barin, O. Knacke, and O. Kubaschewski, *Thermochemical properties of inorganic substances.* Berlin, Heidelberg: Springer, 1977.

[119] W. B. Pearson, *A handbook of lattice spacings and structures of metals and alloys.* New York: Pergamon Press, 1958, open Library ID: OL6227710M.

[120] J. M. Redwing, D. A. S. Loeber, N. G. Anderson, M. A. Tischler, and J. S. Flynn, "An optically pumped GaN–AlGaN vertical cavity surface emitting laser," *Applied Physics Letters*, vol. 69, no. 1, pp. 1–3, 1996.

[121] R. Iida, Y. Ueshima, W. Muranaga, S. Iwayama, T. Takeuchi, S. Kamiyama, M. Iwaya, and I. Akasaki, "GaN-based vertical cavity surface emitting lasers with lateral optical confinements and conducting distributed Bragg reflectors," *Japanese Journal of Applied Physics*, vol. 59, no. SG, p. SGGE08, 2020.

[122] T. Nagasawa, K. Kobayashi, R. Watanabe, T. Takeuchi, S. Kamiyama, M. Iwaya, and T. Kamei, "In situ cavity length control of GaN-based vertical-cavity surface-emitting lasers with in situ reflectivity spectra measurements," *Japanese Journal of Applied Physics*, vol. 62, no. 6, p. 066504, 2023.

[123] K. Hiraiwa, W. Muranaga, S. Iwayama, T. Takeuchi, S. Kamiyama, M. Iwaya, and I. Akasaki, "In situ wafer curvature measurement and strain control of AlInN/GaN distributed Bragg reflectors," *Applied Physics Express*, vol. 13, no. 5, p. 055506, 2020.

[124] T. Akagi, Y. Kozuka, K. Ikeyama, S. Iwayama, M. Kuramoto, T. Saito, T. Tanaka, T. Takeuchi, S. Kamiyama, M. Iwaya, and I. Akasaki, "High-quality AlInN/GaN distributed Bragg reflectors grown by metalorganic vapor phase epitaxy," *Applied Physics Express*, vol. 13, no. 12, p. 125504, 2020.

[125] K. Shibata, T. Nagasawa, K. Kobayashi, R. Watanabe, T. Tanaka, T. Takeuchi, S. Kamiyama, M. Iwaya, and T. Kamei, "High-quality n-type conductive Si-doped AlInN/GaN DBRs with hydrogen cleaning," *Applied Physics Express*, vol. 15, no. 11, p. 112007, 2022.

[126] K. Kobayashi, K. Shibata, T. Nagasawa, R. Watanabe, K. Usui, T. Takeuchi, S. Kamiyama, M. Iwaya, and T. Kamei, "N-type conducting AlInN/GaN distributed Bragg reflectors with AlGaN graded layers," *Japanese Journal of Applied Physics*, vol. 62, no. SN, p. SN1012, 2023.

[127] G. Cosendey, A. Castiglia, G. Rossbach, J.-F. Carlin, and N. Grandjean, "Blue monolithic AlInN-based vertical cavity surface emitting laser diode on free-standing GaN substrate," *Applied Physics Letters*, vol. 101, no. 15, p. 151113, 2012.

[128] S. Izumi, N. Fuutagawa, T. Hamaguchi, M. Murayama, M. Kuramoto, and H. Narui, "Room-temperature continuous-wave operation of GaN-based vertical-cavity surface-emitting lasers fabricated using epitaxial lateral overgrowth," *Applied Physics Express*, vol. 8, no. 6, p. 062702, 2015.

[129] T. Onishi, O. Imafuji, K. Nagamatsu, M. Kawaguchi, K. Yamanaka, and S. Takigawa, "Continuous wave operation of GaN vertical-cavity surface-emitting lasers at room temperature," *IEEE Journal of Quantum Electronics*, vol. 48, no. 9, pp. 1107–1112, 2012.

[130] T. Hamaguchi, M. Tanaka, and H. Nakajima, "A review on the latest progress of visible GaN-based VCSELs with lateral confinement by curved dielectric DBR reflector and boron ion implantation," *Japanese Journal of Applied Physics*, vol. 58, no. SC, p. SC0806, 2019.

[131] T. Hamaguchi, M. Tanaka, J. Mitomo, H. Nakajima, M. Ito, M. Ohara, N. Kobayashi, K. Fujii, H. Watanabe, S. Satou, R. Koda, and H. Narui, "Lateral optical confinement of GaN-based VCSEL using an atomically smooth monolithic curved mirror," *Scientific Reports*, vol. 8, no. 1, p. 10350, 2018.

[132] T. Hamaguchi, H. Nakajima, M. Tanaka, M. Ito, M. Ohara, T. Jyoukawa, N. Kobayashi, T. Matou, K. Hayashi, H. Watanabe, R. Koda, and K. Yanashima, "Sub-milliampere-threshold continuous wave operation of GaN-based vertical-cavity surface-emitting laser with lateral optical confinement by curved mirror," *Applied Physics Express*, vol. 12, no. 4, p. 044004, 2019.

[133] H. Nakajima, T. Hamaguchi, M. Tanaka, M. Ito, T. Jyokawa, T. Matou, K. Hayashi, M. Ohara, N. Kobayashi, H. Watanabe, R. Koda, and K. Yanashima, "Single transverse mode operation of GaN-based vertical-cavity surface-emitting laser with monolithically incorporated curved mirror," *Applied Physics Express*, vol. 12, no. 8, p. 084003, 2019.

[134] T. Hamaguchi, Y. Hoshina, K. Hayashi, M. Tanaka, M. Ito, M. Ohara, T. Jyoukawa, N. Kobayashi, H. Watanabe, M. Yokozeki, R. Koda, and K. Yanashima, "Room-temperature continuous-wave operation of green vertical-cavity surface-emitting lasers with a curved mirror fabricated on (20-21) semi-polar GaN," *Applied Physics Express*, vol. 13, no. 4, p. 041002, 2020.

[135] K. Hayashi, T. Hamaguchi, J. A. Kearns, N. Kobayashi, M. Ohara, T. Makino, S. Nagane, K. Sato, Y. Nakamura, Y. Hoshina, T. Jyoukawa, T. Watanabe, Y. Kikuchi, M. Ito, E. Nakayama, R. Koda, and N. Futagawa, "Narrow emission of blue GaN-based vertical-cavity surface-emitting lasers with a curved mirror," *IEEE Photonics Journal*, vol. 14, no. 4, pp. 1–5, 2022.

[136] M. Ito, T. Hamaguchi, T. Makino, K. Hayashi, J. A. Kearns, M. Ohara, N. Kobayashi, S. Nagane, K. Sato, Y. Nakamura, Y. Hoshina, T. Jyoukawa, T. Watanabe, Y. Kikuchi, S. Kasahara, S. Kusanagi, Y. Kanitani, Y. Kudo, E. Nakayama, R. Koda, and N. Futagawa, "Highly ef-

ficient operation and uniform characteristics of curved mirror vertical-cavity surface-emitting lasers," *Applied Physics Express*, vol. 16, no. 1, p. 012006, 2023.

[137] J. A. Kearns, T. Hamaguchi, K. Hayashi, M. Ohara, T. Makino, M. Ito, N. Kobayashi, T. Jyoukawa, E. Nakayama, S. Nagane, K. Sato, Y. Nakamura, Y. Hoshina, R. Koda, and N. Futagawa, "Longitudinal mode control in long cavity VCSELs with a curved mirror," *Applied Physics Express*, vol. 15, no. 7, p. 072009, 2022.

[138] J. T. Leonard, D. A. Cohen, B. P. Yonkee, R. M. Farrell, S. P. DenBaars, J. S. Speck, and S. Nakamura, "Smooth e-beam-deposited tin-doped indium oxide for III-nitride vertical-cavity surface-emitting laser intracavity contacts," *Journal of Applied Physics*, vol. 118, no. 14, p. 145304, 2015.

[139] T.-C. Lu, C.-C. Kao, H.-C. Kuo, G.-S. Huang, and S.-C. Wang, "CW lasing of current injection blue GaN-based vertical cavity surface emitting laser," *Applied Physics Letters*, vol. 92, no. 14, p. 141102, 2008.

[140] M. Kuramoto, S. Kobayashi, T. Akagi, K. Tazawa, H. Tanaka, and T. Takeuchi, "Nano-height cylindrical waveguide in GaN-based vertical-cavity surface-emitting lasers," *Applied Physics Express*, vol. 13, no. 8, p. 082005, 2020.

[141] J. T. Leonard, D. A. Cohen, B. P. Yonkee, R. M. Farrell, T. Margalith, S. Lee, S. P. DenBaars, J. S. Speck, and S. Nakamura, "Nonpolar III-nitride vertical-cavity surface-emitting lasers incorporating an ion implanted aperture," *Applied Physics Letters*, vol. 107, no. 1, p. 011102, 2015.

[142] M. Kuramoto, S. Kobayashi, T. Akagi, K. Tazawa, K. Tanaka, T. Saito, and T. Takeuchi, "Enhancement of slope efficiency and output power in GaN-based vertical-cavity surface-emitting lasers with a SiO2-buried lateral index guide," *Applied Physics Letters*, vol. 112, no. 11, p. 111104, 2018.

[143] K. Nagata, T. Matsubara, Y. Saito, K. Kataoka, T. Narita, K. Horibuchi, M. Kushimoto, S. Tomai, S. Katsumata, Y. Honda, T. Takeuchi, and H. Amano, "A review on the progress of AlGaN tunnel homojunction deep-ultraviolet light-emitting diodes," *Crystals*, vol. 13, no. 3, p. 524, 2023.

[144] Y. Zhang, Z. Jamal-Eddine, F. Akyol, S. Bajaj, J. M. Johnson, G. Calderon, A. A. Allerman, M. W. Moseley, A. M. Armstrong, J. Hwang, and S. Rajan, "Tunnel-injected sub-290 nm ultraviolet light-emitting diodes with 2.8% external quantum efficiency," *Applied Physics Letters*, vol. 112, no. 7, p. 071107, 2018.

[145] C. Kuhn, L. Sulmoni, M. Guttmann, J. Glaab, N. Susilo, T. Wernicke, M. Weyers, and M. Kneissl, "MOVPE-grown AlGaN-based tunnel heterojunctions enabling fully transparent UVC LEDs," *Photonics Research*, vol. 7, no. 5, pp. B7–B11, 2019.

[146] E. A. Clinton, Z. Engel, E. Vadiee, J. V. Carpenter, Z. C. Holman, and W. A. Doolittle, "Ultra-wide-bandgap AlGaN homojunction tunnel diodes with negative differential resistance," *Applied Physics Letters*, vol. 115, no. 8, p. 082104, 2019.

[147] A. Pandey, J. Gim, R. Hovden, and Z. Mi, "An AlGaN tunnel junction light-emitting diode operating at 255 nm," *Applied Physics Letters*, vol. 117, no. 24, p. 241101, 2020.

[148] K. Kobayashi, T. Nishikawa, R. Watanabe, T. Takeuchi, S. Kamiyama, M. Iwaya, and T. Kamei, "In situ center wavelength control of AlInN/GaN distributed bragg reflectors with in situ reflectivity spectra measurements," *physica status solidi (b)*, vol. 261, no. 11, p. 2400010, 2024.

[149] K. Terao, H. Nagai, D. Morita, S. Masui, T. Yanamoto, and S.-i. Nagahama, "Blue and green GaN-based vertical-cavity surface-emitting lasers with AlInN/GaN DBR," in *Gallium Nitride Materials and Devices XVI*, vol. 11686. SPIE, 2021, p. 116860E.

[150] T. Hamaguchi, M. Ito, J. A. Kearns, T. Makino, K. Hayashi, M. Ohara, N. Kobayashi, T. Jyokawa, E. Nakayama, S. Nagane, K. Sato, Y. Nakamura, Y. Hoshina, Y. Kikuchi, T. Watanabe, Y. Kanitani, S. Kasahara, Y. Kudo, S. Kusanagi, R. Koda, and N. Fuutagawa, "Highly-efficient operation and mode control in GaN-based VCSELs with a curved mirror," in *Gallium Nitride Materials and Devices XVIII*, vol. 12421. SPIE, 2023, pp. 119–126.

[151] K. Omae, Y. Higuchi, K. Nakagawa, H. Matsumura, and T. Mukai, "Improvement in lasing characteristics of GaN-based vertical-cavity surface-emitting lasers fabricated using a GaN substrate," *Applied Physics Express*, vol. 2, no. 5, p. 052101, 2009.

[152] C.-C. Shen, Y.-T. Lu, Y.-W. Yeh, C.-Y. Chen, Y.-T. Chen, C.-W. Sher, P.-T. Lee, Y.-H. Shih, T.-C. Lu, T. Wu, C.-H. Chiu, and H.-C. Kuo, "Design and fabrication of the reliable GaN-based vertical-cavity surface-emitting laser via tunnel junction," *Crystals*, vol. 9, no. 4, p. 187, 2019.

[153] T.-C. Lu, S.-W. Chen, T.-T. Wu, P.-M. Tu, C.-K. Chen, C.-H. Chen, Z.-Y. Li, H.-C. Kuo, and S.-C. Wang, "Continuous wave operation of current injected GaN vertical cavity surface emitting lasers at room temperature," *Applied Physics Letters*, vol. 97, no. 7, p. 071114, 2010.

[154] D. Kasahara, D. Morita, T. Kosugi, K. Nakagawa, J. Kawamata, Y. Higuchi, H. Matsumura, and T. Mukai, "Demonstration of blue and green GaN-based vertical-cavity surface-emitting lasers by current injection at room temperature," *Applied Physics Express*, vol. 4, no. 7, p. 072103, 2011.

[155] W.-J. Liu, X.-L. Hu, L. Y. Ying, J.-Y. Zhang, and B.-P. Zhang, "Room temperature continuous wave lasing of electrically injected GaN-based vertical cavity surface emitting lasers," *Applied Physics Letters*, vol. 104, no. 25, p. 251116, 2014.

[156] D. H. Hsieh, A. J. Tzou, T. S. Kao, F. I. Lai, D. W. Lin, B. C. Lin, T. C. Lu, W. C. Lai, C. H. Chen, and H. C. Kuo, "Improved carrier injection in GaN-based VCSEL via AlGaN/GaN multiple quantum barrier electron blocking layer," *Optics Express*, vol. 23, no. 21, pp. 27 145–27 151, 2015.

[157] T. Hamaguchi, N. Fuutagawa, S. Izumi, M. Murayama, and H. Narui, "Milliwatt-class GaN-based blue vertical-cavity surface-emitting lasers fabricated by epitaxial lateral overgrowth," *physica status solidi (a)*, vol. 213, no. 5, pp. 1170–1176, 2016.

[158] T. Furuta, K. Matsui, K. Horikawa, K. Ikeyama, Y. Kozuka, S. Yoshida, T. Akagi, T. Takeuchi, S. Kamiyama, M. Iwaya, and I. Akasaki, "Room-temperature CW operation of a nitride-based vertical-cavity surface-emitting laser using thick GaInN quantum wells," *Japanese Journal of Applied Physics*, vol. 55, no. 5S, p. 05FJ11, 2016.

[159] C. A. Forman, S. Lee, E. C. Young, J. A. Kearns, D. A. Cohen, J. T. Leonard, T. Margalith, S. P. DenBaars, and S. Nakamura, "Continuous-wave operation of m-plane GaN-based vertical-cavity surface-emitting lasers with a tunnel junction intracavity contact," *Applied Physics Letters*, vol. 112, no. 11, p. 111106, 2018.

[160] R. Xu, Y. Mei, H. Xu, L.-Y. Ying, Z. Zheng, H. Long, D. Zhang, B. Zhang, and J. Liu, "Green vertical-cavity surface-emitting lasers based on combination of blue-emitting quantum wells and cavity-enhanced recombination," *IEEE Transactions on Electron Devices*, vol. 65, no. 10, pp. 4401–4406, 2018.

[161] M. Kuramoto, S. Kobayashi, K. Tazawa, K. Tanaka, T. Akagi, and T. Saito, "In-phase supermode operation in GaN-based vertical-cavity surface-emitting laser," *Applied Physics Letters*, vol. 115, no. 4, p. 041101, 2019.

[162] W. Muranaga, T. Akagi, R. Fuwa, S. Yoshida, J. Ogimoto, Y. Akatsuka, S. Iwayama, T. Takeuchi, S. Kamiyama, M. Iwaya, and I. Akasaki,

"GaN-based vertical-cavity surface-emitting lasers using n-type conductive AlInN/GaN bottom distributed Bragg reflectors with graded interfaces," *Japanese Journal of Applied Physics*, vol. 58, no. SC, p. SCCC01, 2019.

[163] Y. Mei, G.-E. Weng, B.-P. Zhang, J.-P. Liu, W. Hofmann, L.-Y. Ying, J.-Y. Zhang, Z.-C. Li, H. Yang, and H.-C. Kuo, "Quantum dot vertical-cavity surface-emitting lasers covering the 'green gap'," *Light: Science & Applications*, vol. 6, no. 1, pp. e16 199–e16 199, 2017.

[164] N. C. Palmquist, J. A. Kearns, S. Gee, A. Juan, S. Gandrothula, M. Lam, S. P. Denbaars, and S. Nakamura, "Demonstration of III-nitride vertical-cavity surface-emitting lasers with a topside dielectric curved mirror," *Applied Physics Express*, vol. 17, no. 1, p. 016504, 2023.

[165] R. Watanabe, K. Kobayashi, M. Yanagawa, T. Takeuchi, S. Kamiyama, M. Iwaya, and T. Kamei, "Over 20% wall plug efficiency of on-wafer GaN-based vertical-cavity surface-emitting laser," *Applied Physics Letters*, vol. 124, no. 13, p. 131107, 2024.

[166] K. Terao, H. Nagai, K. Tsukayama, T. Ohara, Y. Hara, R. Shimazu, S. Masui, T. Yanamoto, and S.-I. Nagahama, "Highly efficient blue and green VCSELs with AlInN/GaN bottom DBRs," in *2023 Conference on Lasers and Electro-Optics (CLEO)*, 2023, pp. 1–2, iSSN: 2160-8989.

[167] N. C. Palmquist, S. Gee, S. Gandrothula, X. Li, H. M. Chang, S. P. Denbaars, and S. Nakamura, "Characterization of long-cavity GaN vertical-cavity surface-emitting lasers with a topside dielectric lens," *Japanese Journal of Applied Physics*, vol. 64, no. 5, p. 050901, 2025.

[168] J. A. Kearns, J. Back, N. C. Palmquist, D. A. Cohen, S. P. DenBaars, and S. Nakamura, "Inhomogeneous current injection and filamentary lasing of semipolar $(20\bar{2}\bar{1})$ blue GaN-based vertical-cavity surface-emitting lasers with buried tunnel junctions," *physica status solidi (a)*, vol. 217, no. 7, p. 1900718, 2020.

[169] J. H. Park, D. Y. Kim, E. F. Schubert, J. Cho, and J. K. Kim, "Fundamental limitations of wide-bandgap semiconductors for light-emitting diodes," *ACS Energy Letters*, vol. 3, no. 3, pp. 655–662, 2018.

[170] G. Cardinali, F. Hjort, N. Prokop, J. Enslin, M. Cobet, M. A. Bergmann, J. Gustavsson, J. Ciers, I. Häusler, T. Kolbe, T. Wernicke, Å. Haglund, and M. Kneissl, "Low-threshold AlGaN-based UVB VCSELs enabled by post-growth cavity detuning," *Applied Physics Letters*, vol. 121, no. 10, p. 103501, 2022.

[171] Z. Zheng, Y. Wang, J. Hoo, S. Guo, Y. Mei, H. Long, L. Ying, Z. Zheng, and B. Zhang, "High-quality AlGaN epitaxial structures and realization

of UVC vertical-cavity surface-emitting lasers," *Science China Materials*, vol. 66, no. 5, pp. 1978–1988, 2023.

[172] H. Zhou, M. Diagne, E. Makarona, A. Nurmikko, J. Han, K. Waldrip, and J. Figiel, "Near ultraviolet optically pumped vertical cavity laser," *Electronics Letters*, vol. 36, no. 21, pp. 1777–1779, 2000.

[173] J.-Y. Zhang, L.-E. Cai, B.-P. Zhang, S.-Q. Li, F. Lin, J.-Z. Shang, D.-X. Wang, K.-C. Lin, J.-Z. Yu, and Q.-M. Wang, "Blue-violet lasing of optically pumped GaN-based vertical-cavity surface-emitting lasers with dielectric distributed bragg reflectors," *Journal of Lightwave Technology*, vol. 27, no. 1, pp. 55–59, 2009.

[174] C. Zhang, R. T. ElAfandy, J. Zhang, S. Chen, A. Nurmikko, and J. Han, "Development of nanopore-based near ultraviolet vertical-cavity surface emitting lasers," in *Gallium Nitride Materials and Devices XIV*, vol. 10918. SPIE, 2019, pp. 138–148.

[175] T. S. T. Someya, K. T. K. Tachibana, J. L. J. Lee, T. K. T. Kamiya, and Y. A. Y. Arakawa, "Lasing emission from an $in_{0.1}ga_{0.9}n$ vertical-cavity surface-emitting laser," *Japanese Journal of Applied Physics*, vol. 37, no. 12A, p. L1424, 1998.

[176] T. Someya, R. Werner, A. Forchel, and Y. Arakawa, "Growth and structural characterization of InGaN vertical-cavity surface-emitting lasers operating at room temperature," *physica status solidi (a)*, vol. 176, no. 1, pp. 63–66, 1999, _eprint: https://onlinelibrary.wiley.com/doi/pdf/10.1002/%28SICI%291521-396X%28199911%29176%3A1%3C63%3A%3AAID-PSSA63%3E3.0.CO%3B2-8.

[177] Y. J. Park, T. Detchprohm, K. Mehta, J. Wang, H. Jeong, Y.-S. Liu, P. Chen, S. Wang, S.-C. Shen, P. D. Yoder, F. Ponce, and R. Dupuis, "Optically pumped vertical-cavity surface-emitting lasers at 375 nm with air-gap/$al_{0.05}ga_{0.95}n$ distributed bragg reflectors," in *Vertical-Cavity Surface-Emitting Lasers XXIII*, vol. 10938. SPIE, 2019, pp. 27–33.

[178] S.-H. Park, J. Kim, H. Jeon, T. Sakong, S.-N. Lee, S. Chae, Y. Park, C.-H. Jeong, G.-Y. Yeom, and Y.-H. Cho, "Room-temperature GaN vertical-cavity surface-emitting laser operation in an extended cavity scheme," *Applied Physics Letters*, vol. 83, no. 11, pp. 2121–2123, 2003.

[179] S. Okur, R. Shimada, F. Zhang, S. D. A. Hafiz, J. Lee, V. Avrutin, H. Morkoç, A. Franke, F. Bertram, J. Christen, and U. rÖzgür, "GaN-based vertical cavities with all dielectric reflectors by epitaxial lateral overgrowth," *Japanese Journal of Applied Physics*, vol. 52, no. 8S, p. 08JH03, 2013.

[180] Y. Mei, P. Gu, S. Yang, L. Ying, and B. Zhang, "Optically pumped flexible GaN-based ultraviolet VCSELs," *Optics Letters*, vol. 49, no. 7, pp. 1816–1819, 2024.

[181] Y.-S. Liu, A. F. M. S. Haq, K. Mehta, T.-T. Kao, S. Wang, H. Xie, S.-C. Shen, P. D. Yoder, F. A. Ponce, T. Detchprohm, and R. D. Dupuis, "Optically pumped vertical-cavity surface-emitting laser at 374.9 nm with an electrically conducting n-type distributed Bragg reflector," *Applied Physics Express*, vol. 9, no. 11, p. 111002, 2016.

[182] S. Kako, T. Someya, and Y. Arakawa, "Observation of enhanced spontaneous emission coupling factor in nitride-based vertical-cavity surface-emitting laser," *Applied Physics Letters*, vol. 80, no. 5, pp. 722–724, 2002.

[183] R. Chen, H. D. Sun, T. Wang, K. N. Hui, and H. W. Choi, "Optically pumped ultraviolet lasing from nitride nanopillars at room temperature," *Applied Physics Letters*, vol. 96, no. 24, p. 241101, 2010.

[184] T.-C. Chang, S.-Y. Kuo, E. Hashemi, Å. Haglund, and T.-C. Lu, "GaN vertical-cavity surface-emitting laser with a high-contrast grating reflector," in *High Contrast Metastructures VII*, vol. 10542. SPIE, 2018, pp. 30–35.

[185] F. Xu, C. Ji, J. Wang, L. Zhang, J. Lang, Z. Zhang, F. Tan, C. Ji, J. Zhang, X. Kang, Z. Qin, G. Ju, X. Yang, N. Tang, X. Wang, W. Ge, and B. Shen, "Wafer scale III-nitride deep-ultraviolet vertical-cavity surface-emitting lasers featuring nanometer-class control of cavity length," iSSN: 2693-5015, 2025.

[186] S. Mishkat-Ul-Masabih, J. Leonard, D. Cohen, S. Nakamura, and D. Feezell, "Techniques to reduce thermal resistance in flip-chip GaN-based VCSELs," *physica status solidi (a)*, vol. 214, no. 8, p. 1600819, 2017.

[187] Y. Mei, R.-B. Xu, H. Xu, L.-Y. Ying, Z.-W. Zheng, B.-P. Zhang, M. Li, and J. Zhang, "A comparative study of thermal characteristics of GaN-based VCSELs with three different typical structures," *Semiconductor Science and Technology*, vol. 33, no. 1, p. 015016, 2017.

[188] L. A. Coldren, S. W. Corzine, and M. L. Mashanovitch, *Diode lasers and photonic integrated circuits*, Hoboken, N.J, 2012.

[189] L. Guo, Y. Guo, J. Yang, J. Yan, J. Liu, J. Wang, and T. Wei, "275 nm deep ultraviolet AlGaN-based micro-LED arrays for ultraviolet communication," *IEEE Photonics Journal*, vol. 14, no. 1, pp. 1–5, 2022.

[190] T.-C. Chang, S.-Y. Kuo, J.-T. Lian, K.-B. Hong, S.-C. Wang, and T.-C. Lu, "High-temperature operation of GaN-based vertical-cavity surface-emitting lasers," *Applied Physics Express*, vol. 10, no. 11, p. 112101, 2017.

[191] T.-C. Lu, T.-T. Wu, S.-W. Chen, P.-M. Tu, Z.-Y. Li, C.-K. Chen, C.-H. Chen, H.-C. Kuo, S.-C. Wang, H.-W. Zan, and C.-Y. Chang, "Characteristics of current-injected GaN-based vertical-cavity surface-emitting lasers," *IEEE Journal of Selected Topics in Quantum Electronics*, vol. 17, no. 6, pp. 1594–1602, 2011.

[192] M. Osinski, "Vertical-cavity surface-emitting lasers: effects of heating on modal characteristics and threshold current," in *Circular-Grating Light-Emitting Sources*, vol. 2398. SPIE, 1995, pp. 42–64.

[193] D. Babic and S. Corzine, "Analytic expressions for the reflection delay, penetration depth, and absorptance of quarter-wave dielectric mirrors," *IEEE Journal of Quantum Electronics*, vol. 28, no. 2, pp. 514–524, 1992.

[194] S. Wiechmann and J. Müller, "Thermo-optic properties of TiO2, Ta2O5 and Al2O3 thin films for integrated optics on silicon," *Thin Solid Films*, vol. 517, no. 24, pp. 6847–6849, 2009.

[195] G. Gülşen and M. Naci Inci, "Thermal optical properties of TiO2 films," *Optical Materials*, vol. 18, no. 4, pp. 373–381, 2002.

[196] T. Hamaguchi, "GaN-based VCSELs with a monolithic curved mirror: challenges and prospects," *Photonics*, vol. 10, no. 4, p. 470, 2023.

[197] C. O. Holder, J. T. Leonard, R. M. Farrell, D. A. Cohen, B. Yonkee, J. S. Speck, S. P. DenBaars, S. Nakamura, and D. F. Feezell, "Nonpolar III-nitride vertical-cavity surface emitting lasers with a polarization ratio of 100% fabricated using photoelectrochemical etching," *Applied Physics Letters*, vol. 105, no. 3, p. 031111, 2014.

[198] J. A. Kearns, J. Back, D. A. Cohen, S. P. DenBaars, and S. Nakamura, "Demonstration of blue semipolar $(20\bar{2}\bar{1})$ GaN-based vertical-cavity surface-emitting lasers," *Optics Express*, vol. 27, no. 17, pp. 23 707–23 713, 2019.

[199] J. Gustavsson, Å. Haglund, J. Bengtsson, P. Modh, and A. Larsson, "Dynamic behavior of fundamental-mode stabilized VCSELs using a shallow surface relief," *IEEE Journal of Quantum Electronics*, vol. 40, no. 6, pp. 607–619, 2004.

[200] A. Haglund, J. Gustavsson, J. Vukusic, P. Modh, and A. Larsson, "Single fundamental-mode output power exceeding 6 mW from VCSELs with a shallow surface relief," *IEEE Photonics Technology Letters*, vol. 16, no. 2, pp. 368–370, 2004.

[201] J. S. Gustavsson, Å. Haglund, J. A. Vukušić, J. Bengtsson, P. Jedrasik, and A. Larsson, "Efficient and individually controllable mechanisms for

mode and polarization selection in VCSELs, based on a common, localized, sub-wavelength surface grating," *Optics Express*, vol. 13, no. 17, pp. 6626–6634, 2005.

[202] Å. Haglund, J. S. Gustavsson, J. Bengtsson, P. Jedrasik, and A. Larsson, "Design and evaluation of fundamental-mode and polarization-stabilized VCSELs with a subwavelength surface grating," *IEEE Journal of Quantum Electronics*, vol. 42, no. 3, pp. 231–240, 2006.

[203] A. Larsson and J. S. Gustavsson, "Single-Mode VCSELs," in *VCSELs: Fundamentals, Technology and Applications of Vertical-Cavity Surface-Emitting Lasers*, R. Michalzik, Ed. Berlin, Heidelberg: Springer, 2013, pp. 119–144.

[204] J. Gustavsson, J. Vukusic, J. Bengtsson, and A. Larsson, "A comprehensive model for the modal dynamics of vertical-cavity surface-emitting lasers," *IEEE Journal of Quantum Electronics*, vol. 38, no. 2, pp. 203–212, 2002.

[205] Z. Zhang, M. Kushimoto, A. Yoshikawa, K. Aoto, L. J. Schowalter, C. Sasaoka, and H. Amano, "Continuous-wave lasing of AlGaN-based ultraviolet laser diode at 274.8 nm by current injection," *Applied Physics Express*, vol. 15, no. 4, p. 041007, 2022.

[206] S. Zanotti, M. Minkov, D. Nigro, D. Gerace, S. Fan, and L. C. Andreani, "Legume: A free implementation of the guided-mode expansion method for photonic crystal slabs," *Computer Physics Communications*, vol. 304, p. 109286, 2024.

[207] L.-L. Lin, Z.-Y. Li, and K.-M. Ho, "Lattice symmetry applied in transfer-matrix methods for photonic crystals," *Journal of Applied Physics*, vol. 94, no. 2, pp. 811–821, 2003.

[208] K. S. Kunz and R. J. Luebbers, *The finite difference time domain method for electromagnetics*. Boca Raton: CRC Press, 2018.

[209] Y. Liang, C. Peng, K. Sakai, S. Iwahashi, and S. Noda, "Three-dimensional coupled-wave analysis for square-lattice photonic crystal surface emitting lasers with transverse-electric polarization: finite-size effects," *Optics Express*, vol. 20, no. 14, pp. 15 945–15 961, 2012.

[210] Y. Liang, C. Peng, K. Ishizaki, S. Iwahashi, K. Sakai, Y. Tanaka, K. Kitamura, and S. Noda, "Three-dimensional coupled-wave analysis for triangular-lattice photonic-crystal surface-emitting lasers with transverse-electric polarization," *Optics Express*, vol. 21, no. 1, pp. 565–580, 2013.

[211] H.-Y. Ryu, M. Notomi, and Y.-H. Lee, "Finite-difference time-domain investigation of band-edge resonant modes in finite-size two-dimensional photonic crystal slab," *Physical Review B*, vol. 68, no. 4, p. 045209, 2003.

[212] M. Yokoyama and S. Noda, "Finite-difference time-domain simulation of two-dimensional photonic crystal surface-emitting laser," *Optics Express*, vol. 13, no. 8, pp. 2869–2880, 2005.

[213] O. Häggström, "Problem solving is often a matter of cooking up an appropriate markov chain," *Scandinavian Journal of Statistics*, vol. 34, no. 4, pp. 768–780, 2007, _eprint: https://onlinelibrary.wiley.com/doi/pdf/10.1111/j.1467-9469.2007.00561.x.

[214] J. Liu, Y. Gao, P. Ivanov, P. Harvey, and R. Hogg, "Probabilistic Markov chain modeling of photonic crystal surface emitting lasers," *Applied Physics Letters*, vol. 123, no. 26, p. 261107, 2023.

[215] J. Liu, D. Kim, Z. Bian, J. Feng, Y. Gao, P. Harvey, and R. Hogg, "Convergence criteria for probabilistic markov chains modelling of photonic crystal surface-emitting lasers," in *Novel In-Plane Semiconductor Lasers XXII*, vol. 12440. SPIE, 2023, pp. 75–80.

[216] J. Liu, X. Zhao, Z. Bian, S. J. Sweeney, and R. Hogg, "Optimization of pumping geometry of photonic crystal surface emitting lasers," in *Physics and Simulation of Optoelectronic Devices XXXIII*, vol. 13360. SPIE, 2025, pp. 14–18.

[217] Z. Bian, X. Zhao, J. Liu, D. Kim, A. F. McKenzie, S. Thoms, P. Reynolds, N. D. Gerrard, A. S. M. Kyaw, J. Grant, K. Rae, J. R. Orchard, C. H. Hill, C. W. Munro, P. Ivanov, D. T. D. Childs, R. J. E. Taylor, and R. A. Hogg, "Resonator embedded photonic crystal surface emitting lasers," *npj Nanophotonics*, vol. 1, no. 1, p. 13, 2024.

[218] N. Taguchi, A. Iwai, M. Noguchi, H. Takahashi, A. Michiue, M. De Zoysa, T. Inoue, K. Ishizaki, and S. Noda, "Green-wavelength GaN-based photonic-crystal surface-emitting lasers," *Applied Physics Express*, vol. 17, no. 1, p. 012002, 2024.

[219] M. Usman, M. , Munaza, M. , Urooj, A. , Abdur-Rehman, , and N. Muhammad, "Green gap in GaN-based light-emitting diodes: in perspective," *Critical Reviews in Solid State and Materials Sciences*, vol. 46, no. 5, pp. 450–467, 2021.

[220] T.-C. Lu, S.-W. Chen, L.-F. Lin, T.-T. Kao, C.-C. Kao, P. Yu, H.-C. Kuo, S.-C. Wang, and S. Fan, "GaN-based two-dimensional surface-emitting photonic crystal lasers with AlN/GaN distributed Bragg reflector," *Applied Physics Letters*, vol. 92, no. 1, p. 011129, 2008.

[221] S. Kawashima, T. Kawashima, Y. Nagatomo, Y. Hori, H. Iwase, T. Uchida, K. Hoshino, A. Numata, and M. Uchida, "GaN-based surface-emitting laser with two-dimensional photonic crystal acting as distributed-feedback grating and optical cladding," *Applied Physics Letters*, vol. 97, no. 25, p. 251112, 2010.

[222] D.-U. Kim, S. Kim, J. Lee, S.-R. Jeon, and H. Jeon, "Free-standing GaN-based photonic crystal band-edge laser," *IEEE Photonics Technology Letters*, vol. 23, no. 20, pp. 1454–1456, 2011.

[223] Y.-H. Ra and C.-R. Lee, "Ultracompact display pixels: tunnel junction nanowire photonic crystal laser," *Nano Energy*, vol. 84, p. 105870, 2021.

[224] M. F. Vafadar and S. Zhao, "Ultralow threshold surface emitting ultraviolet lasers with semiconductor nanowires," *Scientific Reports*, vol. 13, no. 1, p. 6633, 2023.

[225] M. Imada, A. Chutinan, S. Noda, and M. Mochizuki, "Multidirectionally distributed feedback photonic crystal lasers," *Physical Review B*, vol. 65, no. 19, p. 195306, 2002.

[226] M. N. Robinson, S. J. Sweeney, and R. A. Hogg, "Two-dimensional coupled wave theory for triangular lattice tm-polarised photonic crystal surface-emitting lasers," *IEEE Journal of Selected Topics in Quantum Electronics*, vol. 31, no. 2: Pwr. and Effic. Scaling in Semiconductor Lasers, pp. 1–11, 2025.

[227] C. R. Pollock and M. Lipson, *Integrated photonics*. Boston, MA: Springer US, 2003.

[228] Y. Liang, C. Peng, K. Sakai, S. Iwahashi, and S. Noda, "Three-dimensional coupled-wave model for square-lattice photonic crystal lasers with transverse electric polarization: A general approach," *Physical Review B*, vol. 84, no. 19, p. 195119, 2011.

[229] K. Sakai, J. Yue, and S. Noda, "Coupled-wave model for triangular-lattice photonic crystal with transverse electric polarization," *Optics Express*, vol. 16, no. 9, pp. 6033–6040, 2008.

[230] M. J. Bergmann and H. C. Casey, Jr., "Optical-field calculations for lossy multiple-layer $al_xga_{1-x}n/in_xga_{1-x}n$ laser diodes," *Journal of Applied Physics*, vol. 84, no. 3, pp. 1196–1203, 1998.

[231] Y. Chassagneux, R. Colombelli, W. Maineult, S. Barbieri, H. E. Beere, D. A. Ritchie, S. P. Khanna, E. H. Linfield, and A. G. Davies, "Electrically pumped photonic-crystal terahertz lasers controlled by boundary conditions," *Nature*, vol. 457, no. 7226, pp. 174–178, 2009.

[232] K. Sakai, E. Miyai, and S. Noda, "Coupled-wave model for square-lattice two-dimensional photonic crystal with transverse-electric-like mode," *Applied Physics Letters*, vol. 89, no. 2, p. 021101, 2006.

[233] K. Sakai, E. Miyai, and S. Noda, "Two-dimensional coupled wave theory for square-lattice photonic-crystal lasers with TM-polarization," *Optics Express*, vol. 15, no. 7, pp. 3981–3990, 2007.

Included papers A-C